Application of the Calcium Looping Cycle to CO_2 Mitigation in the Cement Process

Charles Dean

Department of Chemical Engineering and Chemical Technology

Imperial College London

A thesis submitted for the degree of Doctor of Philosophy and for the Diploma of Imperial College.

Abstract

The Ca-looping cycle is a novel means of capturing CO_2 from an industrial or power flue gas. It has an inherent synergy with cement production in that a by-product is predominantly CaO, which forms nearly 70 % of the material feed to a cement works. However, integration of the two processes will inevitably lead to a decrease in the thermal efficiency of producing 1 kg of clinker due to the energy penalty of the Ca-loop calciner. Furthermore, experimental studies are required to determine whether any change in the trace element inventory of the sorbent takes place due to cycling between calcination and carbonation conditions, and whether such changes impact on the phase composition or mechanical properties of the subsequent cement produced.

For the flow-sheeting part of this investigation, the thermal efficiency of producing 1 kg clinker when integrated with Ca-looping was found to increase by between 0.15 and 1.49 MJ depending on the configuration. For the experimental part of this investigation, it was found that cycling in the absence of fuel did not lead to a change in trace element content of the sorbent. However, in the presence of fuel combustion, the trace element inventory of the sorbent was seen to increase. Al increased for all three fuels indicating that ash from the fuel was mixing with the sorbent during the calcination step. Cycling in the presence of Lea Hall coal led to an increase in B and Na, whilst cycling in the presence of refuse-derived-fuel led to an increase in Cu, Na and Ti. The production of cement from cycled sorbent indicated that cycling in the absence of fuel did not lead to a change in phase composition. This was also the case for cements produced from sorbent cycled in the presence of continuously fed La Jagua and Lea Hall coals. However, a slight increase in the % wt. alite was observed for cements produced from sorbent exposed to batch-fed La Jagua. Lastly, after undergoing performance tests it was found that there was a general downward trend in the strength of the cement mortars produced with increasing cycle number. Setting times were within the range set out in the British and American Standards.

Acknowledgements

I would like to express my sincere thanks to my supervisors, Dr. Paul Fennell and Prof. Denis Dugwell for giving me the opportunity to come to Imperial and study towards this PhD; also for their guidance and support throughout this research. Thankyou also to Dr. Nigel Paterson who provided valuable assistance during the early stages.

I gratefully acknowledge the financial support for this work provided by the EPSRC and also by Cemex Operations U.K. Ltd. Thankyou also to Dr. Mike Andrews at Cemex Rugby who provided guidance, useful literature and many of the materials used in this project.

Thanks also to all other members of the Energy Engineering group who have made it a great place to study during the last few years.

Contents

List of Figures

List of Tables

Parts of thesis have been published in (Dean, C. C. et al. 2011) and (Dean, C. et al 2012).

John Blamey, Mohamad Al-Jeboori and Nick Florin helped with the review article upon which the introduction was based.

Introduction

All scientific bodies now concede that the evidence for a link between observed climate change and human activity, primarily CO_2 emissions, is compelling (Oreskes 2004). According to the IPCC (Metz, Davidson et al. 2007) and IEA (IEA 2006), the cement industry is responsible for a contribution of between 5 and 7 % to global anthropogenic CO_2 emissions. These emissions come both from chemistry inherent to the cement process (calcination of limestone) and the burning of fossil fuels, necessary to provide the high temperatures required for the production of clinker.

A state-of-the-art cement plant will include heat integration within the process such that further reductions in fuel use / CO_2 emissions are not possible based on thermodynamic limitations; furthermore, emissions from limestone calcination are seemingly unavoidable due to the need to provide CaO for reaction with other compounds to produce clinker. However, the emergence of CaO-sorbent-based CO_2 capture systems ("The Ca-looping Cycle") offers the potential to supply CaO to a cement process, avoiding CO_2 emissions from both limestone calcination and from the burning of fuel to provide heat to drive the endothermic calcination reaction. This leaves only the portion of CO_2 emissions coming from fuel burnt at the kiln.

Calcium looping (Ca-looping) is a CO_2 capture scheme using solid CaO-based sorbents to remove CO_2 from flue gases, i.e., from a power plant or other large stationary industrial process, producing a concentrated stream of CO_2 (~ 95 %) suitable for storage. The Ca-looping process uses a CaO-based sorbent, usually derived from limestone, reacting via the reversible gas–solid reaction between CO_2 and $CaO_{(s)}$ to form $CaCO_{3(s)}$.

CaO purged from the Ca-looping process will however have been subjected to repeated cycles of calcination and carbonation, most likely in the presence of fuel combustion at the calcination stage (assuming in-situ fuel combustion system). This repeated cycling means that the CaO may be different in chemical composition to that of single-calcination CaO; it will certainly contain higher levels of ash, which may be physically mixed in with the sorbent, or which may react with the CaO to form initial clinker compounds before the sorbent has reached the kiln.

Furthermore, trace elements either contained in the ash sent with the sorbent or released from the fuel through devolatilisation and subsequent reaction with the CaO will be higher in concentration than that of single-calcination CaO. Most trace elements commonly present in fossil fuels are known to impact on cement chemistry in one way or another (see: Background). The practical work detailed in this thesis describes an investigation into 1. changes in the concentration of trace elements in the sorbent due to repeated cycling in the presence of three different solid fuels; 2. the effect of using repeatedly cycled CaO on the % wt. alite in clinker, and to correlate any effect to changes in sorbent trace element concentration; 3. The effect of using repeatedly cycled CaO on the mechanical performance of the cement.

Chapter 1. Background

1.1. The Calcium Looping Cycle

Calcium looping (Ca-looping) is a CO_2 capture scheme using solid CaO-based sorbents to remove CO_2 from flue gases, i.e., from a power plant or other large stationary industrial process, producing a concentrated stream of CO_2 (~ 95 %) suitable for storage. Reviews of the Ca-looping cycle have recently been published (Blamey, Anthony et al. 2010; Dean, Blamey et al. 2011); the main features of which are summarised herein. For further information, see also reviews by Stanmore and Gilot and others (Stanmore and Gilot 2005; Anthony 2008; Harrison 2008; Li and Fan 2008; Florin and Harris 2008a), and the IEA GHG High Temperatures Solid Looping Cycles Network (IEA 2010).

1.1.1. Basics of the Cycle

The Ca-looping process uses a CaO-based sorbent, usually derived from limestone, reacting via the reversible gas–solid reaction between CO_2 and $CaO_{(s)}$ to form $CaCO_{3(s)}$ (Eq. 1-1). The forwards step is known as calcination and is an endothermic process which readily goes to completion under a wide range of conditions. The backwards step is known as carbonation:

$$CaO_{(s)} + CO_{2(g)} \leftrightarrow CaCO_{3(s)}\ \Delta H° = +178\ kJ/mol \qquad \text{Eq. 1-1}$$

A typical Ca-looping process for CO_2 capture as proposed by (Shimizu, Hirama et al. 1999) is shown in Figure 1-1. In this example, the heat necessary for calcination is provided by oxy-combustion of coal, however other methods have been suggested such as providing an external heat source (Alvarez and Abanades 2005).

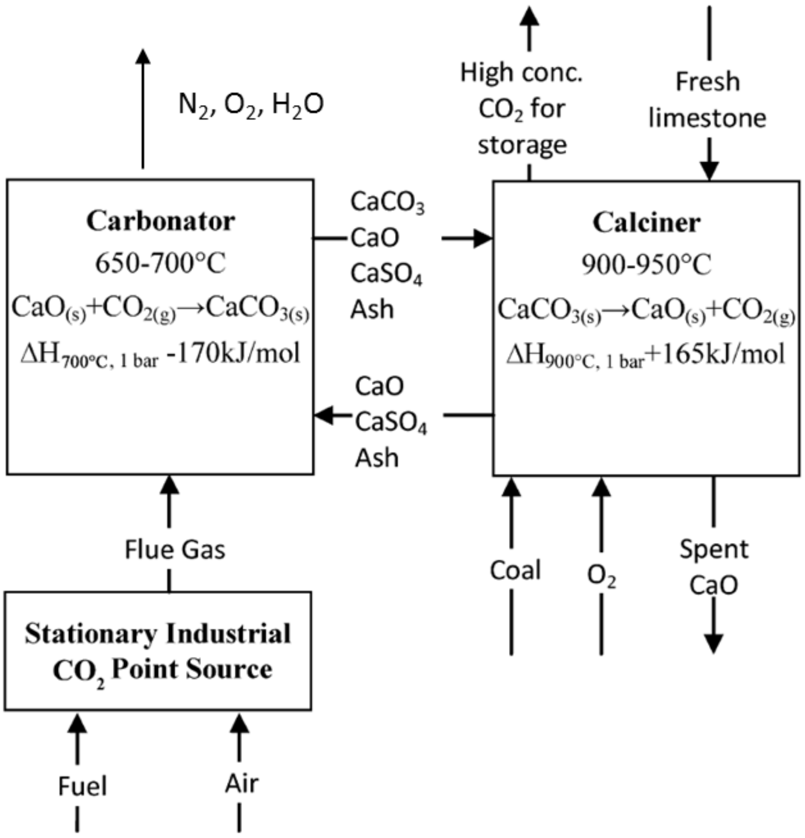

Figure 1-1. Typical example scheme for Ca-looping post-combustion CO_2 capture (enthalpies calculated using data provided by (Mcbride, Zehe et al. 2002).

The equilibrium vapour pressure of CO_2 over CaO according to Eq. 1-1 can be calculated as a function of temperature; partial pressures of CO_2 greater than the equilibrium partial pressure at a given temperature will favour carbonation, while those lower than the equilibrium will favour calcination (see Figure 1-2). As a result, if a sorbent is cycled between two vessels at suitable temperatures, carbonation of sorbent can be effected in one and calcination in the other. The objective of CO_2 capture is to obtain a pure stream of CO_2 suitable for storage; one method of achieving this is by separation of CO_2 from an exhaust gas obtained from power stations or industry (3 – 30 % v / v), i.e. post-combustion CO_2 capture.

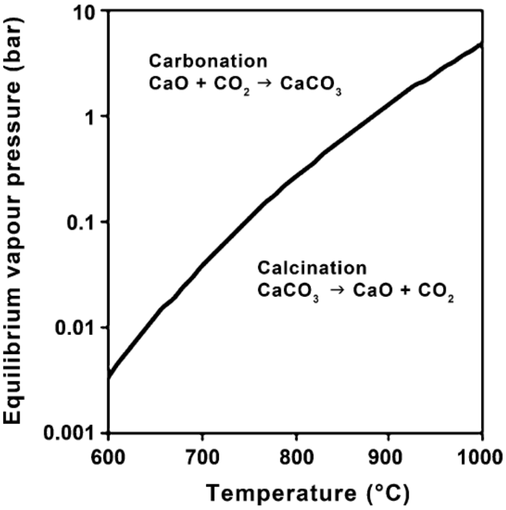

Figure 1-2. Equilibrium vapour pressure of CO2 over CaO as a function of temperature (Mcbride, Zehe et al. 2002).

The calciner temperature (> 850 ◦C) is dictated by the high CO_2 partial pressure necessary to produce a near pure stream (Figure 1-2), and may also be chosen as a compromise between higher temperatures, which increase the rate of calcination at the expense of rapid degradation of the sorbent (see: section 1.1.1.1) and milder temperatures which protect the sorbent; the carbonator temperature is chosen as a compromise between the higher equilibrium (maximum) capture at lower temperatures and a decreased rate of reaction.

Calcium looping has a number of advantages compared to many closer-to-market capture schemes, including: the use of circulating fluidised bed (CFB) reactors (owing to the good gas-solid contacting and uniform bed temperature), a mature technology developed and deployed at large scale (Cuenca M.A. and E.J. 1995; Grace J.R., Avidan A. et al. 1997) up to 460 MWe (Foster_Wheeler, 2012); sorbent derived from cheap, abundant and environmentally benign limestone precursors; and the relatively small efficiency penalty that it imposes on industrial power production process (i.e., estimated at 6 – 8 percentage points, compared to 9.5 – 12.5 from amine-based post-combustion capture). A further advantage is the synergy with cement manufacture, which potentially allows for simultaneous mitigation of a large proportion of CO_2 emissions from the cement process. Integration of power generation and cement manufacture leads to a further reduction in the overall efficiency penalty. If attributed to the power station, the efficiency penalty is reduced by 1.5 – 2 % (Blamey et al 2010). The Ca-looping cycle can also be applied to gasification / pre-combustion techniques, where it can be used to increase hydrogen production by removing CO_2 from the products of the water gas shift Eq. 1-2 and reforming reactions e.g. Eq. 1-3 (Harrison 2008; Florin and Harris 2008a), thus enhancing the maximum production of H_2.

$$CO_{(g)} + H_2O_{(g)} = CO_{2(g)} + H_{2(g)}\ \Delta H^\circ = -41\ kJ\ /\ mol \qquad \text{Eq. 1-2}$$

$$CH_{4(g)} + H_2O_{(g)} \leftrightarrow 3H_{2(g)} + CO_{(g)}\ \Delta H^\circ = 206\ kJ\ /\ mol \qquad \text{Eq. 1-3}$$

1.1.1.1. Sorbent deactivation

Ideally, CaO sorbent would be continually cycled between carbonator and calciner reacting with and evolving 1 mol of CO_2 per mol CaO on each cycle. However, the rate of carbonation of CaO makes a transition from a fast to a very slow diffusion-controlled rate through the product layer (see inset Figure 1-3) (Bhatia and Perlmutter 1983; Mess, Sarofim et al. 1999; Alvarez and Abanades 2005) preventing full conversion to $CaCO_3$ at a rate useful for industrial purposes.

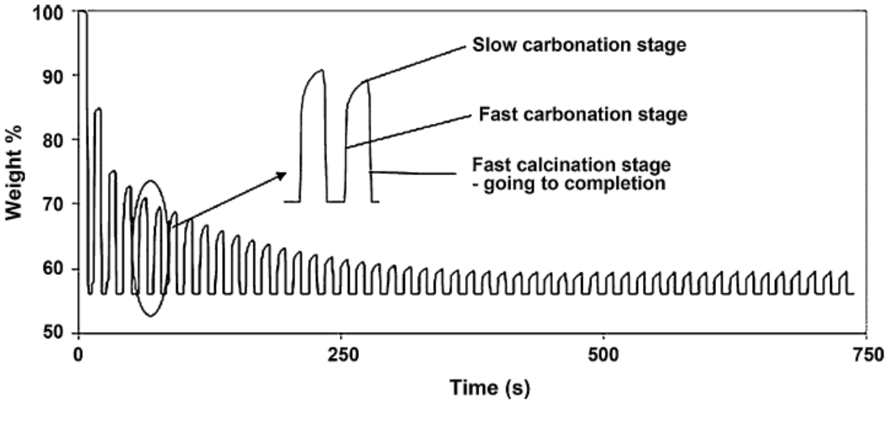

Figure 1-3. Carrying capacity of CaO sorbent through 50 CO_2 capture-and-release cycles represented in terms of mass change vs. time (TGA data for Havelock limestone).

The conversion of CaO to $CaCO_3$ at this transition is often defined as the maximum carbonation conversion or 'carrying capacity' of the sorbent and is well known to decrease upon cycling of the sorbent through multiple CO_2 capture-and-release cycles (Curran 1967; Barker 1973; Deutsch and Heller-Kallai 1991; Silaban and Harrison 1995; Aihara, Nagai et al. 2001; Abanades 2002; Abanades and Alvarez 2003; Fennell, Pacciani et al. 2007a).

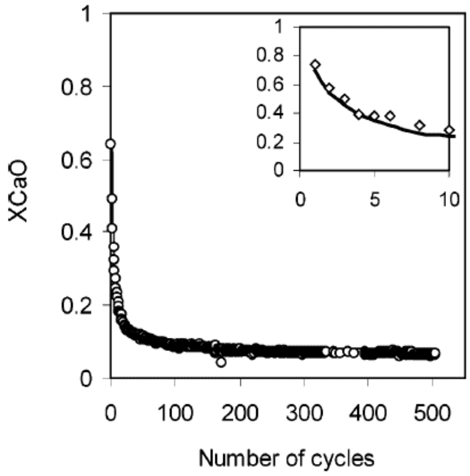

Figure 1-4. Sorbent conversion vs number of cycles. Solid line corresponds to data from eq 1-8; k = 0.52, a_r = 0.075 (see: below)

Loss in sorbent reactivity (as observed in Figure 1-4) can be caused by a number of factors: sintering of the porous CaO during the high temperature calcination stage (the major cause of loss in reactivity); competing sulphation / sulphidation reactions; loss of bed material through attrition causing elutriation of fines; and ash fouling.

CaO formed by calcination of $CaCO_3$ is very porous (Barker 1973) because, as shown in Table 1-1, there is a marked reduction in molar volume from $CaCO_3$ to CaO, resulting in a theoretical porosity of 0.54. However, CaO used for Ca-looping is prone to sintering (i.e., changes in pore shape, pore shrinkage and grain growth, at elevated temperatures), which causes a reduction in reactive surface area and a drop-off in reactivity. The transition to conditions that accelerate the rate of sintering of CaO occurs at approximately 900 °C (Borgwardt 1989a), while increasing partial pressure of CO_2 and steam have also been found to increase the rate of sintering (Borgwardt 1989b). Sintering of CaO can therefore be expected to be severe in the calciner, which in the example scheme in Figure 1-2 is expected to be operating above 900 °C at 101 kPa CO_2. There is also a contribution of reactive sintering that is particular to cycling experiments (Gonzalez, Grasa et al. 2008).

Table 1-1. Physical properties of calcium compounds relevant to the Ca-looping cycle (Perry 1997).

	Molar mass (g / mol)	Density (g / cm^3)	Molar vol. (cm^3 / mol)
$CaCO_3$	100.1	2.71	36.9
CaO	56.1	3.32	16.9
$CaSO_4$	136.1	2.96	46.0
CaS	72.1	2.8	25.8
$Ca(OH)_2$	74.1	2.2	33.7

CaO has a very strong affinity to SO_2 and will readily form $CaSO_4$ in the oxidising conditions expected in post-combustion systems (see Eq. 1-4 for direct sulphation and Eq. 1-5 for indirect sulphation, i.e., sulphation of the carbonate). As a result, CaO derived from limestone has been used as a sorbent for SO_2 on an industrial scale (Smith 2007); e.g., Drax Power Station (coal-fired, 3.96GW) (Drax 2008) in the UK captured 90 % of its sulphur emissions using an independent wet limestone–gypsum flue gas desulphurisation plant. CaO can form CaS upon reaction with H_2S under reducing conditions (see Eq. 1-6 for direct sulphidation and Eq. 1-7 for indirect sulphidation, again, sulphidation of the carbonate). Sulphated sorbent requires very high temperatures or reducing conditions to be regenerated, though sulphide sorbent can be regenerated more readily (Lyngfelt and Leckner 1989; Hayhurst and Tucker 1991; Anthony and Granatstein 2001); both reactions can be considered as resulting in reactive sites lost for carbonation. Grace and co-workers (Ryu, Grace et al. 2006; Sun, Grace et al. 2006) investigated the effect of sulphate and sulphide formation on CO_2 uptake of sorbent and found that sulphate formation is a more significant problem as it results in pore blockage from the formation of $CaSO_4$, which has a much larger molar volume (seeTable 1-1). This pore blockage then prevents access of CO_2 to the centre of a particle:

$$CaO_{(s)} + SO_{2(g)} + 1/2O_{2(g)} = CaSO_{4(s)}\ \Delta H° = -502\ kJ\ /\ mol \qquad \text{Eq. 1-4}$$

$$CaCO_{3(s)} + SO_{2(g)} + 1/2O_{2(g)} = CaSO_{4(s)} + CO_{2(g)}\ \Delta H° = -324\ kJ\ /\ mol \qquad \text{Eq. 1-5}$$

$$CaO_{(s)} + H_2S_{(g)} = CaS_{(s)} + H_2O_{(g)}\ \Delta H° = -61.3\ kJ\ /\ mol \qquad \text{Eq. 1-6}$$

$$CaCO_{3(s)} + H_2S_{(g)} = CaS_{(s)} + CO_{2(g)} + H_2O_{(g)}\ \Delta H° = +117\ kJ\ /\ mol \qquad \text{Eq. 1-7}$$

There has been a large volume of research published on the attrition characteristics of limestone for SO_2 capture (Anthony and Granatstein 2001; Smith 2007; Chen, Grace et al. 2008; Saastamoinen, Pikkarainen et al. 2008; Scala, Montagnaro et al. 2008; Blamey, Anthony et al. 2010). However, there is less research regarding limestone for CO_2 capture. (Fennell, Pacciani et al. 2007a) showed that the most significant attrition occurred in the early cycles of repeated calcination / carbonation cycling experiments. Pilot plant studies published by (Alonso, Rodríguez et al. 2010) observed significant attrition of sorbent at the start of the experiment, while pilot plant studies published by (Lu, Hughes et al. 2008) showed significant attrition throughout operation (> 60 % of material ended up as fine material in the cyclones after 25 cycles, reducing the CO_2 capture rate significantly). The mechanical stability of the sorbent is therefore receiving considerable attention and is likely to be a critical factor in the selection of original limestone for large-scale testing; on this basis, there is a drive towards standardised testing of the mechanical stability of limestone to determine suitability for use in a fluidised environment (Schueppel 2009; Zuberbuehler 2009). An important aspect of scale-up to a typical proposed system, such as that described in Figure 1-1, is the effect of fuel combustion in the calciner. The combustion of the fuel results in two undesirable effects: the introduction of fine ash and chars into the cycle, which have the potential to deposit onto the surface of a particle and result in undesirable side reactions and low temperature melt formation; and higher local temperatures related to fuel-combustion (Joutsenoja, Heino et al. 1999; Scala, Chirone et al. 2003; Corella, Toledo et al. 2006). Accordingly, (Hughes, Macchi et al. 2009) report lower reactivity of sorbent than anticipated and the formation of a dense shell on the surface of particles when combusting high-ash hardwood pellets in the calciner; a similar problem has been described by (Kuramoto, Shibano et al. 2003). There have been a number of attempts to model the decay rate of the maximum carbonation conversion upon cycling, which focus on the reactivity towards CO_2 disregarding sulphation, attrition and ash fouling effects (Abanades 2002; Abanades and Alvarez 2003; Wang and Anthony 2005; Grasa and Abanades 2006; Lysikov, Salanov et al. 2007; Gonzalez, Grasa et al. 2008). For descriptions of these decay equations and a discussion of their individual merits and drawbacks please refer to (Blamey, Anthony et al. 2010). It should be noted that most of the models proposed are semi-empirical and cannot currently be used to predict the behaviour of individual limestones from their intrinsic properties. The author's preferred equation due to its accurate representation of the loss of reactivity over large numbers of cycles (> 20) is Eq. 1-8, proposed by (Grasa and Abanades 2006), where a_n is the maximum carbonation conversion of the sorbent in cycle N, a_∞ is the residual (final) conversion of the sorbent after a very large number of cycles, and k is a decay rate constant:

$$a_n = \left(\frac{1}{\frac{1}{(1-a)}} + kN \right) + a_\infty \qquad \text{Eq. 1-8}$$

It is likely that in a realistic system where sulphation, attrition and ash fouling are unavoidable, a_∞ will tend to zero, however in small scale tests a residual capacity of ~ 60 mg CO_2 / g sorbent is found, which is competitive with other CO_2 sorbents (Rodriguez 2008). A real system will also differ in that the residence time of the sorbent in the calciner or carbonator may not be sufficient to allow full calcination or maximum carbonation, making application of these formulas difficult; such matters are under investigation by Abanades and co-workers (Grasa, Abanades et al. 2009; Rodríguez, Alonso et al. 2010).

1.1.1.2. Sorbent Performance

There is currently a great deal of work being conducted to improve sorbent performance upon cycling. This can be done by alteration of the process conditions or by sorbent enhancement. There are numerous process variables which will affect sorbent performance, the most important of which is the temperature of the calciner. However, steam partial pressure in the carbonator, the residence time of the particles in the calciner and the carbonator, the presence of ash, sulphur and other minor species, and particle size are likely to also play significant roles. The temperature of the calciner can be decreased if the partial pressure of CO_2 is reduced, thus minimising the extent of sorbent sintering upon cycling; the two simplest ways of doing this are by lowering the total pressure (Ewing, Beruto et al. 1979; Alvarez and Abanades 2005; Sakadjian, Iyer et al. 2006) or by introducing steam into the calciner (Alvarez and Abanades 2005; Wang, Lin et al. 2008; Wang, Lin et al. 2009). The main research areas for sorbent enhancement are doping of natural limestones with trace amounts of organic salts, the production of synthetic sorbents, the hydration of spent sorbent, and thermal pre-treatment; an ideal enhanced sorbent will display high mechanical strength while maintaining its reactive surface area over repeated cycling, without being prohibitively expensive—for economic assessments see work by Romeo and co-workers (Romeo, Lara et al. 2009a; Lisbona, Martinez et al. 2010).

There is considerable variability in the reactivity and friability of natural limestones, which should be investigated before selecting a sorbent (Laursen, Duo et al. 2000; Ryu, Grace et al. 2006; Alvarez, Peña et al. 2007; Fennell, Pacciani et al. 2007a). These properties depend on impurities and the conditions / age of formation. Dolomites have shown a reduced decay rate upon cycling, despite a lower initial reactivity owing to a lower amount of CaO per unit mass (Dobner, Sterns et al. 1977; Silaban, Narcida et al. 1996); natural sorbents such as shells have also been studied and have been shown to exhibit mildly increased reactivity in comparison to natural limestone in some cases (Ives, Mundy et al. 2008; Li, Zhao et al. 2009). Doping of natural limestones has been investigated; however the results have been variable (Salvador, Lu et al. 2003; Sun, Grace et al. 2006; Fennell, Davidson et al. 2007b; Florin and Harris 2008b), even when the same dopant has been used. The efficacy of doping is highly dependent on the concentration of dopant used; too low a concentration will have no effect, too high may contribute to pore blocking and potentially agglomeration of particles. 'Synthetic sorbents' are also being developed. Examples include: precipitated $CaCO_3$ from a slurry bubble column (Agnihotri, Mahuli et al. 1999; Gupta, Iyer et al. 2004; Florin and Harris 2008c) Florin and Harris, 2008c) to enhance the reactive surface area of the sorbent; sorbents derived from different calcium precursors, e.g., calcium acetate, calcium ethanoate (Lu, Reddy et al. 2006; Lu, Khan et al. 2008; Liu, Low et al. 2009) with particular success using a MgO support (Liu, Feng et al. 2010) to similarly enhance the reactive surface area; dispersal of CaO within an inert porous matrix such as mayenite (Li, Cai et al. 2005; Pacciani, Müller et al. 2008a) to improve mechanical stability; and use of cementitious binders (Manovic and Anthony 2009a; Manovic and Anthony 2009b) to improve mechanical stability. Sorbent reactivity can be periodically improved by hydration of calcined sorbent, though this is often at the expense of mechanical strength of the sorbent (Hughes, Lu et al. 2004; Manovic and Anthony 2007; Fennell, Davidson et al. 2007b; Manovic, Lu et al. 2008; Sun, Grace et al. 2008; Zeman 2008). Thermal preactivation / pre-treatment, by treating sorbent at high temperature under N_2, has been found to improve long-term reactivity of sorbents (Manovic and Anthony 2008a; Manovic, Anthony et al. 2008b).

All studies of sorbent enhancement should consider that sorbent reactivity is dependent on several variables: calcination temperature and time; carbonation temperature and time; CO_2 concentration in carbonation and calcination; and, the difficulty in defining 'normal' behaviour in a limestone, which may be used as a reference. These factors are important, in that they make comparisons between different studies difficult. For example, very different results are obtained for deactivation rates when calcination is conducted under mild vs. severe conditions (Grasa and Abanades 2006; Manovic and Anthony 2008a; Manovic and Anthony 2008c; Manovic and Anthony 2009a; Wang, Ramkumar et al. 2010) and also due to increases in carbonation temperature (Manovic and Anthony 2008c) (both of which are reported to be due to the effect of sintering). Longer carbonation times can regenerate the sorbent (Barker 1973; Lysikov, Salanov et al. 2007; Chen, Song et al. 2009) though the effect of this is somewhat inconsistent elsewhere (Manovic and Anthony 2008c). A higher CO_2 concentration during carbonation has been shown to improve the uptake of some synthetic sorbents (Pacciani, Müller et al. 2008b). In cases where the CO_2 concentration is higher during calcination this consistently leads to a more rapid drop-off in reactivity (Li, Cai et al. 2005; Lu, Hughes et al. 2009); however there are cases where the effect of CO_2 concentration in calcination is only noticeable over the first five cycles (Manovic and Anthony 2009a). The presence of SO_2 leads to a reduction in carbonation reactivity owing to the competing sulphation reaction (see Section 1.1.1.1).

1.1.1.3. Economics of the Ca-looping Cycle

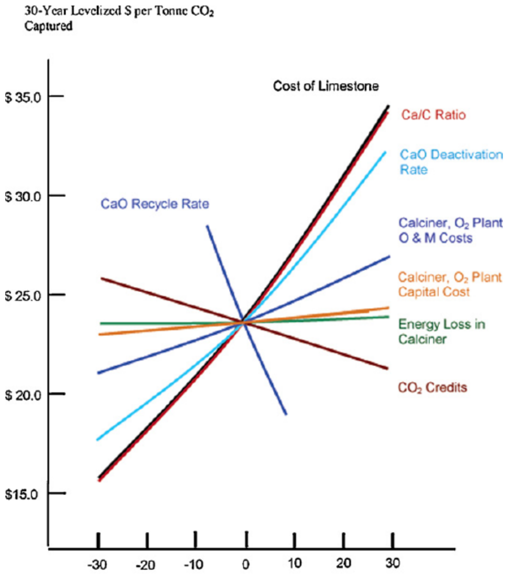

Figure 1-5. Sensitivity analysis showing the impact of varying critical cost parameters by ±30% on CO_2 capture cost (MacKenzie, Granatstein et al. 2007)

The economics of the Ca-looping cycle have been evaluated by (Abanades, Grasa et al. 2007) considering three main cost components: the main power plant, the oxy-fired calciner and the carbonator. They calculated a likely range of costs from 7.1 USD / tCO_2 to 31.2 USD / tCO_2 avoided, incorporating an optimistic and pessimistic estimate using data from the IPCC Special Report on CSS (i.e., for fuel cost, capital cost, variable cost and fixed charge factor) (Metz, Davidson et al. 2005) reflecting the impact of different cost parameters on the overall cost of capture. (MacKenzie, Granatstein et al. 2007) estimated the cost of CO_2 avoided at 19 USD / tCO_2 which compares competitively with estimates for amine scrubbing, e.g., 32.5 – 80 USD / tCO_2(Herzog 1998; David and Herzog 2000) (figures converted to 2006 USD from Canadian dollars, using mean exchange rate June 2006). Their study included a sensitivity analysis and identified the cost of limestone and the assumed Ca / C ratio as having the most significant influence on the cost

(Figure 1-5). The parameters shown to have the most significant effect on the economics of the process were the cost of the limestone and the Ca / C ratio (i.e. the amount of limestone in the system relative to the flow of CO_2 to the carbonator from the combustor).

(Romeo, Lara et al. 2009b) examined the impact on the cost of CO_2 avoided of varying the Ca / C molar ratio and purge rate (as a percentage of the solids inventory); they showed that the impact of purge rate on the capture cost was more significant for higher Ca / C ratios (Ca / C > 4) because at higher Ca / C ratios, increasing the purge rate does not lead to an increase in CO_2 capture capacity while the cost rises monotonically with purge rate. The study examined the effect of these process variables purging both from the carbonator and calciner. Purging from the carbonator allows a lower possible capture cost to be reached because material is removed before a further energy intensive calcination step is required. However, purging from the calciner allows material to be removed as CaO which can provide both an energy and CO_2 credit to cement production. Purging from the carbonator, the optimum configuration (i.e., resulting in the minimum capture cost) comprised a Ca / C ratio of 4 and a purge rate of 2 % giving a minimum cost of 19.8 USD / tCO_2. Purging from the calciner suggested an optimum configuration of Ca / C = 5 and a purge rate of 1 – 2 %, giving a minimum cost of 20.5 USD / tCO_2. The results showed consistently, regardless of purge location or fuel type, that the minimum costs could be achieved with higher Ca / C ratios and lower purge rates. In all cases studied the cost of CO_2 capture remained competitive (< 29 USD / tCO_2) (figures converted to USD from Euros using mean exchange rate January 2008).

1.2. Cement Production

1.2.1. Ordinary Portland Cement (OPC)

Cement is a hydraulic binder forming a paste with water, which sets and hardens following hydration reactions and creates the strength and durability of concrete. Cement is either classified by its composition or in respect to its performance-related properties by national or international standards.

However, the most common classifications are related to the European Standards for Common Cements (e.g. EN 197-1) defined by the European Committee for Standardization (BSI 2011) and the ASTM Standards (e.g. C150 / C150M and C595 / 595M) defined by the American Society for Testing and Material (ASTM) (ASTM 2009). A detailed overview of the different cement classifications is given in (Jackson 2007). Portland cement or 'Ordinary Portland Cement' ('OPC') forms by far the most significant proportion of cements produced today.

1.2.2. Cement Production

1.2.2.1. Raw Materials

The main constituents of cement production are calcium oxide (CaO), silicon dioxide (SiO_2), aluminium oxide (Al_2O_3) and iron oxide (Fe_2O_3). Typical sources of these oxides are limestone, chalk, marl, clays (kaolinite, illite, feldspar), shale, tuff, oil shale, bauxite and iron ore (Bye 1983). These materials often contain alkalis, heavy metals, sulphate, sulphide, phosphate, fluoride and chloride compositions in low or trace concentrations (Bye 1983; Taylor 1997; Glasser, Bhatty et al. 2004). Besides natural materials, waste products from other industrial processes such as lime sludge or fly ash from coal combustion can be used. In the use of waste materials, the addition of relatively pure limestone, sand or iron ore may also be necessary (Johansen and Kouznetsova 1992) to adjust for absent chemical compounds and to achieve the required standards (Jackson 2007). A typical chemical composition of a four-component raw meal is listed below (Table 1-2). The chemical composition of the raw material entering the system is continually controlled in plant laboratories, often through automated means.

Table 1-2. Typical chemical composition of a four component raw meal (Jackson 2007).

	Limestone (% wt.)	Shale (% wt.)	Sand (% wt.)	Iron Oxide (% wt.)	Kiln feed*composition (% wt.)
Dry material used	73	22.5	4.2	0.3	-
SiO_2	1.4	37.9	95.0	2.7	20.1
Al_2O_3	0.5	16.5	1.4	6.6	6.3
Fe_2O_3	0.2	5.1	1.3	84.0	2.4
CaO	53.7	15.4	1.0	2.7	64.4
$CaCO_3$	95.9	27.5	-	-	-
Minor compounds	2.0	13	2.3	6.7	6.8

* Decarbonised material.

Cement production involves the use of high temperatures, including the drying of raw materials, the endothermic decarbonisation reaction of limestone and clinker formation. The energy required is provided by the combustion of fuel, namely, coal, lignite, heavy and light fuel oil, fuel gas and / or petroleum coke (Table 1-3). These traditional fuels are being increasingly substituted by alternative fuels such as scrap tyres, waste oil, wood waste, plastic waste and refuse-derived fuel (RDF)(CEMBUREAU 1997; Pizant and Gauthier 1997; Trezza and Scian 2000; Mackes and Lightburn 2003; Mokrzycki and Uliasz-Bochenczyk 2003; Proscoandro, Mazziotti et al. 2003; Kääntee, Yevenhoven et al. 2004; Stöppel 2004; Pipilikaki, Katsioti et al. 2005; Trezza and Scian 2005; Greco and Enfil 2006; Zabaniotou and Theofilou 2008; World_Cement_News 2011), disposing waste and reducing the deletion of natural resources simultaneously. Raw minerals may also be replaced, for example iron oxide can be replaced with steel carcasses from scrap tyres.

Table 1-3. Consumption of fuel at cement plants in the EU (European_Commission)

Fuel type	Consumption (%)
Petcoke (fossil)	38.6
Coal (fossil)	18.7
Petcoke and coal (together)	15.9
Fuel oil	3.1
Lignite and other solid fuels	4.8
Natural gas	1.0
Waste fuel	17.9

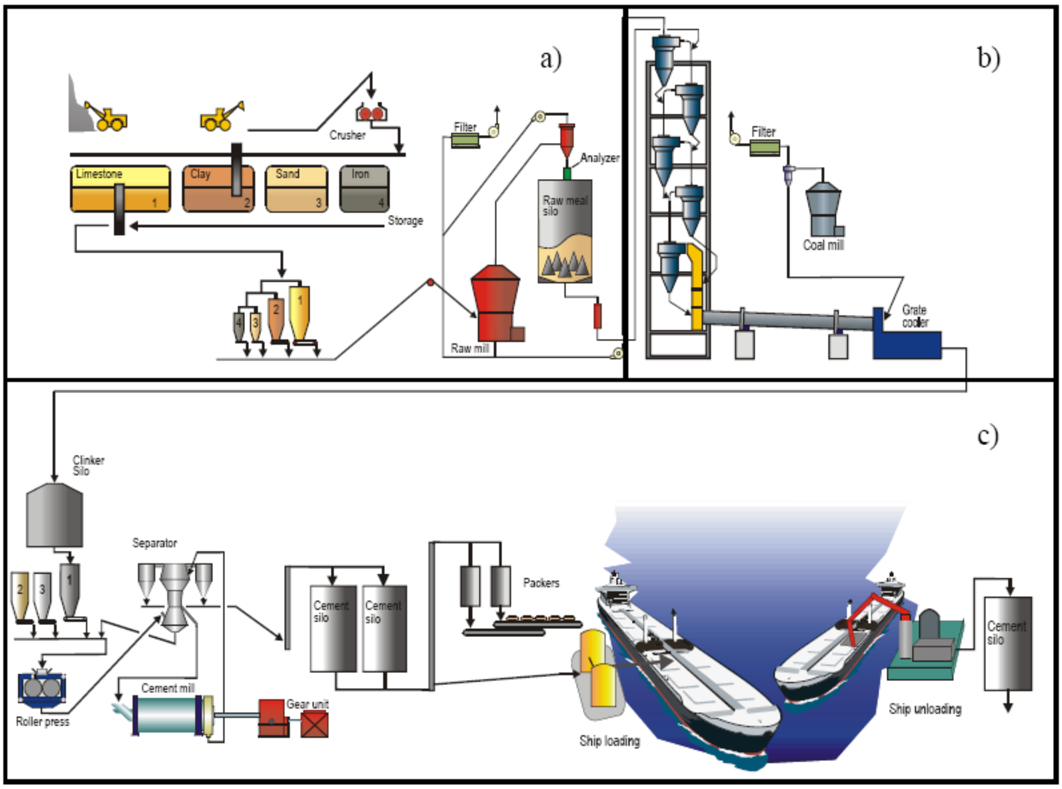

Figure 1-6. Overview of a cement production plant. a) Pre-treatment of the raw materials; b) high temperature process; c) post-treatment of clinker/cement.

1.2.2.2. Raw Meal Pre-treatment

Raw materials are first crushed and separately homogenized to provide a final product of consistent quality (Figure 1-6a). Further raw meal preparation was previously distinguished by dry- and wet pre-treatment depending on the moisture content of the raw materials. A feedstock with a moisture content of > 15 % wt. was often prepared under wet conditions where water was added in order to achieve a slurry with a water content of 25 – 50 % wt. (Bye 1983; Jackson 2007). The advantage of this method is the achievement of high raw meal uniformity. However, the use of wet kilns has decreased rapidly in recent years due to its low thermal efficiency. The more energy-efficient dry method is by far the most employed process in modern cement production. In the dry process, raw materials are ground and dried simultaneously. The blending of the different materials is carried out either by simultaneous grinding or after the grinding step by air agitation in large silos enabling homogeneity comparable to the wet method to be achieved.

1.2.2.3. Pre-heating

Clinker raw meal is pre-heated in the cyclone pre-heater (Figure 1-6b, Figure 1-7a) which is essentially a series of cyclones arranged in 50–120 m towers. Hot gases (~ 1000 K) from the precalciner and kiln heat the raw meal in counter-current flow increasing the feed temperature from ~ 200 K to ~ 800 K in less than 60 seconds (Taylor 1997). High contents of inorganic volatiles in the gases(Na, K, S and Cl) are problematic when released from the raw material or fuel in the rotary kiln as they may condense at the pre-heater walls forming solid deposits (ring build-ups) (Choi and Glasser 1988) which places limitations on the motion of gas and material around the system (Bye 1983).

1.2.2.4. Calcination

The separation of the calcination process of calcareous materials from processes in the rotary kiln enabled a reduction in kiln length or, with unchanged kiln dimensions, led to an increase in production capacity thus decreasing investment and operational costs (Bye 1983). The hot raw meal enters the calciner at about 800 K from the preheater. The energy required for the endothermic decarbonisation reaction (calcination) is obtained from hot kiln gases and additional combustion of fuel at a secondary burner taking place at temperatures of 1223 – 1273 K. In a fully-integrated process, hot air from the clinker cooler (‘tertiary’ air) is utilised as combustion air (Figure 1-7f). The consumption of fuel for calcination can account for up to 60% of fuel needed for cement production (Alsop, Hung et al. 2007). The degree of decarbonisation constitutes 90 – 95% whilst solid material enters the rotary kiln with a temperature of ~1173 K(Bye 1983).

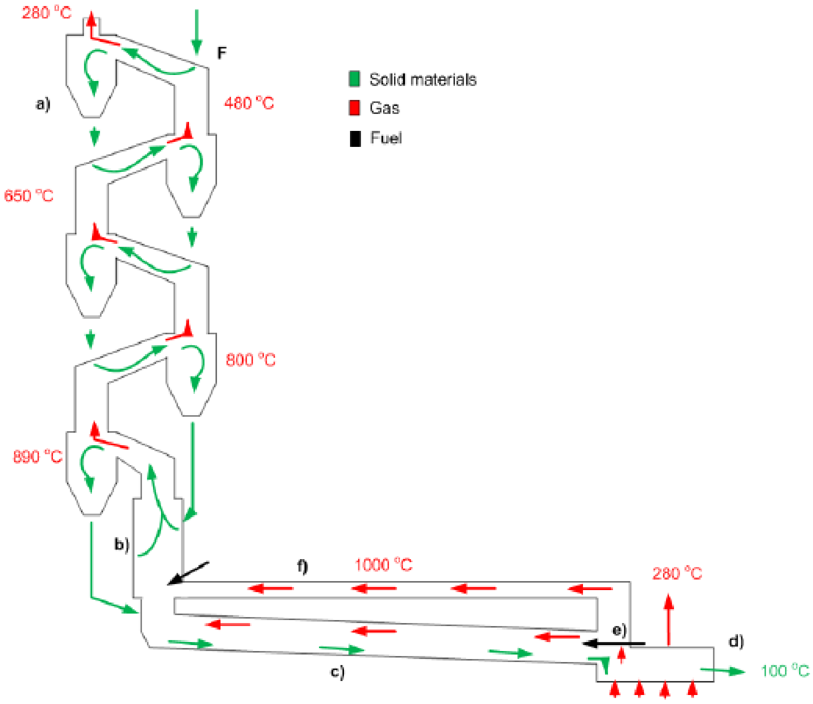

Figure 1-7. An In-line calciner pre-heater system. a) the pre-heater tower, b) the pre-calciner, c) the rotary kiln, d) the clinker cooler, e) burner and secondary air inlet, f) tertiary air pass(FLSmidth 2011).

1.2.2.5. Clinkerization

The heart of the cement-making process is the rotary kiln which varies in length and diameter depending on the design of the pyro-process system (i.e. from raw meal pre-heating through to clinker cooling). Typical dimensions for rotary kiln systems with cyclone pre-heater and precalciner are 50–100 m in length and 3–7 m in diameter (length to internal diameter ratio ~11–16) (Alsop, Hung et al. 2007). These kilns operate typically at a tilt of 1 – 3 ° from the horizontal and with a rotation velocity of 2 – 4.5 rev / min resulting in material kiln retention times of ~ 20–40 min (Alsop, Hung et al. 2007) The pre-calcined solid meal is fed into the kiln at the higher end whilst fuel, 'secondary' air (hot combustion air drawn in from the cooler – Figure 1-7e) and primary air (a much smaller air stream in comparison to secondary and tertiary air streams – as a means of controlling the flame temperature) is blown into the kiln and combusted at the lower end creating a flame with temperatures of around 2200K (Klauss 2000) (Figure 1-7e). The calcined meal moves counter current to the hot gases toward the hot region (sintering zone) of the kiln thereby achieving heat transfer between gases, solids and the kiln walls. The calcined feed is heated up to ~ 1700 K leading to reactions and mineralogical changes in the different zones of the kiln. These reactions include decomposition of the remaining uncalcined $CaCO_3$ and formation of the clinker phases which are alite and belite. At temperatures of up to 1400 K solid state reactions occur enabling the belite, aluminate and ferrite phases to be gradually formed. In addition, at these temperatures, inorganic volatiles are released from the feed material and fuel consisting mainly of alkalis, sulphates and chlorides, which condense and form deposits as rings inside the kiln. Melting of the aluminate, ferrite and to some extent the belite phase occurs at higher temperatures (1573 – 1723K) forming a liquid phase which leads to solid particles sticking, referred to as granulation / nodulisation. Lastly, 'free' (excess) CaO and belite react to form alite (Bye 1983).

1.2.2.6. Clinker cooling

Controlled clinker cooling is very important for clinker quality and for the energy efficiency of the overall production process since it enables heat recovery as depicted in Figure 1-7. It is essential that the hot clinker is cooled down quickly to below 1200 – 1250 °C as fast cooling causes the re-crystallisation of the finely grained aluminate phase (Bye 1983) which results in a desirable slow, controllable hydration reaction during the cement setting process. Conversely, a coarsely grained aluminate phase formed due to low cooling rates causes overly rapid setting of cement (Jackson 2007). In addition, the important alite clinker phase is only thermodynamically stable at temperatures above 1250 °C. Below 1250 °C, alite decomposes into belite and calcium oxide (Figure 1-8) (Mohan and Glasser 1977). Rapid cooling to temperatures below this critical temperature results in metastable alite.

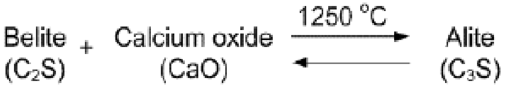

Figure 1-8. The formation and decomposition reaction of alite

Lastly, the higher the cooling rate, the higher the heat recovery which improves the energy efficiency of the cement production process (Bye 1983).

1.2.2.7. Cement Blending and Grinding

For the preparation of cements, clinker needs to be ground and blended with additives (Figure 1-6c), the most important of which are gypsum or anhydrite which control the setting of concrete during hydration. Other additives are for example blast-furnace slag, limestone or fly ash depending on the desired cement type (Bye 1983; Johansen and Kouznetsova 1992; Dunstetter, de Noirfontaine et al. 2006; Jackson 2007).

1.2.3. Cement Chemistry

Cement chemistry is a complex topic; some of the processes involved are still not yet fully understood. However, a summary of the essential chemistry relevant to the four main clinker phases is given here.

1.2.3.1. Clinker Phases

Cement clinker is comprised of four main phases, all containing CaO. These phases are commonly referred to in shorthand within the cement industry (Table 1-4).

Table 1-4. Abbreviation of the chemical formulae used in the cement field (Bye 1983)

Chemical compound	Abbreviation	Clinker phase	Clinker phase Abbreviation
CaO	C	Ca_3SiO_5	C_3S
SiO_2	S	Ca_2SiO_4	C_2S
Al_2O_3	A	$Ca_3Al_2O_6$	C_3A
Fe_2O_3	F	$Ca_4Al_2Fe_2O_{10}$	C_4AF
$Ca_{12}Al_7O_{33}$		$C_{12}A_7$	

In OPC the four main phases appear in order of prevalence; tricalcium silicate (C_3S); dicalcium silicate (C_2S); tricalcium aluminate (C_3A) and tetra-calcium alumino-ferrite (C_4AF). The first two are responsible for cement strength and commonly contain impurities; in their impure form these are commonly known as alite and belite respectively. Tricalcium aluminate (C_3A) incorporates impurities such as Si^{4+}, Fe^{3+}, Na^+ and K^+ and is the most reactive of the clinker phases

Alite (C_3S)

Alite is the most important clinker phase in cement since it controls mainly the initial and ultimate strength of cement. OPC clinker consists of ~ 50 – 70 wt. % of alite which contains 71 – 75 % wt. CaO, 24 – 28 % wt. SiO_2 and 3 – 4 % wt. substituted ions (Taylor 1997). Ions typically incorporated within the alite crystal lattice are Mg^{2+}, Al^{3+} and Fe^{3+}. The impurities in alite stabilize high temperature polymorphs at low temperatures (below the related decomposition temperature) (Maki and Goto 1982). So far, there exist seven known polymorphs between room temperature and 1343 K: three triclinic (denoted with T), three monoclinic (M) and one rhombohedral (R) polymorph (Figure 1-9) (Bye 1983; Taylor 1997; Dunstetter, de Noirfontaine et al. 2006). Due to incorporations in the alite crystal lattice, M_1 and M_3 polymorphs are present mostly in industrial clinker. Inversion of the R polymorph to M_3 and further more to M_1 occurs when cooling clinker from 1723 K, forming small crystals (M_3) rich in substituents or large crystals but poor in substituted ions (M_1). Especially, high MgO- concentrations promote high nucleation, resulting in formation of small automorphic M_3-

crystals (Maki and Goto 1982; Taylor 1997). The different polymorphs do not show significant differences in their hydraulic properties (Bye 1983).

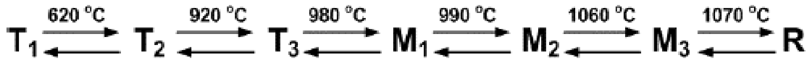

Figure 1-9. Temperature dependence of the 7 polymorphs of pure tricalcium silicate (alite) (Taylor 1997).

Belite (C_2S)

The second most prevalent clinker phase in OPC is belite. Its hydration products develop similar strength in cement as alite, only much more slowly. Belite makes up between 15 and 30 % wt. of OPC clinker and consists of 60 – 65 % wt. CaO, 29 – 35 % wt. SiO_2 and 4 – 6 % wt. substituted oxides, mainly Al_2O_3 and Fe_2O_3, but also K_2O, Na_2O, MgO, SO_3 and P_2O_5. Belite crystallizes in five polymorphs: α-belite, α'H-belite, α'L-belite, β-belite (H = "high" and L = "low" symmetry) and γ-belite (Figure 1-10), which differ in structural and hydraulic properties. The α'- polymorphs are the most hydraulic forms of belite, whereas γ-belite is a non-hydraulic polymorph and does not account for the setting and hardening of cement. β-belite is also a hydraulic polymorph, the most common in industrial OPC, but less hydraulic than the α'- polymorphs. A phenomenon that needs to be prevented through the inclusion of trace compounds is disintegration (dusting) of clinker. This happens if β-C_2S is not stabilized during cooling and / or by inclusions affording a part β-γ-C_2S inversion. γ-C_2S crystals are less dense (more voluminous) than β-C_2S crystals and cause cracking of other β-C_2S crystals, forming a voluminous powder and dust (Imlach 1976; Bye 1983; Taylor 1997).

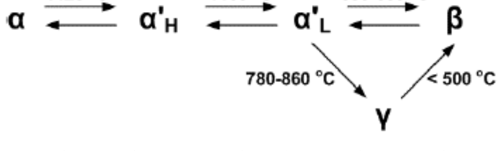

Figure 1-10. Temperature dependence of the five polymorphs of pure dicalcium silicate

Tricalcium Aluminate (C_3A)

C_3A constitutes 5 – 10 % wt. of OPC clinker and is the most reactive component. Pure C_3A consists of 62 % wt. CaO and 38 % wt. Al_2O_3 and does not exhibit temperature dependent polymorphs. However, ion substitution of Ca^{2+} in the structure of the pure C_3A causes changes in crystal structure. Typically Ca^{2+} is substituted by Mg^{2+}, 2 K^+ and 2 Na^+, Al_{3+} by Fe^{3+} and Si^{4+}, but only the alkali metals affect the structural changes (Bye 1983; Taylor 1997) from a cubic crystal structure (pure C_3A) to orthorhombic and monoclinic structures via intermediate structures of lower symmetry. In industrial clinker products, orthorhombic and cubic structures are the most common polymorphs. The orthorhombic form features dark, prismatic crystals, whereas the cubic polymorph forms fine grains with dendritic ferrite crystals.

Calcium Aluminoferrite (C_4AF)

Calcium aluminoferrite constitutes 5 – 15 % wt. of OPC (Taylor 1997). The pure phase contains 46 % wt. CaO, 21 % wt. Al_2O_3, 33 % wt. Fe_2O_3, but in industrial clinker up to 10 % wt. of incorporated oxides appear (mostly MgO). This phase is composed of any solid solution composition of $Ca_2(Al_xFe_{1-x})_2O_5$, with $0 < x < 0.7$ and is typically termed brownmillerite (Mineral_News ; Mindat.org 2013) The denotation C_4AF represents only a single point in this series for $x = 0.5$. Substitution free C_4AF is yellowish brown, while substituted (Mg^{2+}, Zn^{2+}), air cooled C_4AF is black.

1.2.3.2. Clinker Phase related Equations

Several equations have been derived to describe the quality and quantity of OPC of a known raw material composition based on phase relations in the four component system. In all equations the chemical compositions are expressed in % wt. The quality of clinker is often referred to as the amount of ‘free’ (non-reacted) CaO in the sample which is known to reduce the strength of concrete (Bye 1983). Up to now many theoretically and empirical derived equations have been developed to calculate the so called “Lime Saturation Factor” (LSF) (Eq. 1-9) (Taylor 1997; Macphee and

Lachowski 2007) which is used to quantify the amount of CaO in the raw material that can be combined with SiO_2, Al_2O_3 and Fe_2O_3 to form the four main clinker phases. For satisfactory clinker quality the LSF value should be in the range of 92 – 98 % (Macphee and Lachowski 2007). Other relevant parameters are the “Silica Ratio” or “Silica Modulus” (SR or SM)” (Eq. 1-10) and the “Alumina Ratio” or Alumina Modulus” (AR or AM) (Eq. 1-11). The SR value is usually in the range of 2 – 3 and describes the proportion of the silica phases to aluminate and ferrite phases. It also reflects the ratio of solid phases (the silica phases) to the liquid phase formed by aluminate and ferrite in the kiln. AR expresses the ratio between the aluminate phase and ferrite phase and indicates which of these two phases is forming the melt phase.

$$LSF = \frac{CaO}{2.8SiO_2 + 1.18Al_2O_3 + 0.65Fe_2O_3} \cdot 100 \qquad \text{Eq. 1-9}$$

$$SR\ or\ SM = \frac{SiO_2}{Al_2O_3 + Fe_2O_3} \qquad \text{Eq. 1-10}$$

$$AR = \frac{Al_2O_3}{Fe_2O_3} \qquad \text{Eq. 1-11}$$

A method used to determine the potential quantities of C_3S, C_2S, C_3A or C_4AF from the four major oxides contained in cement raw meal is given by the Bogue calculation. Although this calculation is known to over-predict alite content and is considered somewhat out-of-date, it is still a standard method used within the cement industry. More detailed information on the Bogue calculation can be found in (Taylor 1997).

1.3. Integration of Ca-looping and Cement Production

One major advantage for the Ca-looping cycle over many competing technologies is that the exhausted / purged CaO can be used as a raw material in cement production, presenting an opportunity to partially decarbonise both power generation and the cement process. Cement production is both a highly resource and energy intensive process. The energy consumption of producing a tonne of clinker ranges from 3.1 to 7.5 GJ (CEMBUREAU 1999) with over 60 % of the energy use in the process owing to heat input to the precalciner (EU 2001) to drive the endothermic calcination of $CaCO_3$, as mentioned previously.

The cement production process emits between 0.6 and 1 kg of CO_2 per kg of cement (ECRA 2007) and approximately 80 % of these emissions (~ 60 % from decarbonisation, ~ 20 % from calciner fuel use) originate in the calcination stage (Figure 1-11).

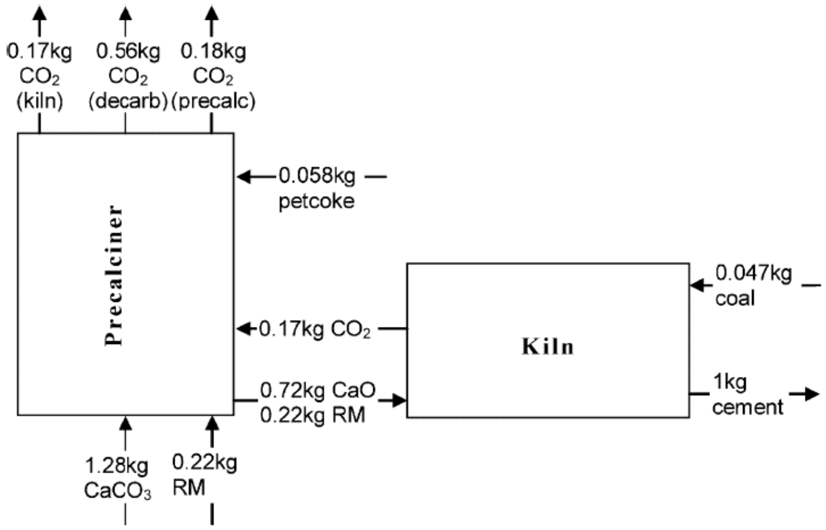

Figure 1-11. Mass balance on raw materials, fuels and CO_2 in a typical modern dry cement production process (RM = raw materials other than CaCO3). Coal LHV 26.3 MJ/kg, 68.9% carbon content. Petroleum coke LHV 34.2 MJ/kg, 87.2% carbon content. Data taken from (Alsop, Hung et al. 2007).

A means to reducing the direct emissions of CO_2 from the calcination process has been assessed which involves driving the reaction using very hot CaO particles ($T > 1273K$) passed to the precalciner from a separate combustor (Rodriguez, Alonso et al. 2008) (see Figure 1-12). This is intended to replace the conventional method of driving the calcination reaction in the cement works (i.e. in situ fuel combustion). Such a process would increase the energy requirement by 0.8 GJ / tonne cement, but allows up to 60 % of the CO_2 emissions to leave the system in a form suitable for storage (following compression and purification) at an estimated cost of 19 USD / tCO_2. This is shown to be highly competitive with other figures for cost of CO_2 avoided as determined in an economic study of CO_2 capture in the cement process using amines (144 USD / tCO_2) and using an oxy-fired kiln configuration (54 USD / tCO_2) (Barker, Turner et al. 2009).

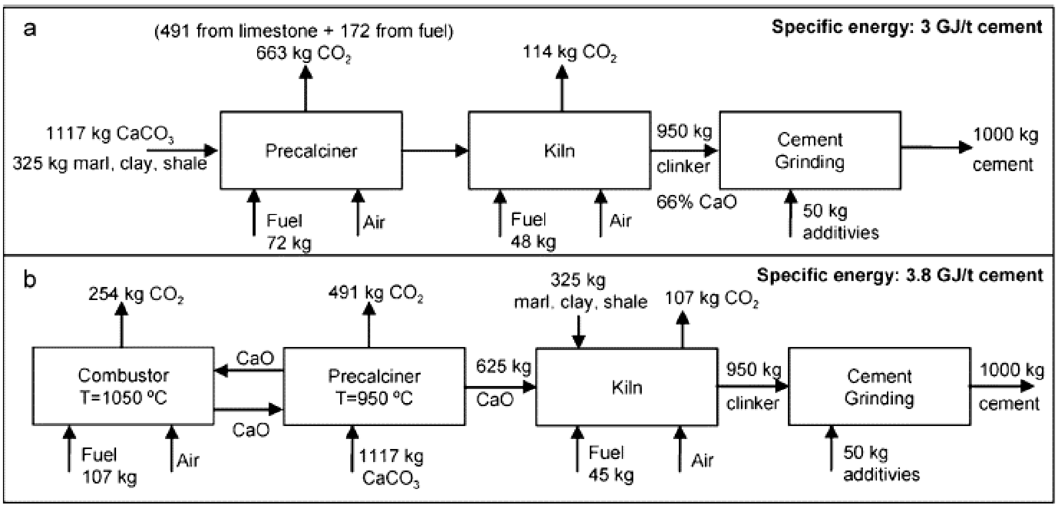

Figure 1-12. Mass balance on (a) a reference cement plant and (b) the novel CO_2 mitigation strategy proposed. Basis = 1 tonne of cement, LHV 25 MJ / kg, 10 % air excess (Rodriguez et al., 2008a).

Alternatively, the purged material from the Ca-looping system (for example if applied to power generation) (Figure 1-1) which would consist predominantly of CaO (if removed at the calciner) with a proportion of ash and calcium sulphate (the proportion of which would depend on Ca-looping operating parameters) can be used in place of the $CaCO_3$ which is usually the main constituent of the cement feed. The ash content could also fulfil some or all of the cement aluminosilicate requirements usually supplied in the clay or in additives. This means that the direct emissions of CO_2 from the calcination stage are avoided in the cement works, as is a substantial amount of the energy required to effect the calcination. Basic calculations (Blamey, Anthony et al. 2010) indicate that a reasonable purge rate of ~ 48.9 kg/s (Romeo, Ballesteros et al. 2008) would otherwise require 144MWth, simply to calcine, thus theoretically reducing the energy required within the cement works for clinker manufacture of 3.1 GJ / t by approximately 50%. As a result, both of the industrial processes undergo significant decarbonisation, the energy required to produce clinker in the cement plant is almost halved, the raw material costs of the cement process are vastly reduced and the issue of waste disposal from the power plant CO_2 capture process is avoided.

The inherent advantage of integrating cement manufacture with the Ca-looping process is clear. However, the potential to use waste material from the cycle to fulfil the requirement for calcareous material in the cement process may be limited by its chemical compatibility in relation to the demands or limitations imposed on cement product composition.

The factors potentially limiting or having implications for the use of the deactivated CaO are discussed here. Firstly, due to the strong affinity of CaO to SO_2 (Eq. 1-4), a proportion of the CaO in the waste material will be in the form of $CaSO_4$. The proportion will depend upon the Ca / C ratio used in the Ca-loop, the composition of the fuel and the recycle / purge rate. The maximum sulphur content of OPC in the U.S. is 2.5 % as specified by ASTM C150 (ASTM 2009); above this level, sulphur leads to expansion and cracking of the cement paste upon hydration. (This expansion is dependent upon the alumina content; therefore this value increases to 3 % for cements with higher levels of aluminates (Figure 1-13).

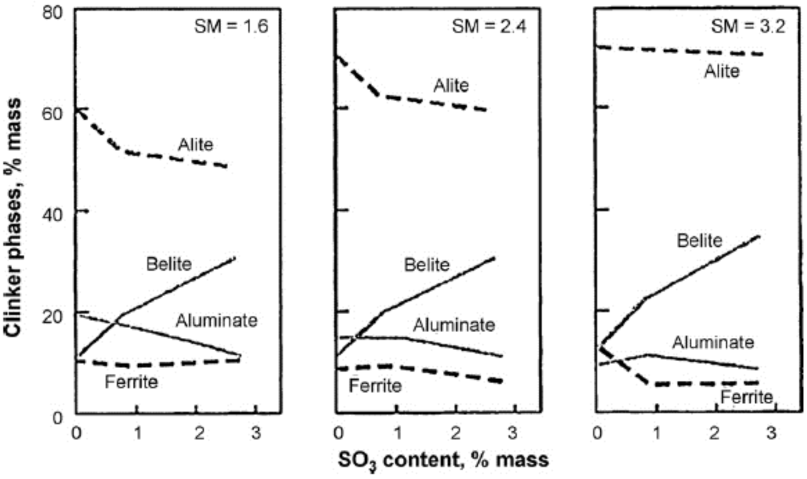

Figure 1-13. The effect of cement product SO_3 content and Silica Modulus (SM) on major phase formation (Bhatty et al., 2004).

The proportion of sulphur contained in the final cement product is also known to impact upon the formation of the four major cement compounds which determine the strength properties of the cement. An increase in sulphur content within the 0 – 3 % range has been shown to lead to a decrease in alite (the cement compound which provides long term strength development) and an increase in belite (the compound providing short-term strength development) irrespective of the Silica Modulus. A desirable level of SO_3 in OPC clinker is 0.6 % (Alsop, Hung et al. 2007). It should also be noted that excess sulphur entering the cement works can lead to operational problems arising from cycles of evaporation in the kiln and condensation in the precalciner leading to blockages.

However, in modern cement plants reasonable sulphur levels in the system and the resulting circulation can be achieved using a kiln by-pass line to remove unwanted vaporised components from the kiln (in particular K_2O, Cl and Na_2O_3 as well as SO_3). Another potential issue is that of trace elements released from fuel use in the Ca-looping calciner. The in-situ combustion of solid fuels is likely to result in partial or total vaporisation of trace elements contained in the fuel. Repeated exposure of the solids to the combustion environment over a long series of cycles could lead to a build-up of certain trace elements in the solids, either through physical or chemical attachment to the calcium oxide, calcium sulphate or the ash. These elements would therefore be present in the waste material and passed to the cement works.

A key concern for the cement industry when considering the use of a marginal raw material is its trace element content, the incorporation of the elements into the clinker and their effects on the production process and on cement performance (Bhatty 1995). Highly volatile elements such as cadmium, mercury, selenium and thallium tend to leave the cement process either in the cement kiln dust (CKD) or in the emissions and pose less of a concern for operation of the plant or for the final cement product. Less volatile elements are likely to incorporate into the clinker causing a variety of desired or undesired effects. For example, the presence of beryllium in quantities as low as 0.25 % has been shown to severely affect the setting and strength properties of cement (Bhatty 2003) due to its impact on alite crystals.

A summary of the behaviour of trace elements and their effects on alite productionis given in Table 1-5. The issue of trace elements becomes particularly relevant when the use of modified sorbents in the Ca-looping cycle are considered for integration with cement manufacture as they may contain high concentrations of certain elements / impurities.

In addition to chemical compatibility, both attrition and agglomeration of the exhausted material could impact on its use as a raw feed to the cement process. Typically the cement feed is made up of particles with the following size distribution: 88 μ (83%), 88–300 μ (15%) and >300 μ (2%) (Alsop, Hung et al. 2007). If the material is too fine due to attrition the particles would become entrained in the exhaust gas and lost in the CKD. However, if the feed is too coarse the load on the kiln would be increased due to a reduction in material burnability (i.e., the ease by which the raw materials form the clinker phases, measured in terms of the fuel consumption required to achieve these phases). This can be overcome by subjecting the material to grinding, however a grinding stage would result in a loss of the sensible heat provided by the purged CaO stream which could otherwise be used to reduce the load on the kiln.

Table 1-5. Behaviour of trace elements in the kiln and their effect on cement phases and clinker mineralogy, adapted from (Glasser, Bhatty et al., 2004)

Element	Behaviour	Impact on alite
Arsenic (As)	Volatile and therefore leaves in Cement Kiln Dust. Can also incorporate in clinker as low-volatile calcium arsenates	Reduces formation
Boron (B)		Causes decomposition Stabilises
Barium (Ba)	Replaces Ca in all clinker phases except ferrite	Reduces melt temperature and improves clinker mineralogy
Beryllium (Be)		Decomposes alite
Bismuth (Bi)	Goes into alite	
Cadmium (Cd)	Forms volatile halides / sulphates and leaves in CKD.	Reduces melt temperature Improves burnability
Chromium (Cr)		Produces dendritic belite Decomposes alite Reduces melt viscosity
Copper (Cu)	Goes to ferrite	Can adversely affect alite and belite formation Lowers melt temperature
Potassium (K)		Lowers melt temperature
Lanthanum (La)		Replaces Ca in alite and belite, forms solid solution with alite, enhances clinkering
Lithium (Li)		
Magnesium (Mg)		Improves burnability
Manganese (Mn)		Can replace Si and Ca in alite
Sodium (Na)		Lowers melt temperature
Nickel (Ni)	Goes to ferrite	Replaces Ca in alite and stabilises monoclinic form
Antimony (Sb)	Incorporates in clinker as calcium antimonates under oxidizing conditions and high temperatures	Reduces size of alite and belite crystals.
Tin (Sn)	Stays in clinker	Decomposes alite Produces dendritic belite No effect in traces
Strontium (Sr)		Small amounts favour alite formation Large amounts cause belite formation Promotes free lime formation
Titanium (Ti)	Goes to ferrite	Decomposes alite to belite Reduces melt temperature
Vanadium (V)	Goes into alite	Forms larger alite crystals Produces ragged belite Reduces melt viscosity
Tungsten (W)	Reduces melt viscosity	Forms large round alite and Type III Belite crystals
Yttrium (Y)	Substitutes	Ca in alite and belite
Zinc (Zn)	Enters belite and alite	Modifies alite crystals, reduces free lime, improves clinkering
Zirconium (Zr)		Modifies alite and belite crystals

Chapter 2. Flowsheeting

2.1. Chapter Summary

The aim of this chapter is to find the change in thermal efficiency of 1 kg clinker (η_{ck}) after integration of a generic dry cement process with the Ca-looping process such that some of the CO_2 from the cement process can be captured. This has been achieved by first producing flow-sheets of the two independent processes to then enable them to be integrated into a single process under different realistic configurations.

2.2. The Calcium Looping Process

Flowsheeting of the Ca-looping process has been carried out to enable calculation of the thermal efficiency of the process (H_{in} / F_{CO2} MJ where H_{in} = the heat demands at the calciner and F_{CO2} = the flow of CO_2 to the carbonator in kmols,) under different sets of conditions. The most fundamental parameters used as variables in this investigation are the sizes of the purge / replenishment streams (F_0) and solids recycle rate (F_R) relative to the amount of CO_2 coming into the carbonator (F_{CO2}) (Figure 2-1). CO_2 capture efficiency of the carbonator (E_{CO2}) and the average reactivity of the sorbent ($\bar{x}_C$) are also both important parameters that need to be calculated from F_0 and F_R; $\bar{x}_C$ is also required to calculate H_{in} as will be seen below.

Nomenclature for Figure 2-1 (all in kmol)	
F_{CO2}	the flow of CO_2 to the carbonator
F_0	purge / replenishment streams (relative to the amount of CO_2 coming into the carbonator)
F_R	solids recycle rate (relative to the amount of CO_2 coming into the carbonator)
E_{CO2}	CO_2 capture efficiency of the carbonator
$\bar{x}_C$	the average reactivity of the sorbent

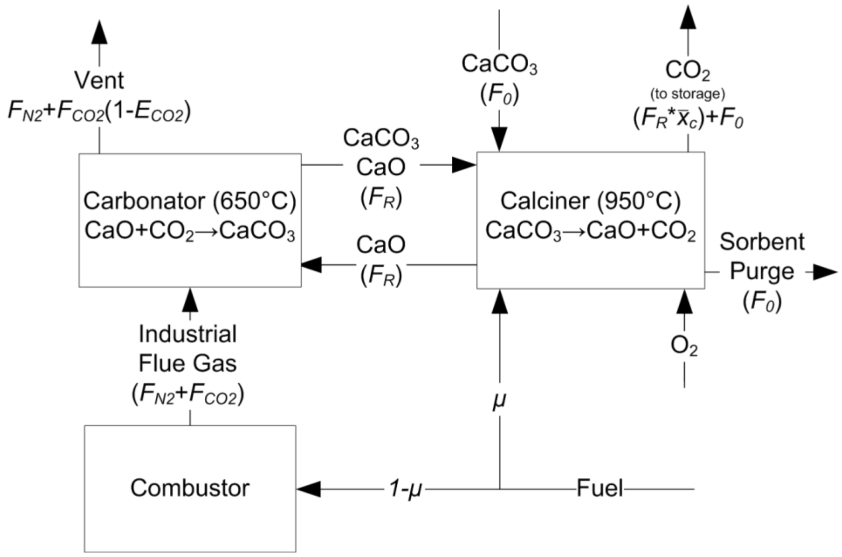

Figure 2-1. Basic flow-sheet of the Ca-looping System. (all flows in moles) Other nomenclature not mentioned in the text: F_{N2}= N_2 to the carbonator, $\bar{x}_c$ = maximum average conversion of solids in the system, μ=split of fuel to the calciner. Industrial flue gas CO_2 concentration (f_{CO2})=15 % v/v.

Other flows of interest include the vent stream which is primarily comprised of the N_2 which passes through the carbonator without reaction plus the CO_2 coming from the combustor which is not reacted with the sorbent in the carbonator (F_{CO2}*[1-E_{CO2}]). The total amount of high purity CO_2 leaving the calciner is equal to the number of moles in the recycle reacted in the carbonator ($F_R*\bar{x}_c$) plus the number of moles of CO_2 entering in the replenishment stream (F_0). The split of fuel use between the combustor and the calciner is represented by μ where μ is the split of fuel going to the calciner.

2.2.1. Determining $\bar{x}_c$ and E_{CO2} for a steady-state system

Abanades obtained an equation for E_{CO2} for a steady-state system via a mass balance on the carbonator, essentially as the amount of CO_2 captured in the carbonator ($[F_R+F_0]*\bar{x}_c$) divided by the total amount of CO_2 coming into the carbonator ($F_{CO2}+F_0$) (Eq. 2-1) (Abanades 2002).

$$E_{CO2} = \frac{(F_R + F_0)\bar{x}_c}{F_{CO2} + F_0} \qquad \text{Eq. 2-1}$$

Eq. 2-1 requires estimation of $\bar{x}_c$ to determine how much of the CO_2 is leaving in the recycle and purge after conversion to $CaCO_3$. $\bar{x}_c$ is estimated through summation of the product of conversion as a function of cycle number (a_n – See: Eq. 1.8, Background) and the mass fraction of particles for each cycle (r_k):

$$\bar{x}_c = \sum_{k=1}^{k=} r_k x_{c,k} \qquad \text{Eq. 2-2}$$

The mass fraction of particles for each cycle is calculated by performing a succession of cycle mass balances to find the mass fraction of particles that have circulated 'N' times (otherwise referred to as the age distribution) as a function of F_0 and F_R (Eq. 2-3 - Eq. 2-5):

$$r_1 = \frac{F_0}{F_0 + F_R} \qquad \text{Eq. 2-3}$$

$$r_2 = \frac{r_1.F_R}{F_0 + F_R} \qquad \text{Eq. 2-4}$$

$$\vdots$$

$$r_N = \frac{F_0 {F_R}^{N-1}}{(F_0 + F_R)^N} \qquad \text{Eq. 2-5}$$

As described, E_{CO2} is dependent on the age distribution r_N. This value can also be calculated by another means. A stochastic population balance model has been developed as part of this PhD to calculate the age distribution r_N using an iterative procedure. The model essentially utilises a vector whose values represent the number of times a given quantity of CaO (a 'packet', e.g. 100 moles) has been cycled through the Ca-looping system. On each cycle of the model, the existing packets have their ages increased by one, whilst a fraction of the total CaO in the system is purged by removing a given number of cells from the vector randomly. These cells are replaced with 'fresh packets' whose ages are equal to one (Figure 2-2).

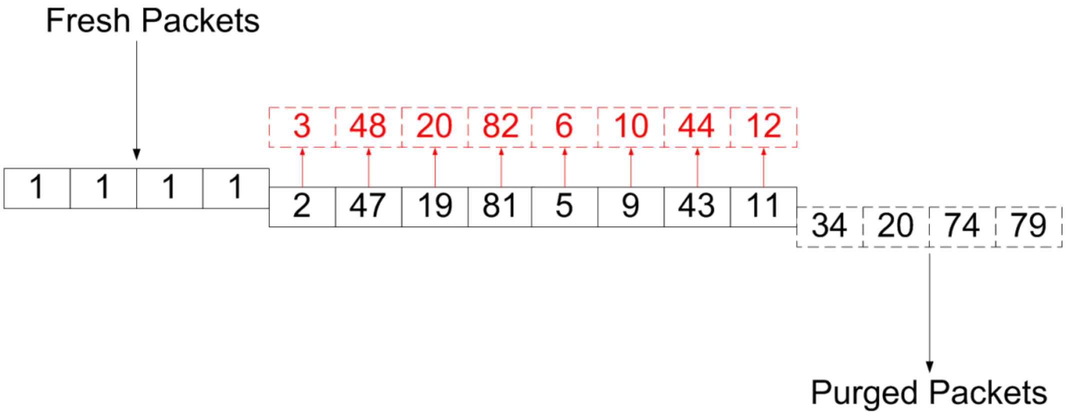

Figure 2-2. Schematic diagram depicting the procedure for establishing an age distribution via the stochastic model on each cycle.

As in the INCAR method described above, this method allows the age distribution to be calculated as a function of F_R and F_0. However, the stochastic method has an inherent advantage in that it enables the degradation in reactivity to be calculated on a time basis (as opposed to steady-state) and therefore allows real data for carbonation kinetics to be used as opposed to simplified representations as will be detailed below (see: section 2.2.3). The match between the results for r_N up to fifteen cycles can be observed from Figure 2-3;

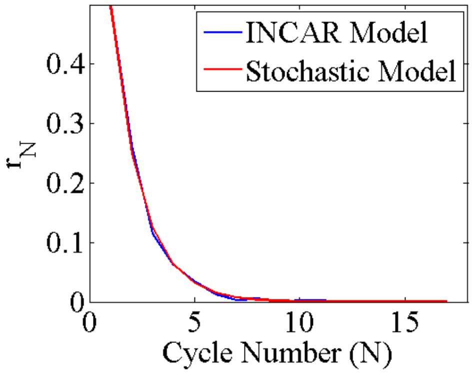

Figure 2-3. Comparison of r_N vs. cycle number for the two methods (analytical and stochastic).

As indicated in Table 2-1, the results for $\bar{x}_c$ calculated using the stochastic method also match those of the results reported by INCAR to 3 d.p. This is to be expected given that $\bar{x}_c$ is dependent on r_N. (NB. The error between the values of $\bar{x}_c$ is considered acceptable for the purposes of this project.)

Table 2-1. Results for comparison of $\bar{x}_c$ for the two methods as a function of F_0 and F_R.

		$\bar{x}_c$	
F_0	F_R	INCAR	SPBM
0.1	3.55	0.1964	0.1965
0.2	2.29	0.3058	0.3055
0.3	1.83	0.3823	0.3824
0.4	1.61	0.4354	0.4351

This demonstrates that the stochastic model is also capable of calculating E_{CO2} to an acceptable degree of accuracy from Eq. 2-1 given that the equation is dependent on $\bar{x}_c$. For the annonated Matlab code for this stage of the model please see Appendix 2-1.

2.2.2. Determining the energy requirements at the calciner (η_{th})

According to (Rodriguez 2008) the total energy requirement at the calciner (MJ / moles CO_2, H_{in}) is composed of three terms and is represented by Eq. 2-6; the energy required to drive the endothermic calcination reaction ($\Delta H_{calc} = -178\ kJ/mol$), where the total amount of $CaCO_3$ to be calcined is made up of the fresh limestone stream (F_0) and the carbonated material returning from the carbonator ($\frac{F_R}{F_{CO2}}\bar{x}_c$) (first term); the energy required to raise the temperature of the solids recycle coming from the carbonator from 923 K to 1223 K (ΔT_{cal}), where the recycle stream is made up of carbonated material ($\frac{F_R}{F_{CO2}}\bar{x}_c$), unreacted material ($\frac{F_R}{F_{CO2}}(1-\bar{x}_c)$), sulphated material ($\frac{F_{CaSO4}}{F_{CO2}}$) and ash ($\frac{F_{ash}}{F_{CO2}}$) (second term); and, the energy required to raise the temperature of the fresh limestone from ambient temperature (298 K) to 1223 K(ΔT_{F0}) (third term).

$$
\begin{aligned}
n_t = {} & \Delta H_{calc}\left(\frac{F_R}{F_{CO2}}\bar{x}_c + \frac{F_0}{F_{CO2}}\right) \\
& + \Delta T_{cal}\left[Cp_{Cao}\frac{F_R}{F_{CO2}}(1-\bar{x}_c) + Cp_{Caco3}\frac{F_R}{F_{CO2}}\bar{x}_c + Cp_{CaSO4}\frac{F_{CaSO4}}{F_{CO2}}\right. \\
& \left. + Cp_{ash}\frac{F_{ash}}{F_{CO2}}\right] + \frac{F_0}{F_{CO2}}Cp_{Caco3}\Delta T_{F0}
\end{aligned}
\qquad \text{Eq. 2-6}
$$

Eq. 2-6 has been incorporated into the stochastic model. In (Rodriguez 2008), the results are reported as the heat requirement at the calciner (H_{in}) as a percentage of the total system heat requirements (H_{in} $+H_{comb}$, where H_{comb} is the energy supplied to the combustor). Essentially, the lower the fraction of the energy being added to the system which goes to the calciner, the higher the efficiency of the overall process (though it should be remembered that there would be recuperation of some of the heat added in the calciner into the steam cycle). The plot also indicates the effect of reactivation lower than the maximum conversion potential (possibly due to partial conversion in the carbonator) on the % heat requirements at the calciner. Comparisons between the two methods indicate that the stochastic model is capable of generating the same results as that of the INCAR method (Figure 2-4 a+b). This is an expected result given H_{in} is essentially dependent on $\bar{x}_C$ and that the values for r_N and $\bar{x}_C$ matched as described in the previous section.

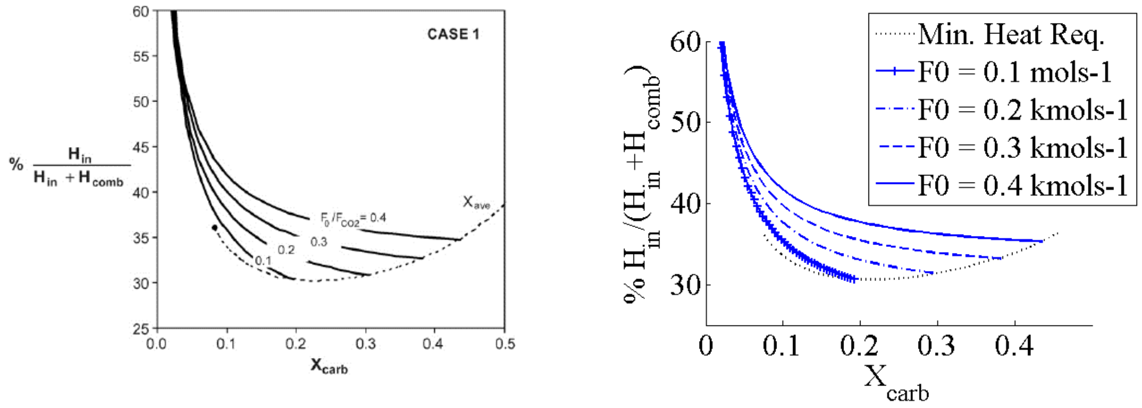
a.

b.

Figure 2-4. % H_{in} / (H_{in} + H_{comb}) for a. The INCAR model; b. the stochastic model.

The next step was to use the stochastic model to find H_{in} for different modified sorbents, namely; HBr-doped sorbent and steam-activated sorbent (data for both from Al-Jeboori, Fennell laboratory); thermally pre-treated sorbent (Manovic and Anthony, 2008a); and precipitated calcium carbonate (PCC) (Florin, Fennell laboratory). These all have degradation curves similar to that produced from Eq. 1-8 (see: Chapter 1 section 1.1.1.1) except for thermally pre-treated sorbent which has a degradation curve of a different shape (Figure 2-5c).

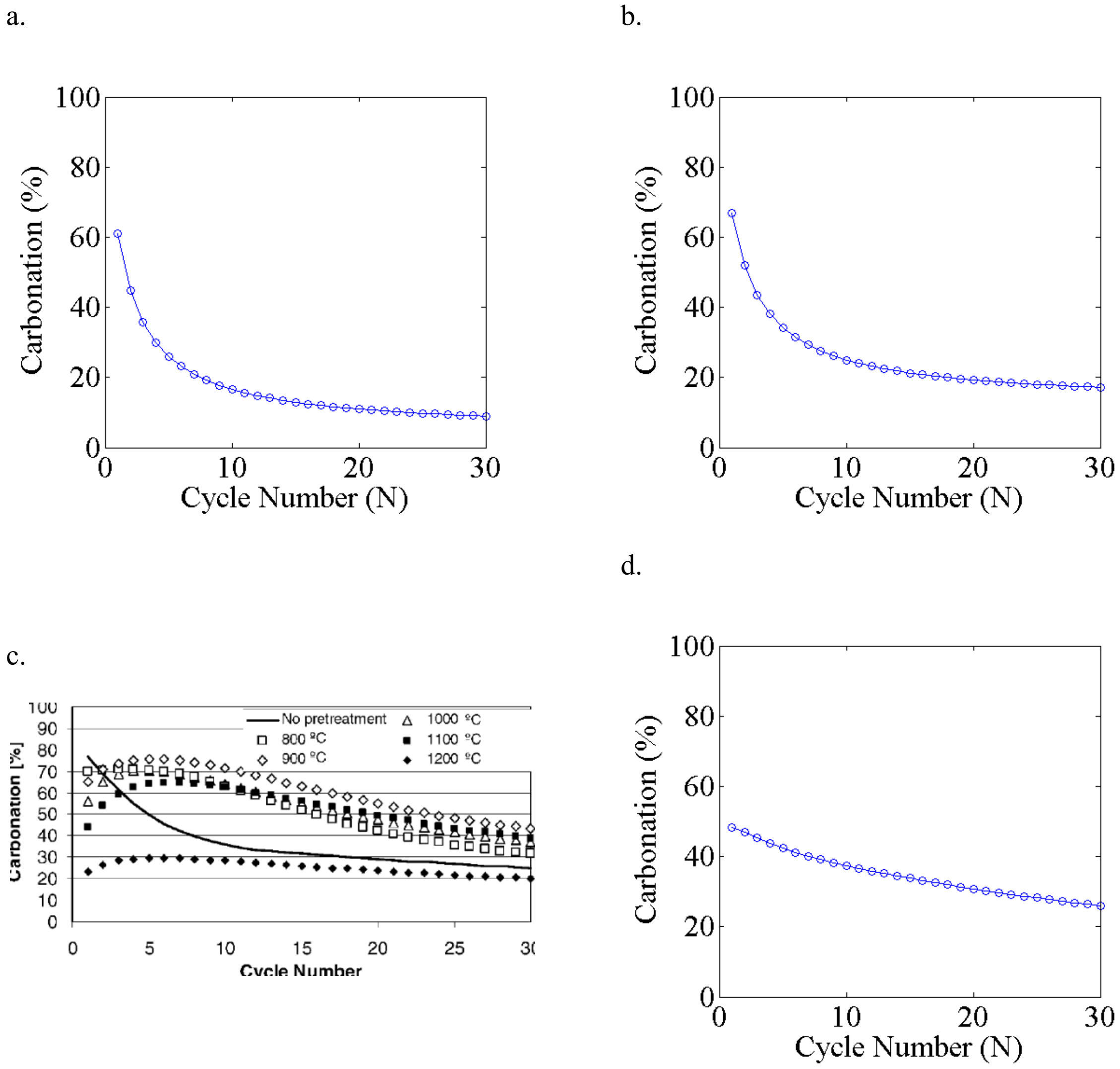

Figure 2-5. Degradation curves for a. Undoped Longcliffe, (15 % CO_2, calcination at 900 °C, carbonation at 700 °C); b. HBr-doped Longcliffe, (15 % CO_2, calcination at 900 °C, carbonation at 700 °C) c. Kelly Rock samples hydrated by steam and preheated for 24 h at different temperatures. d. Precipitated Calcium Carbonate (PCC) (15 % CO_2 during carbonation, 100 N_2 during carbonation).

All measurements except those for preheated Kelly rock limestone were fitted using equation 1-8. The experimental measurements of carbonation extent were used directly for the Kelly rock. The results of using Eq. 2-6 for the modified sorbents is given in Table 2-2 and Figure 2-6a-d. It can be seen that the thermally pre-treated sorbent results in the lowest calciner heat demand of 24.50 %. However, the energy required to thermally pre-treat the sorbent should also be factored in for a true reflection of the overall heat balance of that system.

Table 2-2. Values of H_{in} as a function of F0 for different sorbents.

	H_{in} (% total)				
F_0	Grasa	Undoped	HBr-doped	Thermal PT	PCC
0.1	217 (30.7)	262 (33.6)	207 (29.7)	177 (26.5)	205 (29.5)
0.2	224 (31.4)	248 (33.6)	222 (31.2)	203 (29.3)	227 (31.6)
0.3	244 (33.2)	259 (34.5)	244 (33.2)	231 (32.00)	251 (33.9)
0.4	268 (35.3)	279 (36.3)	269 (35.4)	258 (34.5)	277 (36.0)

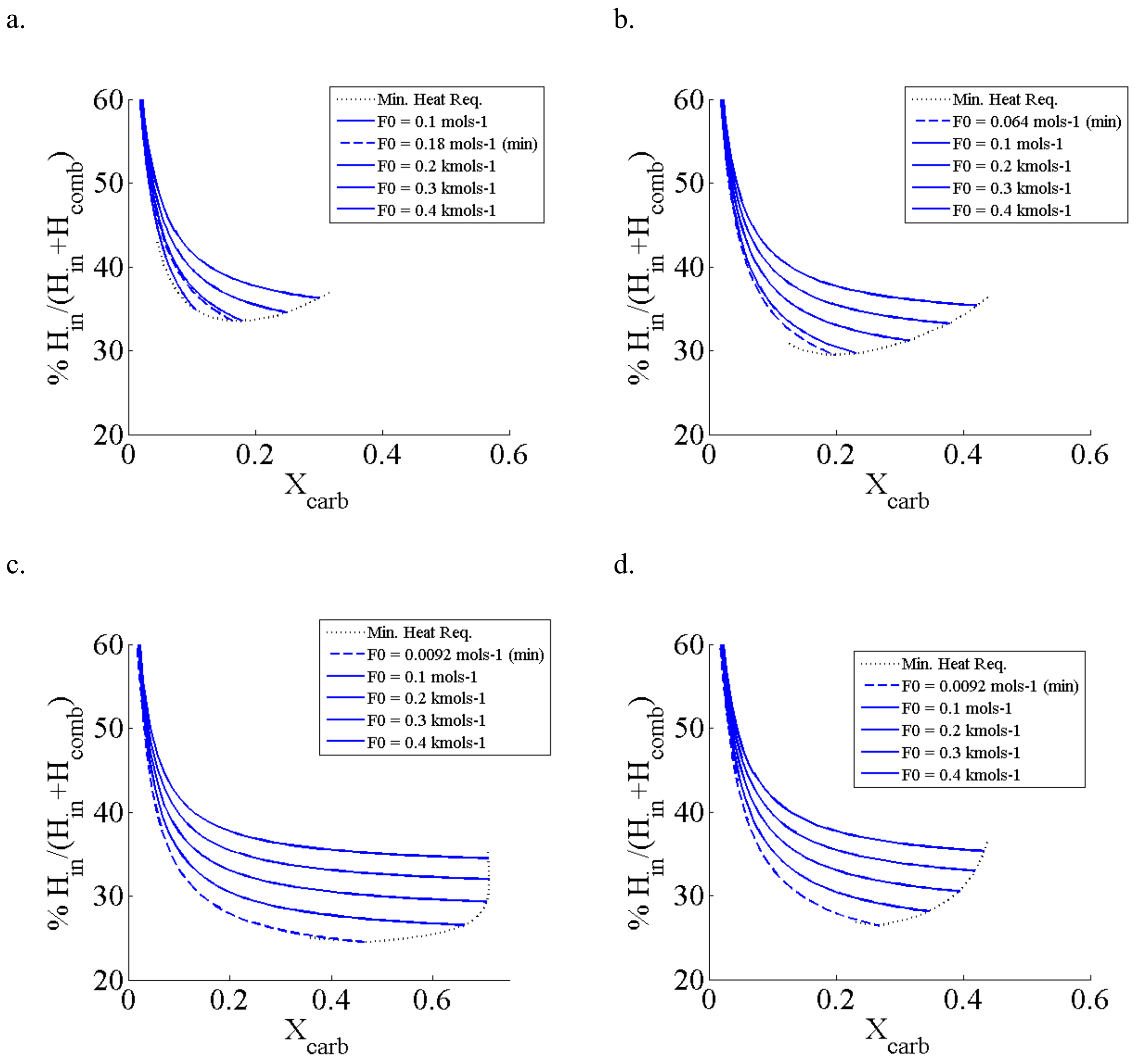

Figure 2-6. a. Undoped Longcliffe (50 cycles) b. HBr-doped Longcliffe (50 cycles) c. Thermally pre-treated / steam pre-activated Kelly Rock (30 cycles) (pretreated for 24 hrs at 900 °C) d. Precipitated calcium carbonate (30 cycles).

The undoped longcliffe has the highest minimum calciner heat demand of 33.54 %; a direct comparison can be made with Figure 2-6b which shows the results for the HBr-doped Longcliffe. It can be seen that doping the sorbent with HBr brings the heat demand down from ~ 33.54 % to ~ 29.51 %. This can be attributed to the fact that doping the sorbent results in a higher value for the final reactivity (a_{∞}) and therefore a smaller purge / replenishment stream (F_0 / F_{CO2}) can be used (0.064 rather than 0.18) whilst achieving the same value of $\bar{x}_c$. Both the thermally pre-treated and the precipitated calcium carbonate show low heat demands of 159.55 and 192.22 MJ respectively (Table 2-3). This too can be attributed to the fact that they enable the size of the purge / replenishment stream to be reduced to a near negligible amount (0.0092) whilst maintaining the same level of reactivity. However, it is important to note that such negligible purge rates may not be achievable in reality, owing to deactivation from sulphation.

Table 2-3. Optimum parameters to minimise calciner heat demands for different sorbents.

	k / X_r	$F_{0(min)}$	$\bar{x}_{c(min)}$	H_{in}	% total
Grasa	0.52 / 0.075	0.13	0.23	217.10	30.60
Undoped Longcliffe	0.72 / 0.045	0.18	0.19	248.63	33.54
HBr-doped Longcliffe	0.69 / 0.126	0.064	0.19	205.86	29.51
Thermally / steam pre-treated Kelly Rock	N/A	0.0092	0.19	159.55	24.50
PCC	N/A	0.0092	0.19	192.22	28.11

These results are of interest to cement manufacture because they will enable the overall energy penalty of the CO_2 capture process to be reduced upon integration. It is also pertinent to mention that the use of doping agents such as Br will have implications on the both the final cement product (i.e. as a trace or minor element) and also as a potential source of increased corrosion on steel components. However, the doping concentrations used are very small (Al-Jeboori, M. J. et al. 2013).

2.2.3. Incorporating Carbonation Kinetics and Bed Inventory (W_{CaO})

The next step in the work by INCAR was to incorporate bed inventories and carbonation rate kinetics into the calculation of E_{CO2}. In their work the following assumptions were made: instantaneous and perfect mixing of solids in both the carbonator and calciner; plug flow for the gas phase in the carbonator; and, instantaneous and complete calcination of particles in the calciner. It is assumed that the bed contains N_{Ca} moles of CaO but only a fraction (f_a) reacts in the bed at a rate rave (average reaction rate of the active material, s^{-1}). The remaining fraction of bed particles ($1-f_a$) are considered inactive. Simultaneously, there is a continuous arrival of newly calcined particles (F_R) that are converted in the perfectly mixed carbonator to conversion X.

To facilitate integration of the reaction rate and the residence time distributions it was assumed that the CaO particles attain the maximum conversion X_N at a constant rate in a characteristic time, t*; after that the reaction rate becomes zero (Figure 2-7 and Eq. 2-7) in line with theory regarding a fast reaction rate followed by a slow reaction regime controlled by CO_2 diffusion through the product layer formed on the free CaO surfaces as described in Chapter 1 (see: Chapter 1, section 1.1.1.1):

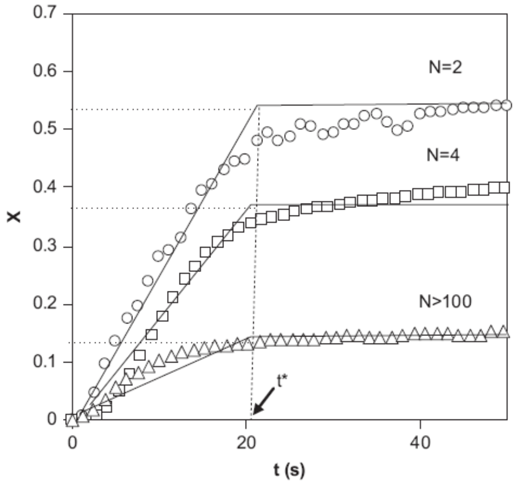

Figure 2-7. Scheme of the kinetic model adopted from (Alonso, Rodriguez et al. 2009).

$$r_{CaO} = \begin{cases} \frac{X_N}{t^*} & \text{if } t < t^* \\ 0 & \text{if } t > t^* \end{cases} \qquad \text{Eq. 2-7}$$

This equation implies that particles with a residence time above t* reach their maximum average conversion X_N, and that their reaction rate is zero from that point onwards. It is argued here however that this is an over-simplification of the actual carbonation rate and extent of carbonation (maximum conversion) as derived from experimental data. The stochastic model described previously has been adapted to enable integration of real experimental data for carbonation rate (Figure 2-8) with the residence time distribution by picking out values from vectors of carbonation conversion over time depending on how long the particle or packet has spent in the carbonator.

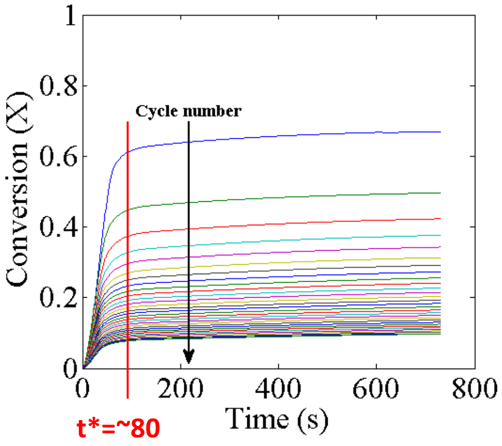

Figure 2-8. TGA data for CO_2 conversion as a function of time (Havelock). Red line indicates an approximate value for t*, whilst the black arrow indicates the direction of cycle number through the data.

This required two separate vectors to be created; one for the carbonator and one for the calciner. In each 'second' of the simulation, packets are passed around the system (i.e. between the vectors) using three stochastic functions; two between the carbonator and calciner enabling packets to be passed between the reactors at random, and a third function purging packets at random (as in the previous model described in section 2.2.1) (Figure 2-9):

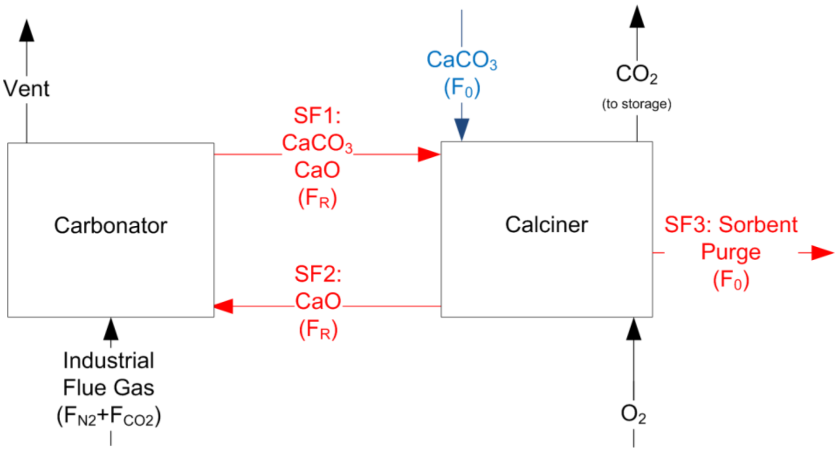

Figure 2-9. Flow-sheet of the stochastic model incorporating bed inventories into the calculation of E_{CO2}.

During the course of the simulation the residence times of packets at the carbonator are recorded depending on the number of seconds they have spent in the reactor without being passed to the calciner for regeneration. Packets which are passed to the calciner and returned to the carbonator have their ages increased by one to effect the degradation of reactivity over repeated cycles. This enables the model to 'pick out' values from the carbonation rate (e.g. Figure 2-7) based on the residence time at the carbonator and the number of cycles. E_{CO2} was then calculated as the number of moles of CO_2 reacting in each second (i.e. by summing all active packets in the carbonator based on their age and residence time) divided by the number of moles of CO_2 coming in from the combustor. A thermodynamic limit of 92 % was placed on E_{CO2} based on a flue gas concentration of 15 % v / v.

These results were then compared against those of the INCAR method. It was not possible to acquire exact values for E_{CO2} calculated via the INCAR method for reasons of confidentiality (Alonso 2013). However approximate values have been derived based on plots published in (Alonso, Rodriguez et al. 2009). The next step was to incorporate carbonation conversion from experimental data (Figure 2-10), where F_0 = the purge / replenishment rate, F_R = the solids recycle rate and W_{CaO} = the bed inventory.

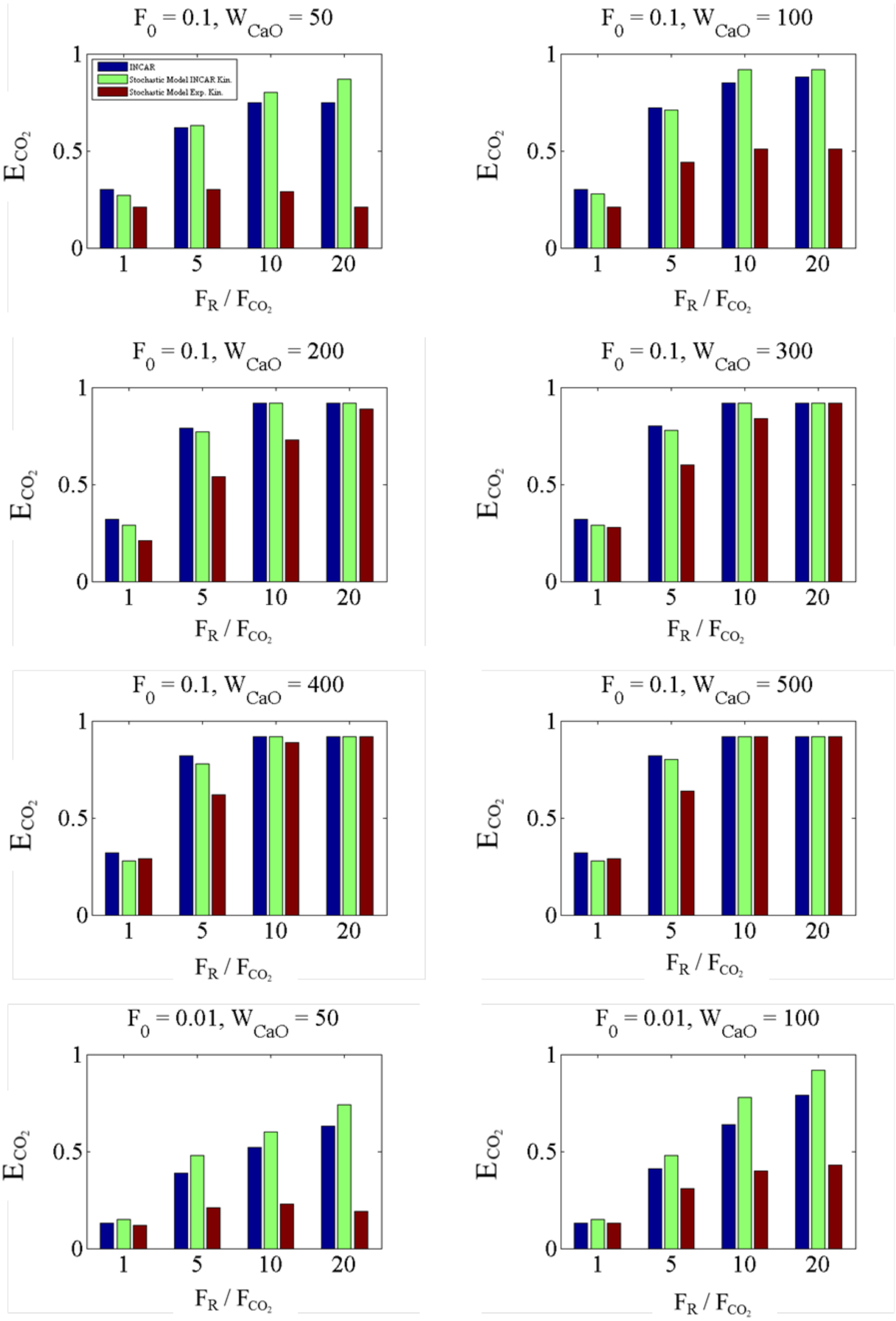
F 0 = 0.1, W CaO = 50
F 0 = 0.1, W CaO = 100
F 0 = 0.1, W CaO = 200
F 0 = 0.1, W CaO = 300
F 0 = 0.1, W CaO = 400
F 0 = 0.1, W CaO = 500
F 0 = 0.01, W CaO = 50
F 0 = 0.01, W CaO = 100
INCAR
Stochastic Model INCAR Kin.
Stochastic Model Exp. Kin.
E_{CO_2}
F_R / F_{CO_2}
0
0.5
1
1
5
10
20

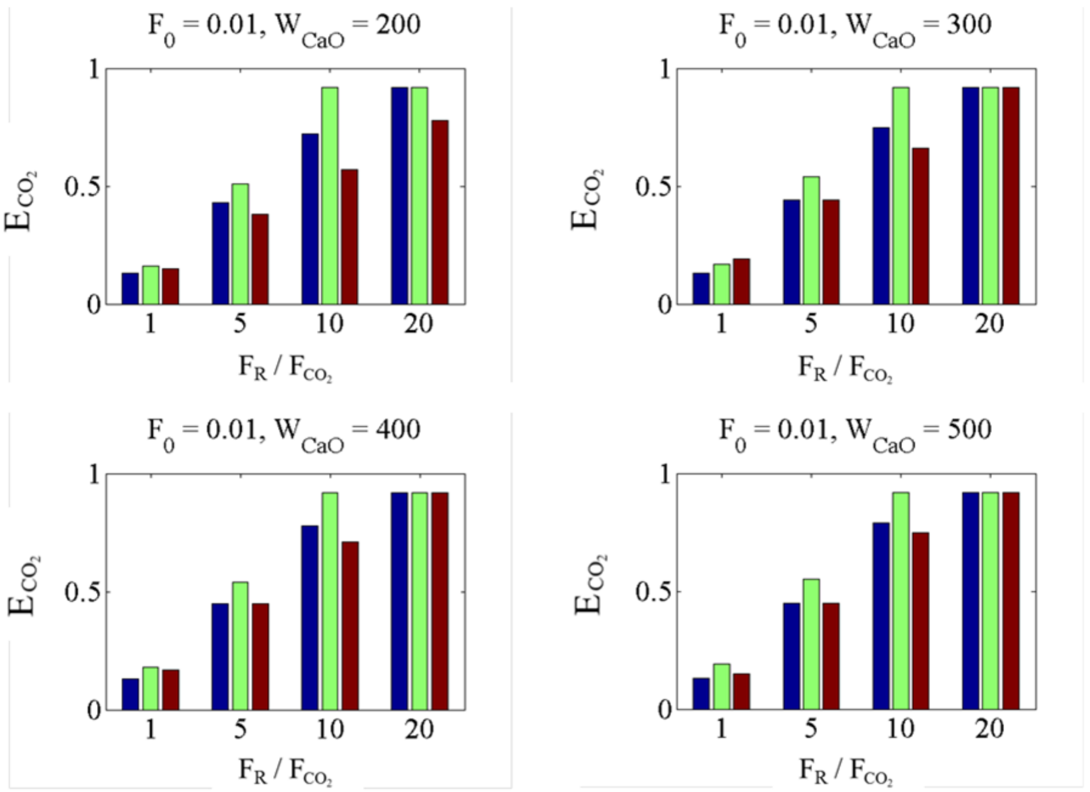

Figure 2-10. Comparison of E_{CO2} values for the two methods. Blue bars refer to the results of the published INCAR work; green lines to the stochastic method using the INCAR kinetic model; and, red lines to the stochastic model using experimental data.

The results comparing the stochastic model with the INCAR method indicate that the model yields results similar to that from INCAR; at higher purge rates (F_0 = 0.1) the stochastic model outputs values for E_{CO2} very similar to those in the INCAR results, whilst at the lower purge rates (F_0 = 0.01) the results for E_{CO2} are somewhat higher. However these differences can be attributed to the fact that a different modeling method is being used; one is based on an arithmetic series whilst the other is based on the random movement of data between two vectors. The results for the stochastic model using experimental data are consistently lower than that of both the INCAR results and the results of the stochastic model using the INCAR model. This is an expected result given that the equivalent value of t* in the experimental data is close to 80 (marked with a red line on Figure 2-8) as opposed to the 20 seconds used in the INCAR model. This means that it takes around 4 times as long for a packet to reach the maximum conversion resulting in lower carbonator CO_2 capture efficiencies. For the annotated Matlab code for this stage of the model please see Appendix 2-2.

2.2.4. Examining system start-up

As well as enabling real carbonation data to be used, the stochastic model also enables study of the start-up of the system, given that it operates on a time basis rather than being based on steady-state calculations. For example, Figure 2-10a+b show the CO_2 capture efficiency of the carbonator as a function of time.

a.

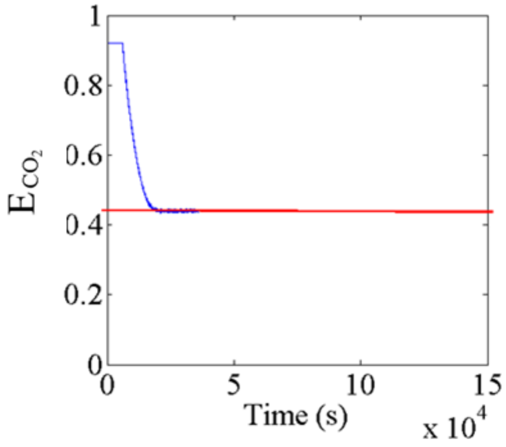

b.

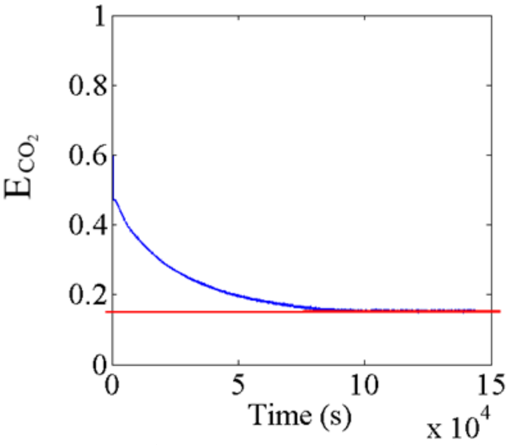

Figure 2-11. Plot of E_{CO2} as a function of time a. $W_{CaO} = 400$, $F_R = 10$, $F_0 = 0.01$; b. $W_{CaO} = 400$, $F_R = 1$, $F_0 = 0.01$

The red lines in Figure 2-11a+b indicate the steady-state values of E_{CO2} calculated by the stochastic model for fixed values of W_{CaO} and F_0 and two F_R values ($F_R = 10$ and 1 respectively). These plots show that not only does a lower recycle rate reduce the carbonator efficiency from 0.44 to 0.15, it also increases the time taken for the system to reach steady-state (defined as less than 1 % change from one second to the next) from ~ 20,000 seconds (~ 5.5 hours) to ~ 100,000 seconds (over 1 day) (Table 2-4).

Table 2-4. Time taken for E_{CO2} to reach steady state (t_{ss}) for different values of W_{CaO}, F_R and F_0.

$W_{CaO} / F_R / F_0$	t_{ss} (seconds)
500 / 10 / 0.01	~ 1250
500 / 1 / 0.01	~ 150,000
400 / 5 / 0.01	~ 20,000
400 / 1 / 0.01	~ 100,000
300 / 5 / 0.01	~ 35,000
100 / 5 / 0.01	~ 15,000

Finally, an added advantage of using the stochastic method is the ease by which extra units can be inserted, e.g. a hydrator for steam reactivation.

2.3. Cement Plant Flowsheeting

The main purpose of this chapter is to find the thermal efficiency of producing 1 kg clinker (n_{ck}) for a cement plant integrated with the Ca-looping cycle under different configurations. To do this it was first necessary to construct a mass and energy balance for a generic dry cement process. This was developed using Microsoft Excel on a basis of 1 kg cement clinker leaving the clinker cooler before the grinding stage. A description of how the mass and energy balance has been constructed is provided here.

2.1.1. Cement Plant Mass and Energy Balance

The main flows of a modern heat-integrated cement production plant are described in the schematic diagram of Figure 2-12 which shows an integrated dry cement process flow-sheet consisting of four main stages; preheater, precalciner, rotary kiln and clinker cooler. Air entering via the clinker cooler is heated by the hot clinker leaving the kiln and is passed to the kiln and calciner as preheated combustion air. O_2-depleted air leaving the kiln is then used to preheat calcined solids entering the kiln. Lastly, O_2-depleted air leaving the calciner is used to heat the solids in the cyclone preheater section. Solids enter at the preheater and are then calcined at the precalciner before being passed to the kiln. The model described here ignores the bypass gas and bypass dust lines as these do not impact significantly on the overall energy demands of the system

2.1.1.1. Calculation of gas streams through the system

The total air input into the system is comprised of air supplied to the cooler ($F_{AIR,CO}$) (2.81 kg / kgck), primary air supplied to the kiln ($F_{AIR,P}$) (0.175 kg / kgck) (both taken from (Alsop, Hung et al. 2007)) and false air infiltrating at the preheater and combustion stages ($F_{AIR,(PH)}$, $F_{AIR,(PC)}$, $F_{AIR,(KN)}$). The values for false air were taken from (Kiln_Performance_Tests_Task_Force 1992); it is possible to calculate false air using a modified Bernoulli equation (see below, section 2.1.1.3) however some of the values required for this equation were unknown and were estimated. The division of $F_{AIR,CO}$ between kiln and calciner is dependent on the fuel / air requirements at the respective combustion stages. The calculation of heat demands is given below (2.1.1.2). The split of heat demands between the kiln and precalciner therefore dictates the split of air leaving the cooler. The value for primary air is subtracted from that of the secondary air to ensure the amount of total air supplied to the kiln is sufficient but not in excess; this would otherwise lead to a lower thermal efficiency at the kiln. The remaining air from the cooler after the secondary and tertiary air is subtracted to give the value for the amount of cooler vented to atmosphere ($F_{AIR,V}$). The flow of gas from the kiln to calciner and from the calciner to the preheater consists of O_2-depleted air (N_2 and CO_2 from combustion of fuel at the kiln).

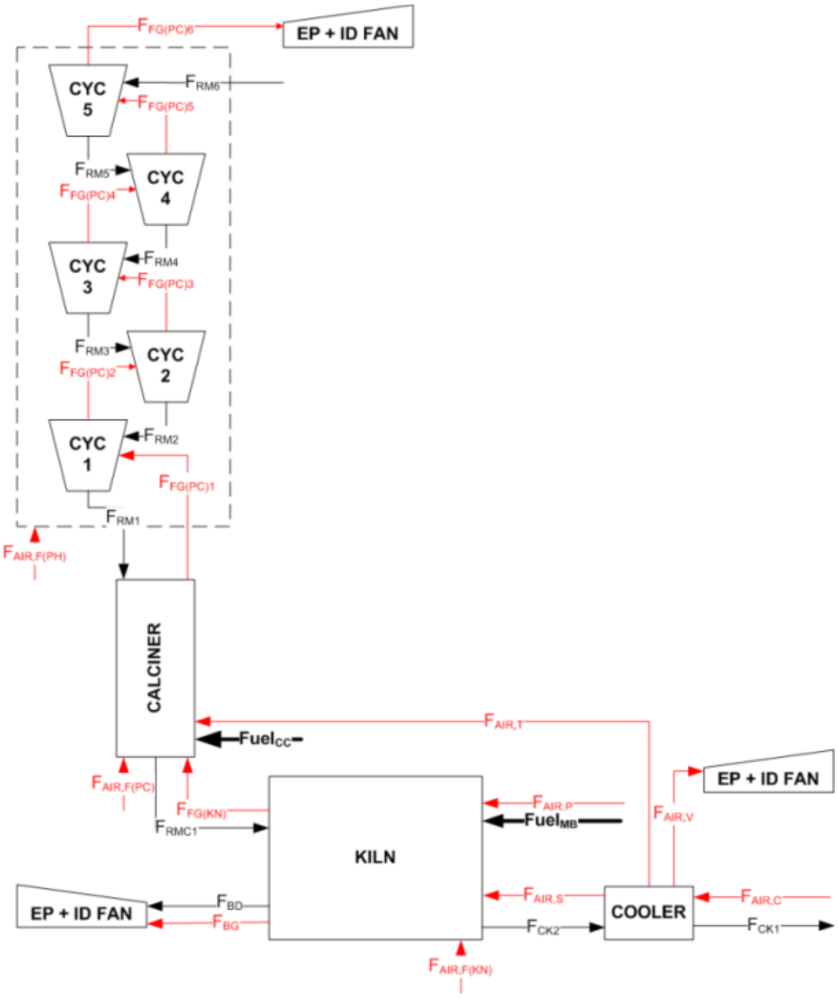

Figure 2-12. Flow-sheet of a cement rotary kiln system including cyclone preheater section, precalciner and tertiary air duct.

Table 2-5. Nomenclature for Figure 2-12.

Gas Flows		Solid Flows	
$F_{AIR,C}$	Air to cooler[1]	F_{CK1}	clinker to grinding/storage
$F_{AIR,P}$	Primary air[1]	F_{CK2}	clinker from kiln to cooler
$F_{AIR,S}$	Secondary air[2]	F_{RMC1}	Raw meal from PC to KN
$F_{AIR,T}$	Tertiary air[2]	F_{RM1-6}	Pre-heated raw meal
$F_{AIR,V}$	Vented cooler air[2]	F_{BD}	Bypass Gas Dust
$F_{FG(KN)}$	Kiln flue gas (O_2-depl. + CO_2)	$Fuel_{MB}$	Fuel at main burner (kiln)
$F_{FG(PC)1-6}$	Precalciner flue gas (O_2-depl. + CO_2)	$Fuel_{SB}$	Fuel at secondary burner (precalciner)
$F_{AIR,F(KN)}$	Air infiltration at kiln[3]		
$F_{AIR,F(PC)}$	Air infiltration at precalciner[3]		
$F_{AIR,F(PH)}$	Air infiltration at preheater[3]		

[1](Alsop, Hung et al. 2007); [2] Calculated; [3] (Kiln_Performance_Tests_Task_Force 1992)

2.1.1.1. Calculation of solid streams through the system

The size of raw material solid streams through the system required to produce 1 kgck (limestone, sand, iron ore) were calculated using the Bogue equation (see: Background) with a target alite and belite composition of 70 % and 20 % respectively, and key parameters set accordingly (S / R = 2.5; A / F = 3). The change in the composition of the solids stream between precalciner and kiln was determined assuming a calcination efficiency of 95 % at the precalciner.

2.1.1.2. Calculation of heat demands

The energy demand at the kiln ($\Delta H_{in,kiln}$, Eq. 2-8) is composed of 5 terms; the energy required to raise the temperature of the calcined raw meal stream (F_{RM}) from calciner temperature (1223 K) to sintering temperature (2073 K) (see below for calculations of the size of raw meal flows); the energy required to raise the temperature of incoming air streams from ambient (298 K) to kiln temperature (primary air; false air) (see below for calculation of raw meal flow); the energy required to raise the temperature of the secondary air from the temperature at which it leaves the cooler (assuming heat losses of 30 % (Alsop, Hung et al. 2007)); the energy required to raise the temperature of the fuel from ambient (298 K) to sintering temperature; energy losses at the kiln (radiation and convection, $H_{conv+rad}$ from (Alsop, Hung et al. 2007)); and, the exothermic clinkering reaction (-355 kJ / kg):

$$\begin{aligned} \Delta H_{in(kiln)} = {} & \Big(F_{RM} C_{p(RM)} (\Delta T_{RM})\Big) + \Big(F_{PA1} + F_{SA1}) C_{pAIR} (T_{ST} - T_{AMB})\Big) \\ & + \Big(F_{fuel1} C_{pfuel} (T_{FT} - T_{AMB})\Big) + H_{conv+rad(kn)} + \Delta H_{ck} \end{aligned} \qquad \text{Eq. 2-8}$$

As such, the calculation for Eq. 2-8 required an iterative calculation given that the fuel and air requirements are dependent on each other. Based on this calculation the kiln energy demands were estimated to be 1.38 MJ / kgck.

Next, the calciner energy demands ($\Delta H_{in,calc}$) were estimated using Eq. 2-9 comprised of eight terms; the energy required to raise the temperature of the incoming uncalcined raw meal; the energy required to raise the temperature of the incoming O_2-depleted air; the energy required to raise the temperature of the CO_2 coming in from the kiln; the energy required to raise the temperature of the tertiary air for combustion; the energy required to raise the temperature of the false air; the energy required to raise the temperature of the fuel from ambient to calciner temperature; energy losses (radiation and convection) and the energy required to drive the endothermic calcination reaction:

$$\begin{aligned}\Delta H_{in(calc)} = {} & \left(F_{RM1} \cdot C_{p(RM)} \cdot (T_{PC} - T_{RM1})\right) + \left(F_{FGKN(N2)} \cdot C_{p(N2)} \cdot (T_{PC} - T_{KNFG})\right) \\ & + \left(F_{FGKN(CO2)} \cdot C_{p(CO2)} \cdot (T_{PC} - T_{KNFG})\right) + \left(F_{TA} \cdot C_{pAIR} \cdot (T_{PC} - T_{TA})\right) \\ & + \left(F_{FAPC} \cdot C_{pAIR} \cdot (T_{PC} - T_{AMB})\right) + \left(F_{fuel2} \cdot C_{pfuel} \cdot (T_{PC} - T_{AMB})\right) \\ & + H_{conv+rad} + \Delta H_{carb}\end{aligned} \qquad \text{Eq. 2-9}$$

Eq. 2-9 also required an iterative calculation and gave a result for the calciner heat demands of 2.96 MJ / kgck. Based on these calculations the thermal efficiency of producing 1 kg of clinker (η_{ck}) was estimated to be 4.34 MJ, with almost 70 % of the total heat demand at the calciner. Notably, this is a higher total value than that of the most efficient processes, residing in the top 90 % percentile of kilns globally (WBCSD 2006). Comparison of key values in the mass balance against those of a reference cement plant (Kiln_Performance_Tests_Task_Force 1992) indicate that this high final value is mainly due to the size of the tertiary air stream entering at the calciner which is nearly double that of the reference case (marked with an asterisk in Table 2-6):

The fact that the calciner heat demands comprise 70 % of the total energy demands (as opposed to the usual 60 %) suggests it is this value which causes the thermal efficiency to be lower than that of the most efficient cement plants with a thermal efficiency of nearer to 3 MJ / kgck.

Table 2-6. Comparison of key values in the mass balance against those of a reference case.

Notation	Description	Calculated (kg / kgck)	Reference (kg / kgck)
$F_{AIR,C}$	*Air to cooler*	2.81	2.72
$F_{AIR,S}$	*Secondary Air*	0.35	0.52
$F_{AIR,T}$	*Tertiary Air **	0.96	0.48
$\text{Fuel}_{\mathbf{MB}}$	*Fuel (main burner)*	0.05	0.09
$\text{Fuel}_{\mathbf{SB}}$	*Fuel (secondary burner)*	0.09	0.09

2.1.1.3. Calculation for kiln hood air infiltration ('false' air)

The volume flow of infiltrated air at the kiln hood ($V_{,FA,KN}$) can be estimated using a modified Bernoulli equation which includes a correction factor for the assumptions of frictionless flow, Eq. 2-10(Kiln_Performance_Tests_Task_Force 1992), where: F = cross-sectional area of opening (m^2), $\rho_{,L,N}$=air density in cross-section F (kg / m^3) Δp = pressure differential (Pa):

$$\dot{V}_{FA,kn} = \frac{0.75 \cdot F}{\rho_{L,N}} \sqrt{\Delta p \cdot \rho_{L,N} \cdot 2} \qquad \text{Eq. 2-10}$$

However some of these values are unknown (e.g. the cross-sectional area of openings at each of the respective pyro-processing stages) and so the values for false air have been taken directly from the reference case (Table 2-7).

Table 2-7. Values of false air used in the model (kg / kgck) (Kiln_Performance_Tests_Task_Force 1992).

Preheater (combined)	0.08
Precalciner	0.22
Kiln	0.04

2.4. Integration of Cement Plant and Calcium Looping Plant Flow-sheets

The aim of this section was to begin to investigate the best configuration for the integration of a cement plant with Ca looping. For all configurations the following changes to the cement plant / Ca-Loop flow-sheets apply. The precalciner unit at the cement plant is replaced with a dual-CFB calciner and carbonator setup. Given that the calciner must be oxy-fired, the enthalpy associated with the hot tertiary air previously supplied to the precalciner is available elsewhere (e.g. for preheating of raw materials, fluidising of carbonator solids or for driving a steam cycle). There is also no longer false air associated with the calciner. In all configurations the kiln flue gas is passed to the carbonator rather than the calciner to enable capture of CO_2 arising from fuel use at the kiln and to fluidise carbonator solids. Limestone is added to the dual-CFB either via the carbonator or calciner, separate from the raw meal which is added to the system either via the preheater or directly to the kiln. (NB. In this model it is assumed that fresh limestone is added to the calciner according to Eq. 2-6). Lastly, CaO sorbent purged from the calciner is passed to the kiln separate from raw meal stream. This last point however requires some clarification; current Ca-looping pilot-scale demonstrations have used sorbent particle sizes larger than the 90 μ required for formation of calcium silicates (Rodríguez, Alonso et al. 2011); CanMET, 400 – 800 μ; INCAR, 130 – 180 μ; IFK, 350 μ. However particle sizes as low as 50 μ are permissible in CFBCs (Sun, Grace et al. 2008). It is therefore worth pointing out that a grinding stage between the CFB calciner and kiln may be required which would cause complications in terms of the energy supplied to the kiln via the hot raw meal stream. For the purposes of this investigation it will be assumed that the size of CaO sorbent particles purged from the calciner to the kiln match that of the 90 μ required for formation of calcium silicates in the kiln. It is important to note that though the energy demand of the base-case scenario (i.e. a basic cement plant) is somewhat higher than that of the most modern and efficient kilns, it is the relative differences in energy demand between different potential configurations with Ca-looping that are most important, not the absolute values.

For all configurations the cement plant mass balance was scaled up from 1 kgck to 46.29 kgck / second; this is equivalent to a 4000 tonne clinker / day cement plant. This is to ensure that the correct amount of CO_2 was entering the carbonator from the kiln (0.13 kg / kgck equating to 0.14 kmols^{-1}). The CaO sorbent purge size was fixed at the rate of CaO required to supply the amount of CaO needed for a cement plant of this size (0.45 kg / kgck or 0.55 kmols^{-1}) giving a F_0 / F_{CO2} value of ~ 4. Different values of F_R / F_{CO2} and W_{CaO} were tested to achieve a minimum heat demand at the calciner whilst capturing the maximum amount of CO_2 (~ 0.12 kg CO_2 / kgck or 126 mols^{-1}) assuming an E_{CO2} value of 92 %. The calciner heat demands under this configuration for different bed inventories (W_{CaO}) and recycle rates (F_R) are given in Table 2-8.

Table 2-8. Combinations of W_{CaO} / F_R which give a E_{CO2} value of 92 % and the associated values of H_{in}.

W_{CaO}	F_R / F_{CO2}	H_{in} / s(MJ)
200	1	166.05
10	2	167.43
2.45	3	167.43
1.75	4	167.65
1.5	5	169.45

Values for H_{in} under this configuration range from 166.05 – 169.45 MW as a function of W_{CaO} and F_R. Next, for the three configurations described below it was first necessary to calculate the enthalpy of the waste gas streams as given in Table 2-9.

Table 2-9. Enthalpy of waste gas streams.

Stream	Enthalpy (MJ/s)
Tertiary air	44.98
Vent air	70.29
High conc. CO_2 stream	12.10
Carbonator off-gas (N_2 + CO_2)	17.16

2.4.1. Configuration 1

In the first configuration, all waste heat streams (the high concentration CO_2 stream, F_{CO2}; the CO_2-depleted carbonator flue gas, F_{FGCB}; waste cooler air, $F_{TA}+F_{VA}$) are used to drive a steam cycle. In this configuration, the cooler vent air normally released to atmosphere (constituting an unused waste heat stream) can also be used; this is not the case in a standard cement plant as the vent air on its own would not provide the energy needed to drive a steam cycle. In this configuration, raw meal is passed directly to the kiln without any preheating.

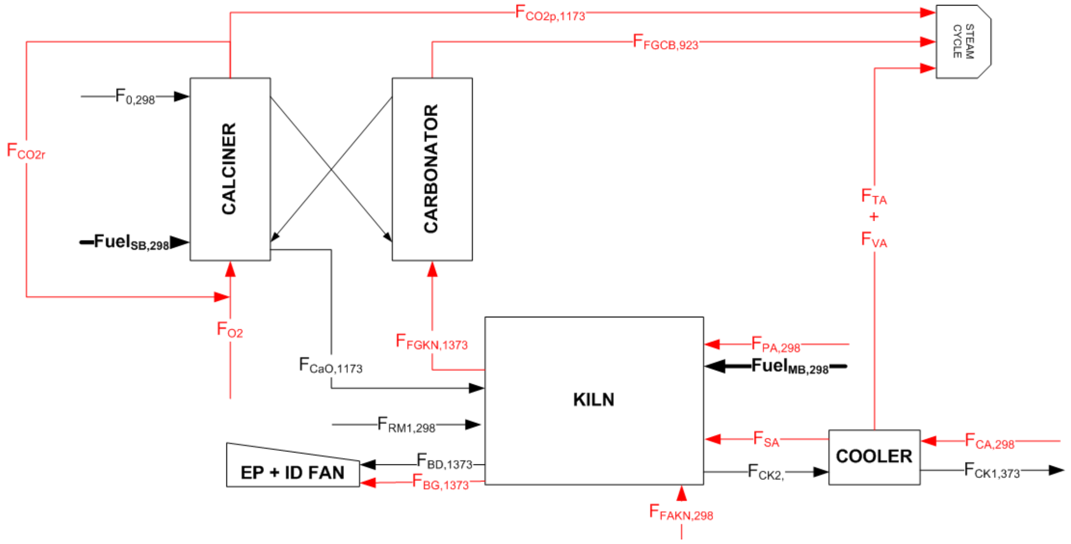

Figure 2-13. Integration of cement manufacture and Ca-looping: Configuration 1.

It was found that introducing the raw meal to the kiln from ambient increased the energy demands at the kiln by 0.86 MJ / kg from 1.38 to 2.24. This equates to a kiln energy demand of 103.69 MJ / s for a 4000 tonne / day cement plant. Therefore the system as a whole including the precalciner (operating with the optimum values indicated in Table 2-8 operates at 269.74 MW, with ~ 2 / 3 of the total energy demands being consumed at the calciner.

However this configuration makes available four streams for the powering of a steam cycle. Assuming a waste heat boiler efficiency of 22 % (Babcock and Wilcox 1978), the enthalpy of these streams (Table 2-9) could supply 56 MW of electricity. This is an excess above the ~ 20 MW (Alsop, Hung et al. 2007) required for a cement plant. Therefore ~ 36 MW of electricity could be supplied back to the grid or used elsewhere for other nearby industrial processes.

2.4.2. Configuration 2

In this configuration, all waste heat streams are used to preheat the raw meal (Figure 2-14).

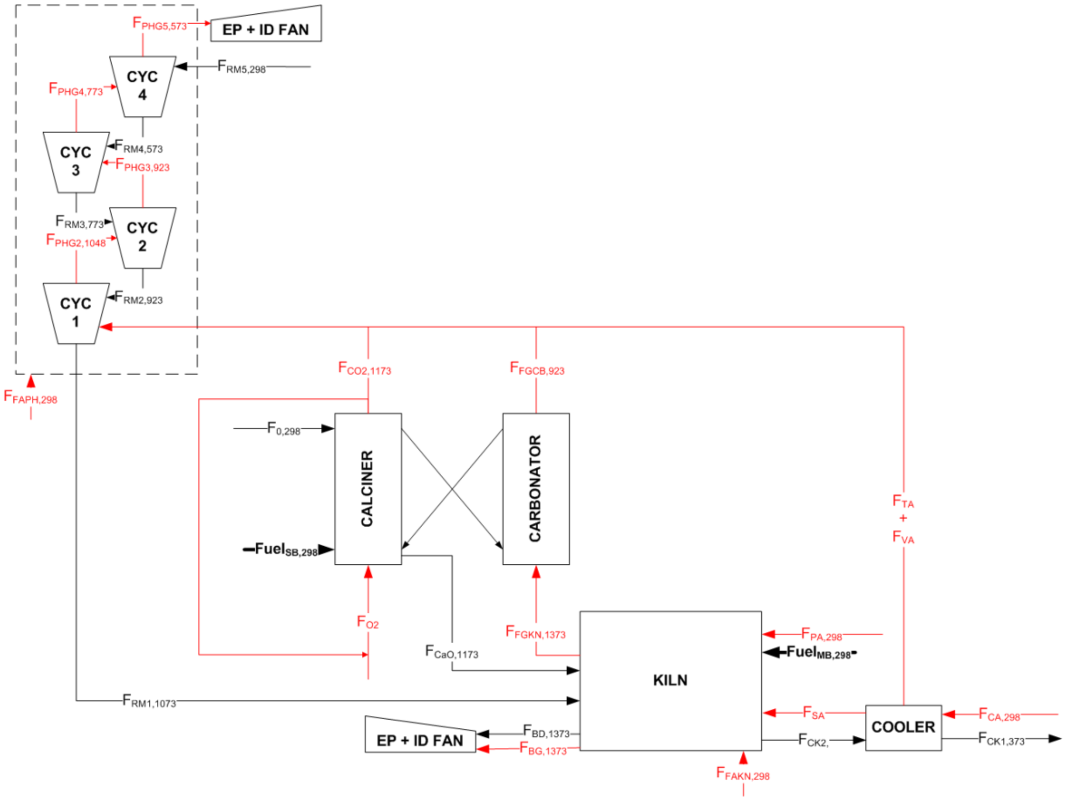

Figure 2-14. Integration of cement manufacture and Ca-looping: Configuration 2.

It was not possible to calculate the temperature of the solids and gases passing through four preheaters due to there being too many unknown values (NB. Previously these values had been taken from literature (Ahn, Ozcan et al. 2011)). Instead, by using Eq. 2-11 the heat transfer was modelled as a single unit making it possible to calculate the temperature of the raw meal coming into the kiln, where Q_o = the enthalpy of the outgoing hot gas streams, $C_{p(RM)}$ = the specific heat capacity of the raw meal (kJ / kg / K), m_{RM} = the mass of the raw meal entering the kiln (kg) and ΔT = the change in temperature of the raw meal from ambient (K). Assuming a heat transfer efficiency of 70 % (Alsop, Hung et al.

2007) the final temperature of the raw meal before entering the kiln was calculated to be 1063 K, 513 K higher than the original temperature of 550 K.

$$Q_0 = \dot{m}_{RM} \cdot C_{p(RM)} \cdot \Delta T \qquad \text{Eq. 2-11}$$

This brought the kiln energy demand down from 1.38 by to 0.9 MJ / kgck or 41.66 MW. This equated to a total energy demand of 207.71 MW with ~ 80 % of the energy demands at the Ca-loop calciner.

2.4.3. Configuration 3

In configuration 3 the aim is to produce enough electricity to power the cement plant with other streams being used to preheat the raw meal to bring down the kiln energy demand as much as possible. Again, assuming a waste heat boiler efficiency of 22 %, this would suggest that the enthalpy required to drive a steam cycle to produce the 20 MW of electricity required at the cement plant would be at ~ 80 MJ / s. This would suggest the vent air (70.29 MJ / s) plus the carbonator off-gas (17.16 MJ / s) would be the best candidates with a combined enthalpy of 87.45 MJ / s. As such these two streams would provide 19.29 MW of electricity. (NB. Although this efficiency is low it would not be realistic to add in a highly efficient cycle as it would only be one turbine).

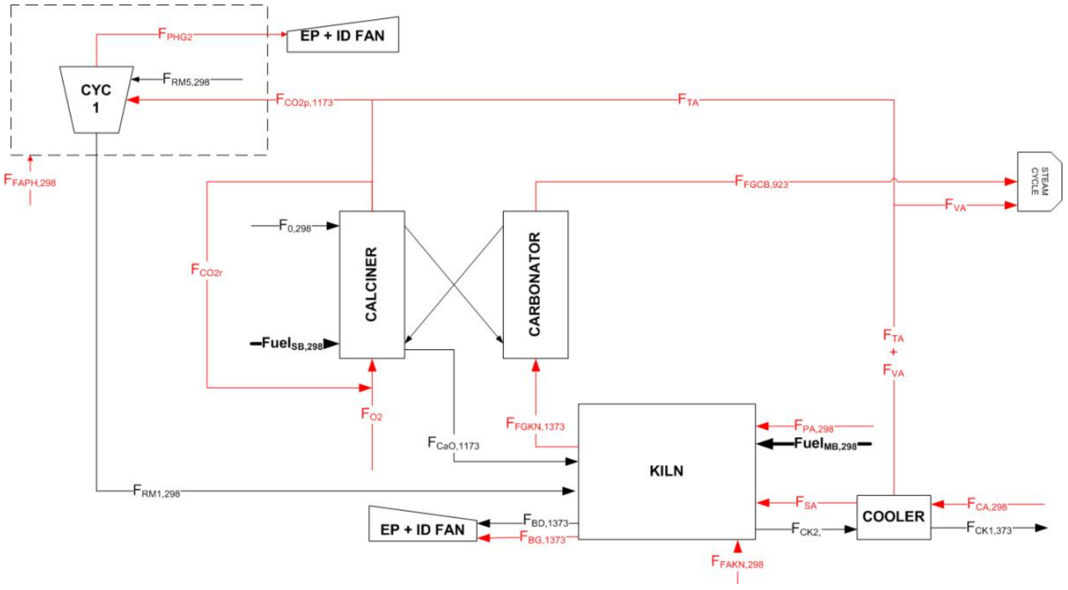

Figure 2-15. Integration of cement manufacture and Ca-looping: Configuration 3.

This leaves the remaining tertiary air and calciner off-gas (high purity CO_2) to preheat the raw meal. In this configuration the raw meal is preheated to 957.47 K, whilst bringing the kiln energy demand down from 1.38 MJ / kg to 1.03 MJ / kg. (NB. It was not possible to calculate the temperature of all streams through the preheater section due to there being too many unknowns; as such the preheater was modelled as a single cyclone, as depicted in (Figure 2-15).

2.4.4. Summary of Cement Plant and Ca-looping Integration

A summary of the results of the integration of the two processes is given in Table 2-10 below:

Table 2-10. Summary of cement plant and Ca-looping integration results.

Config.	Kiln energy demands (MJ / kg ck)	Kiln energy demands MW	Total energy demands **MJ / kg ck (η_{ck})**	Total energy demands MW	Elec. demand from the grid (MW)	Notes
1	1.38→2.24	103.69	**4.34→5.83**	269.74	~ – 36	Provides most amount of excess electricity and removes need for the preheater section.
2	1.38→0.9	41.66	**4.34→4.49**	207.71	~ 20	Reduces the kiln energy demand by the largest amount but provides no electricity for the plant.
3	1.38→1.03	47.68	**4.34→4.62**	213.73	~ 0	Preheats the raw meal to ~ 1000 K bringing the kiln energy demand down by 0.35 MJ / kg and supplies enough electricity for the plant.

All three configurations capture 92 % of the CO_2 arising from the burning of fuel at the kiln which equates to ~ 0.12 kg CO_2 / kgck (or 126 mols^{-1}) whilst 0.01 kg CO_2 / kgck (or 11 mols^{-1}) are lost to atmosphere.

2.5. Conclusions

- The Ca-Looping system has been modelled using a stochastic population balance model, a method which is able to garner similar results for the age distribution (r_N), the maximum average reactivity of the sorbent ($\bar{x}_c$) and the CO_2 capture efficiency of the carbonator (E_{CO2}) as those published in literature by INCAR.

- This method has been furthered to run on a time basis as opposed to per cycle and to incorporate the carbonation rate and extent of carbonation from experimental data rather than a simplified kinetic model.

- A generic dry-process cement plant mass and energy balance has been developed which resulted in a figure of 4.34 MJ for the thermal efficiency of producing 1 kg of clinker. This is within the top 90th percentile of kilns globally; it is thought that this lower thermal efficiency is due to the size of the tertiary air stream.

- Integration of the Ca-looping process with the cement plant indicates that the thermal efficiency of producing 1 kg of clinker can range from 4.49 – 5.83 MJ depending on whether the system supplies itself with electricity through waste heat recovery or whether electricity is supplied from the grid. Up to ~ 36 MW electricity may also be passed back to the grid, however this results in the lowest thermal efficiency of producing 1 kg of clinker of 5.83 MJ. For all configurations 92 % of all CO_2 produced at the kiln is captured which equates to ~ 0.12 kg / kg of clinker or 126 $mols^{-1}$.

2.6. Further Work

- Incorporation of the effects of sulphation and ash into the model.

- Incorporation of a hydrator into the model.

- Costing of the process (Capex / Opex).

Chapter 3. Production of spent sorbent

3.1. Chapter Summary

Sorbent purged from the Ca-loop is likely to differ in chemical composition to that of CaO passed directly to a cement kiln due to an increase in exposure to a combustion environment over a given number of calcination / carbonation cycles. Spent sorbent has been produced in the laboratory using a purpose-built vertical tube furnace incorporating a range of fuel feeders.

3.2. Vertical Tube Furnace Design and Operation

3.2.1. Basic Furnace Design for 'No Fuel' Experiments

The core components of the furnace consist of a 508mm ID Incoloy 800HT pipe, heated electrically by a high-output transformer (1600 A, 2.5 V) via copper electrodes (dimensions 300 x 50 x 5 mm) clamped at the top and bottom of the heating zone, and two sets of ten copper cables (75mm^2 cross-section, 800mm length) (see Figure 3-1). The electrodes are positioned to ensure that the centre of the bed of limestone (70 mm in height when fluidised) sits at the hottest part of the reaction vessel (see arrows on Figure 3-1). The power to the electrodes is controlled by a hardware-based power control unit, operated in turn by a purpose-written program, written in Agilent VEE™ Pro 7.0 software. The temperature of both the bed and the outer reactor wall are measured at points along the bed and wall using type 'K' thermocouples and is monitored / controlled by this program via PID control. The tube and the electrodes are insulated with three layers of Superwool® 607 Max blanket to minimise heat losses from the system. The heat shrink used on the copper cables and the rubber sheath closest to the electrodes are water-cooled by a series of soft copper tubing coils (1 / 8" o.d.), tightly bound around the cable for approximately 50mm along the length of the cable. The quartz reaction vessel sits inside the Incoloy tube as a sliding fit, supported from underneath by various means depending on the configuration. The dimensions of the reactor were chosen to allow 100 g limestone to be calcined in a single run to enable the maximum amount of clinker to be produced as limited by the size of the higher temperature horizontal furnace (see Chapter 5, section 5.3.1). Threads were also made at the top and bottom of the Incoloy pipe to enable the furnace to be used as a closed system if required.

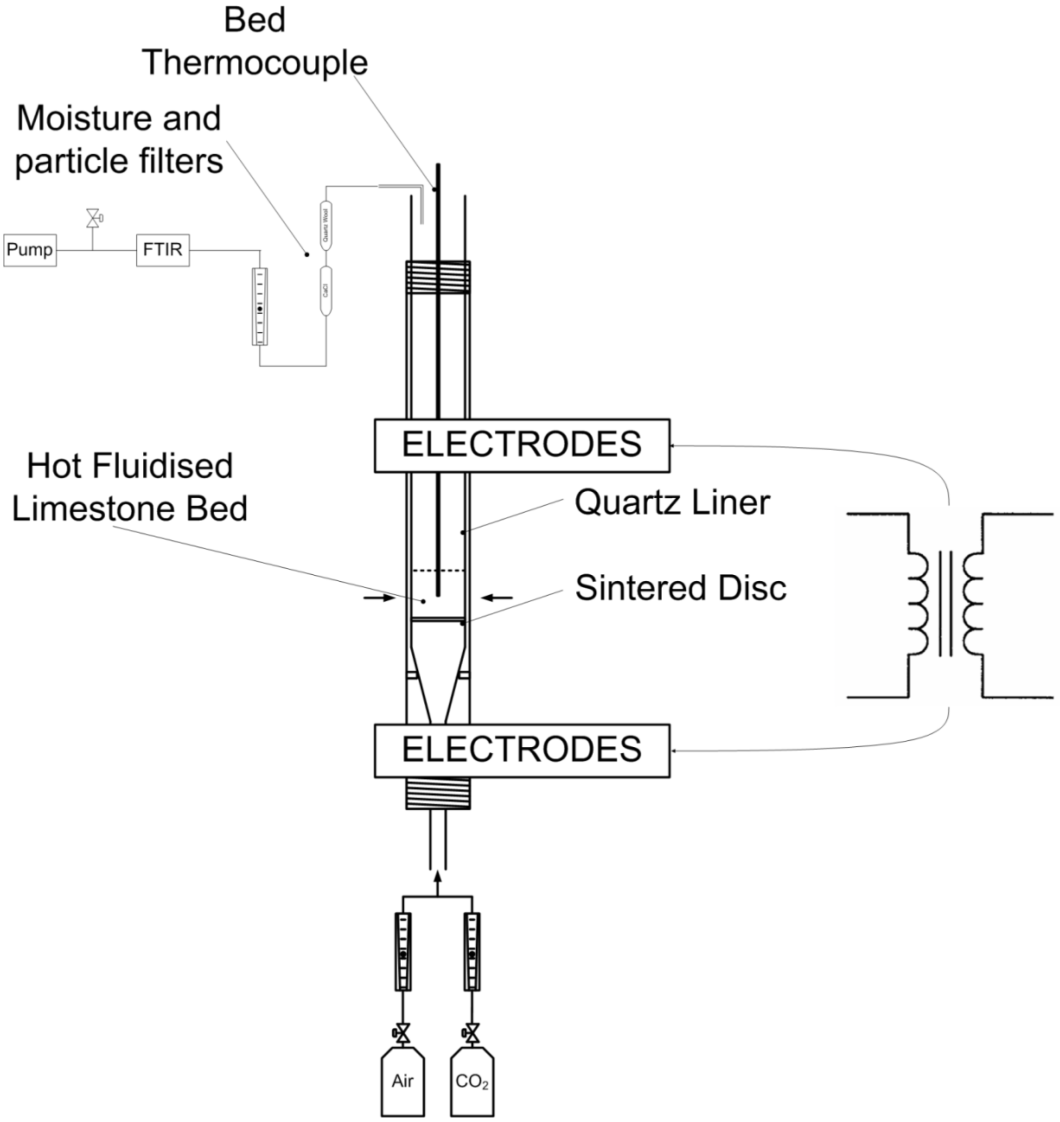

Figure 3-1. Core components of the vertical tube furnace (fluidised bed design).

Gases are supplied to the base of the bed by cylinders via calibrated rotameters. The off-gas is drawn through a Perkin-Elmer FTIR-100 spectrometer via an air pump pumping at a flow-rate at 12 l / m. Given that the required flow-rate to the spectrometer is only 1 l /m, a bleed valve is positioned between the spectrometer and pump to enable the flow-rate to be finely controlled, as measured by a calibrated rotameter. Gases are drawn through quartz wool and CaCl filters to minimise reactor fines and moisture passing to the spectrometer gas cell. Initially, a piece of ¼" pipe bent to a right angle was positioned at the top of the reactor serving as the feed to the off-gas line towards the gas analysis apparatus. However, this was later replaced with a quartz piece to enable the reactor fines to be collected without concern over contamination from metal components.

3.2.2. Calibration of FTIR for CO_2

The CO_2 concentration at the off-gas is measured using a Perkin Elmer Spectrum 100 spectrometer and is controlled by Perkin Elmer Timebase software. To calibrate for CO_2 concentrations of CO_2 ranging from 5 – 50 % are fed into the rig using N_2 as the balance and the corresponding absorbance recorded. The wavelength range used for measuring CO_2 was 3619 ± 50 cm^{-1}. (The larger peak at 2350 cm^{-1} cannot be used; though offering greater sensitivity, clipping occurs at the top of the peak rendering this peak unusable (Figure 3-2)).

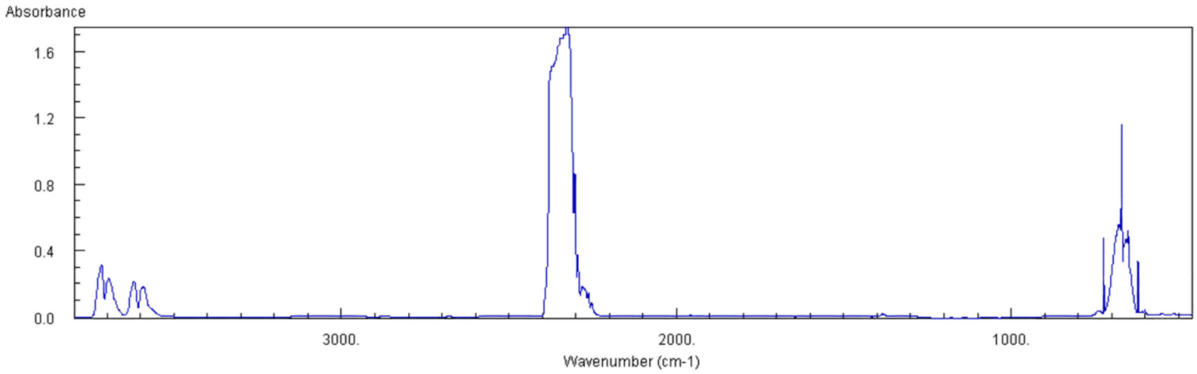

Figure 3-2. CO_2 Infra-red (IR) Spectrum (NIST 2011).

Absorbance vs. concentrations is plotted and a fit of the line used to convert absorbance to concentration during the cycling experiments (Figure 3-3).

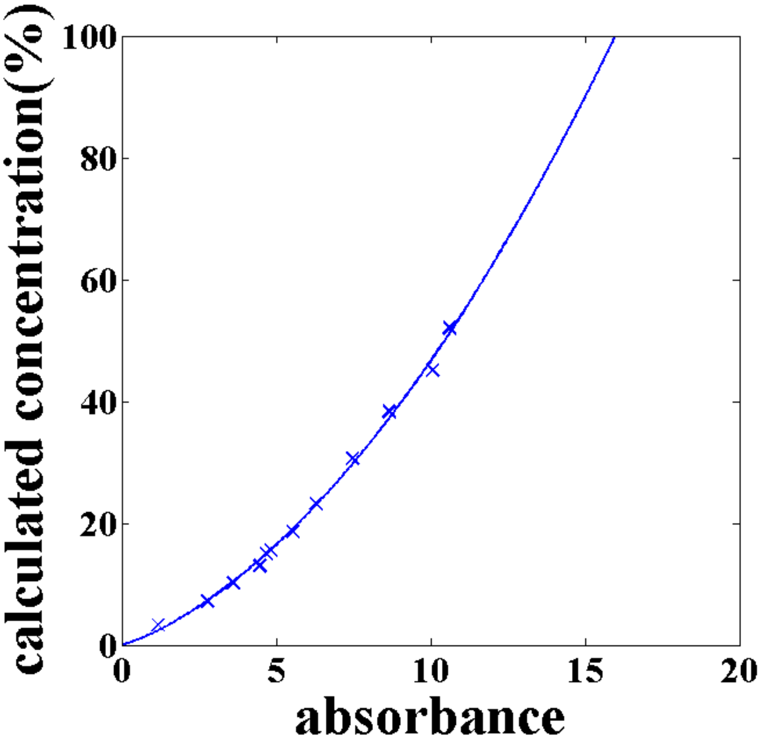

Figure 3-3. Calibration Curve for CO_2.

A purpose-written program in Matlab is used to convert absorbance to concentration in the cycling experiments (for the code please see Appendix 3-1). The FTIR is also calibrated for carbon monoxide (CO) at the 2025 cm^{-1} peak to enable some understanding of the combustion characteristics of the system (i.e. incomplete combustion).

3.2.3. Modification of rig design for coal experiments

Initially, coal experiments were performed using a spouted-bed design to allow coal to be fed into the bed batch-wise from underneath via a compressed air "bullet" feeder whereby coal granules are injected into the base of the bed by opening and closing two valves (Figure 3-4).

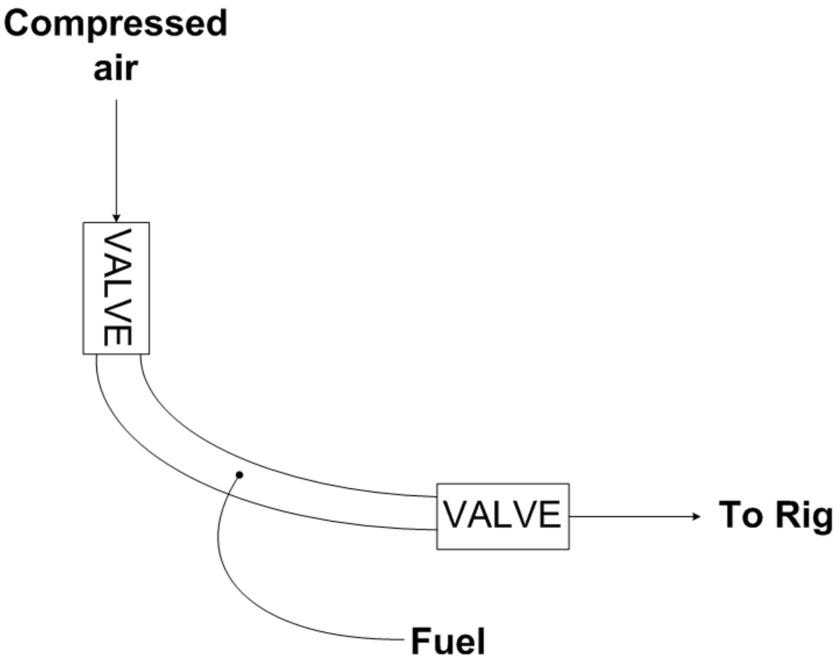

Figure 3-4. Schematic of batch ‘bullet’ coal feeder.

This was later replaced with a “rotary hopper” feeder to enable continuous feeding of coal over a given number of minutes. This feeder consists of a quartz hopper made from a modified titration tube. A plastic rotary cup feeder sits at the base of the hopper, rotated by a motor. Coal granules fall into a quartz feed line, swept in by air at a flow-rate of 1 l / m. This flow-rate is used as a compromise between that needed to sweep the granules into the bed against the incoming fluidising gas, whilst minimising the effect of the sweep gas impacting on the heat requirements of the system. The fuel feed line is encased inside a second quartz tube to allow cooling water to be passed along the length of the feed line. The vertical position of the fuel feed line is again set as a compromise such that the granules drop deep inside and not on top of the bed, whilst minimising the effect of the cooling water (3 l / m) on the heat requirements of the system. This design enabled coal granules to be fed continuously without concerns regarding contamination from metal components (Figure 3-5).

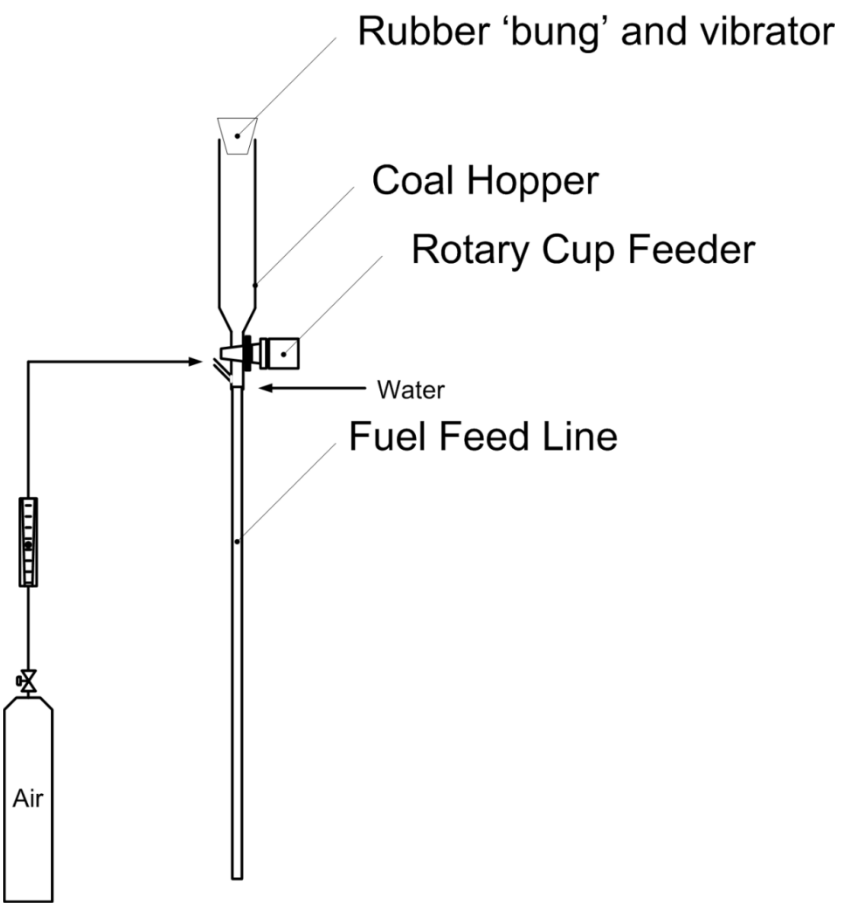

Figure 3-5. Schematic of continuous coal feeder.

Given that the incoming fluidising gas mainly enters through the central part of the bed (from an ariel view) the fuel feed line is positioned off-centre to ensure that the fluidising gas does not prevent the sweep-gas from entraining the granules into the bed. The fuel hopper is attached to the feed line using electrical heat-shrink insulation material. During the cycling experiment, fuel is fed from the point at which calcination is detected based on the initial rise in CO_2 concentration. Coal is fed at a rate of 0.5 g / minute over a period of 16 minutes (8 g of coal in total for each cycle) based on flowsheeting work which predicted the ratio of ash to limestone in each packet of the stochastic model where ash was converted to fuel based on the ash content of the fuel being used (for an explanation of 'packets'see: Chapter 2, section 2.2.1).

3.2.4. Modifications for Refuse-derived Fuel (RDF): feeder design

The feeding of RDF at the laboratory-scale is problematic due to its heterogeneity and the size of the pieces, ~ 25mm in diameter. It is possible to produce a more homogeneous sample by grinding, however this produces a fluffy / dusty sample which cannot be fed by either of the two feeders previously described. By pressing the homogenised sample into a pellet, it is possible to produce a solid sample. A novel feeding apparatus was developed as part of this PhD (Figure 3-6) which enabled the solid sample to be fed from underneath by operating the system as a spouted bed.

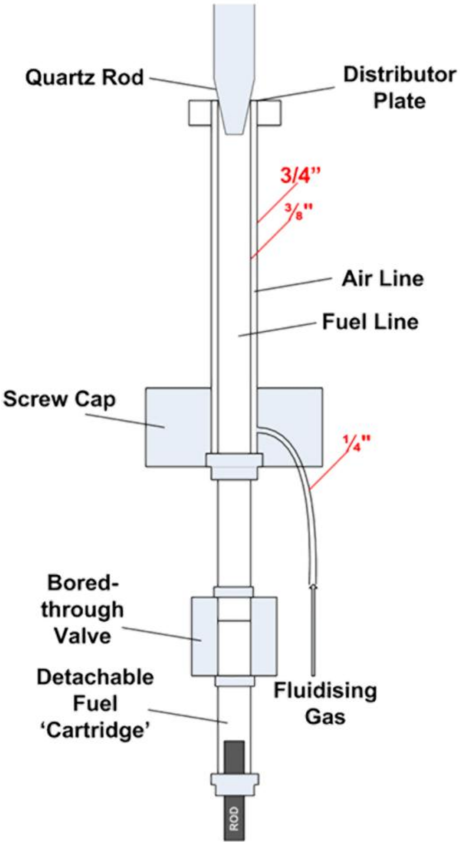

Figure 3-6. Schematic of semi-continuous RDF feeder.

The spout consists of a 3/8” OD tube contained within a ¾” OD tube. The outside tube has a 1/4” tube welded at the base; the fluidising gas passes through this tube and through the gap between the 3/8” and 3/8” tube and into the base of the quartz liner. This way, the incoming gas serves two vital functions. Firstly, it allows the fluidising gas to reach the bed whilst leaving the 3/8” tube free for the pellet to be inserted without the issue of the fuel blocking the incoming gas. Secondly, by having the fluidising gas travel up the outside of the fuel feeding tube, the gas serves as cooling air, hindering any potential for combustion / pyrolysis of the fuel before reaching the bed. A 1/8” water-cooling coil is also included in the design between the spout and the inside of the reactor tube. A distributor plate at the top of the spout secures the fuel and gas lines, whilst preventing limestone particles from falling through the gas line. A quartz rod with a bevelled end, secured by the screw cap at the top of the reactor in the centre of the bed, is positioned such that it sits snugly inside the fuel line, preventing particles from falling through the fuel line.

As the fuel is pushed into the bed from underneath, the quartz rod lifts just enough to allow the fuel to enter the bed at the desired rate, to be replaced by pushing down on the rod from above once all the fuel has been administered. The valve at the base of the spout is bored through, allowing the fuel “cartridges” (which require replacement on each cycle) to be changed whilst keeping the fuel feed line flush along the inside to prevent blockages. Lastly, the RDF is pressed into pellets 6mm wide (2mm narrower than the fuel feed tube ID) and 60mm long using a mould and press. The fuel can be administered in a semi-continuous mode by using a lab jack to raise the rod and pellet manually.

It was found however that pellets needed to be used on the same day that they were made; leaving them overnight led to deformation such that they wouldn’t fit into the feeder. As such, a limitation was placed on how much fuel could be fed in a cycling experiment based on how many pellets could be produced in a morning enabling the cycling experiment to be carried out in the afternoon.

3.3. Design of Experiments

3.3.1. Determination of minimum fluidising velocity

The size of limestone particles used in these experiments was 500 – 710 μm, chosen such that the mean diameter of bed particles was within the range of that used in commercial fluidized-bed combustors (0.5 – 1 mm) (Lanauze 1985). It was necessary to choose a flow rate which fluidised this size of particle without introducing unnecessary heat demands to the system. The minimum fluidising velocity was determined both through the use of an equation from the literature and empirically. To determine this value through theory, first the Reynolds Number at minimum fluidising conditions (Re_{mf}) was calculated using Eq. 3-1 proposed by Wen and Yu (Wen and Yu 1966).

$$Re_{mf} = [33.7^2 + 0.0408 \cdot Ar]^{0.5} - 33.7 \qquad \text{Eq. 3-1}$$

where:

$$Ar = \frac{{d_p}^3 \cdot \rho_f \cdot (\rho_s - \rho_f) \cdot g}{\mu^2} \qquad \text{Eq. 3-2}$$

Where: d_p is the particle diameter, ρ_f is the fluid (gas) density, ρ_s is the particle density, g is the gravitational constant and μ is the fluid viscosity.

The superficial velocity at minimum fluidising conditions (U_{mf}) can then be calculated from Eq. 3-3:

$$U_{mf} = \frac{\mu \cdot Re_{mf}}{d_p \cdot \rho_f} \qquad \text{Eq. 3-3}$$

Fluid viscosities for N_2 were taken from Nist Webbook (NIST 2011) with a density of limestone of 2600 kg / m^3. Eq. 3-3 indicated a U_{mf} value of 0.02 m / s which, given the cross-sectional area of the reactor (0.0028 m2), could be provided with a flow-rate of 3.46 l / m.

Next, U_{mf} was determined experimentally by gradually increasing the flow rate to the bed at 1 l / m intervals and observing the point at which the bed started to fluidise. This method indicated that at 2 l / m the bed started to rise and particles started to circulate. This equated to a U_{mf} value of 0.012 m / s for the size of reactor, nearly half that of the value calculated via Eq. 3-3. It was decided that the value of U_{mf} used would be taken from the empirical results and that a U / U_{mf} value of ~ 2 would be used to ensure bed fluidisation whilst minimising the heat demands of the system which would increase to ~ 3 U / U_{mf} at the higher calcination temperatures. Therefore the total flow of gas into the bed for the 'No Fuel' experiments was determined to be 4 l / m.

3.3.2. Determining coal particle size

The U / U_{mf} was kept the same as that of the 'No Fuel experiments ($U / U_{mf} = 2$) and was deemed high enough to ensure rapid mixing (< 1s) of two media of differing size and density (Fennell, Davidson et al. 2005). Assuming a coal density of 1300 kg / m^3, this would indicate a particle size of 0.71 – 0.85 mm according to the correlation by Wen and Yu detailed in the previous section to match the U / U_{mf} value of the coal with that of the limestone. Experiments which observed the mixing of the two media under cold conditions indicated that the particles mixed rapidly at these two particle sizes.

3.4. Description of Cycling experiments

3.4.1. 'No Fuel' Experiments

The quartz liner is first rinsed with deionised water and dried overnight. The supporting tube is put into position at the base of the reactor. A type K thermocouple is secured such that the tip is located at the centre of where the bed will be in both horizontal and vertical planes (35 mm from the top of the sintered disc for a bed height of 70 mm). The bed temperature set-point is set to 900 ºC. The off-gas line is secured in place at the top of the quartz liner such that the top of the line sits 50 mm into the top of the quartz liner. Both sets of software (Agilent VEE and Timebase) are started simultaneously to allow control of the system and to enable plots to be made at a later stage. A 15 % CO_2 calibration is passed into the system via a rotameter before then passing 15 % CO_2 from a 100 % CO_2 cylinder with N_2 as the balance. A 100 g batch of 500 – 710 μ Longcal P25 is dropped into the liner to form the bed which causes the bed temperature to drop to below 400 °C (see Figure 3-7). Calcination starts to take place which is inferred from the increasing CO_2 concentration in the off-gas.

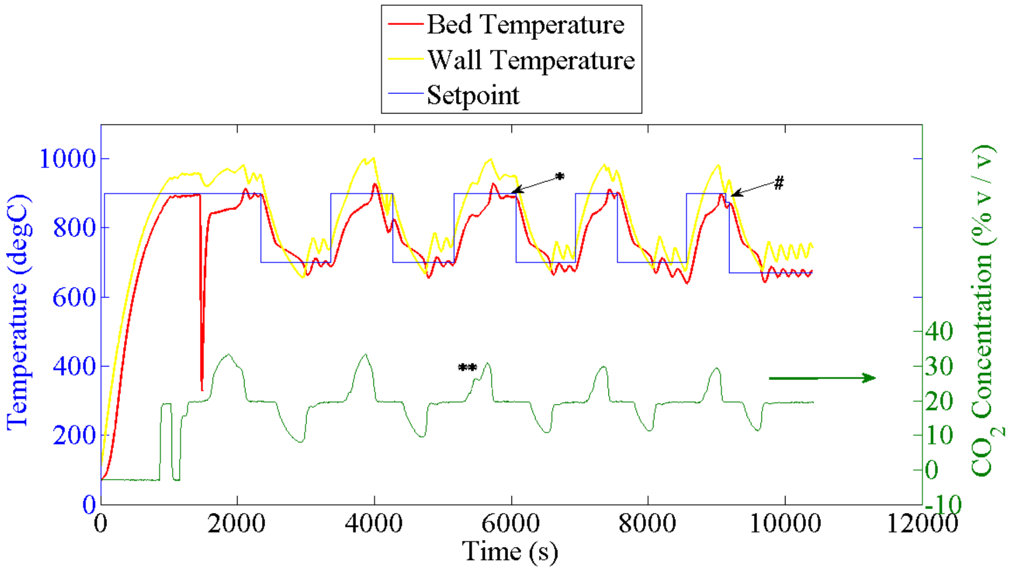

Figure 3-7. CO_2 concentration and system temperatures for 'no fuel' cycling experiments.

Notably, for the majority of calcination in the first 5 cycles, the temperature of the bed rose gradually from the temperature at which calcination started (~ 810 °C) towards 850 °C. At this point the temperature rose quickly above the set-point of 900 °C. Some degree of temperature control was required to prevent the wall temperature from going above 1000 °C (the temperature at which Incoloy becomes vulnerable to shape change) as indicated with an asterisk on cycle three of Figure 3-7. This was achieved by adjusting the voltage on the front of the power controller. On the fifth calcination this was achieved by reducing the set-point of the bed to 875 °C (marked with a hash on Figure 3-8. It can also be seen that on the third cycle by reaching the maximum wall temperature of 1000 °C that the safety alarm on the power controller was triggered causing the power to cut out leading to a temporary drop in CO_2 concentration (marked with a double asterisk on Figure 3-7). For some unknown this did not occur on the first calcination despite the wall temperature reaching 1000 °C.

End of calcination is defined as the time at which the CO_2 concentration is seen to return to the 15 % baseline. After 60 s at the baseline, the temperature set point is set to 650 ºC to affect the carbonation step. This process is repeated for a given number of cycles. After the last calcination, the CO_2 is switched off and the bed allowed to return to ambient temperature. The quartz liner is then removed and the sorbent stored for use in subsequent stages.

3.4.2. Coal Experiments

For the batch coal experiments, coal is fired into the base of the bed as described in section 3.2.3. As can be seen in Figure 3-8, firing the 2 g coal charge into the bed causes the CO_2 concentration to increase from that coming from calcination to between 30 and 35 %. This also causes the bed temperature to increase to that of the temperature set point (900 ºC), which in turn causes the temperature to drop rapidly due to a loss of power given that the set point has been reached.

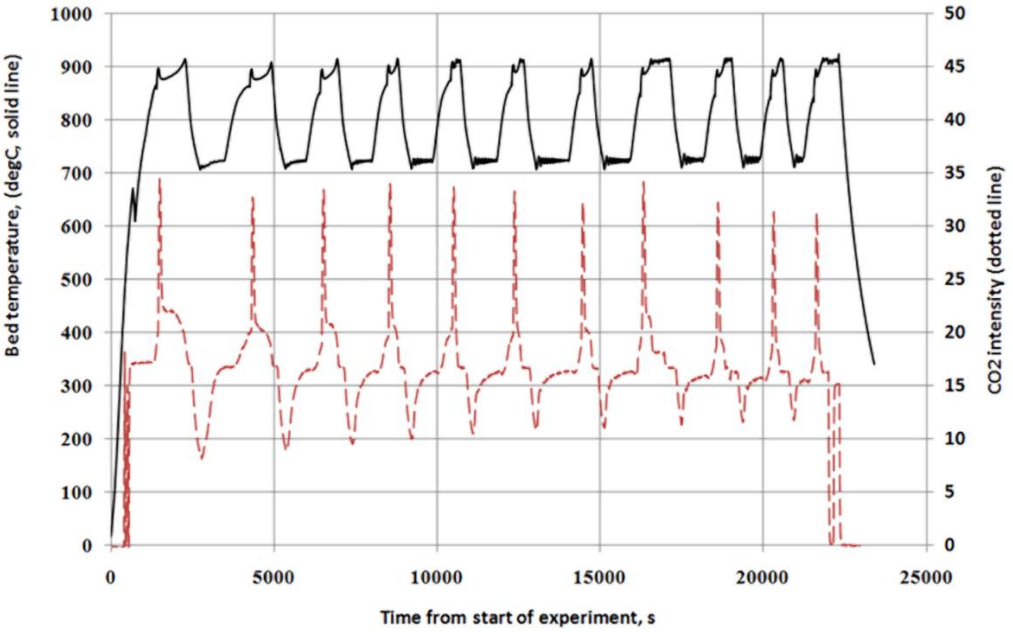

Figure 3-8. CO_2 concentration and system temperatures for cycling experiments. La Jagua coal (batch-fed).

In the case of the continuously fed coal experiment, coal is fed in gradually by switching on the motor. The sweep gas (air) and water cooling are also both switched on simultaneously. The introduction of fuel can be seen to increase the bed temperature but an increase in CO_2 concentration is not observed given that the fuel is being fed in gradually. However once calcination is complete the steady addition of the fuel is observed until coal is no longer fed. At this point the CO_2 concentration returns to the 15 % baseline. An rapid increase in CO_2 observed at the start of calcination indicates however that the fuel is being fed from the start of calcination. The low CO (CO not shown in Figure 3-8) concentration also indicates that near-complete combustion of the fuel is taking place.

3.4.3. RDF Experiments

In the RDF experiments, the feeding of fuel is only semi-continuous. The effect of adding the fuel in this way was somewhat erratic due to the heterogeneous nature of the fuel, leading to surges in bed temperature and CO_2 concentration.

3.5. Mass balance on CO_2 from a single calcination (No Fuel)

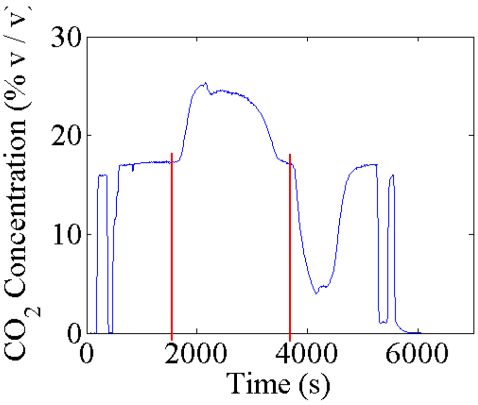

Figure 3-9. CO_2 concentration as a function of time on a single cycle. Red lines indicate where the start and end of the points included in the mass balance.

It is possible to determine whether calcination goes to completion by performing a mass balance on the CO_2 on the first calcination and comparing it to the known amount of CO_2 going in from a 100 g batch of limestone. The number of moles of CO_2 going in is given by the amount of limestone multiplied by the known purity of the limestone (in this case for Longcliffe, 98.25 %) divided by the relative atomic mass of $CaCO_3$ (100.77). Figure 3-9 shows CO_2 concentration in the off-gas on a single cycle, with an indication of the start and end of the mass balance.

The number of moles of CO_2 leaving in the off-gas is given by Eq. 3-4, where $M_{(CO2)carb}$ = number of moles of CO_2 leaving the system arising from calcination, $\dot{n}_{in}$ = the molar flow rate of gas going in (air + CO_2), X_{in} = the concentration of CO_2 in the incoming gas (15 % v / v) and X_{out}= the concentration of CO_2 in the off-gas, as recorded by the FTIR.

$$M_{(CO2)}carb = \int_0^t \left(\frac{\dot{n}_{in} \cdot (X_{in} - X_{out})}{1 - X_{out}}\right) dt \qquad \text{Eq. 3-4}$$

The result of these two calculations gave values for CO_2 going in from the limestone and CO_2 leaving the system through calcination of 0.974 and 0.956 respectively. This indicated an error of less than 2 % for the mass balance.

3.6. Conclusions

- A laboratory-scale system has been designed, built and commissioned capable of producing spent sorbent following a given number of cycles of calcination and carbonation.
- A range of fuel feeding systems have been tested and included in the commissioning process.
- The mass balance on the first cycle indicates that the limestone is fully calcined.

3.7. Further Work

- Further development of the heating system would ensure the entire calcination step takes place at 900 °C rather than between 800 and 900 °C.
- Further work would include producing sorbent with a wider range of solid fuels.

Chapter 4. Trace Element Analysis of Fuels, Limestone and Sorbent

4.1. Chapter Summary

This chapter details the methods used to enable quantification of the trace element inventory of materials entering and leaving the fluidised bed system. To ensure that the loss of elements was due to repeated cycling and not a single cycle, a comparison was made between the original limestone and the sorbent homogenised after a single cycle (‘0’ cycles). Though these results are less relevant to Ca-Looping (than those for repeated cycling), a Ca-looping calciner will have a larger quantity of fresh limestone entering than a standard cement calciner due to the need to continually replenish and purge bed material. Therefore the release of volatile elements as a result of a single calcination becomes relevant from the point of view of calciner operation (due to potential build-up of problem elements in calciner components, e.g. ring-build-ups / filters etc.).

4.2. Description of Relevant Analytical Techniques

Three analytical methods capable of performing trace element analysis are available for use at Imperial College London; two Perkin Elmer Inductively-Coupled-Plasma Atomic Emission Spectrometers (ICP-AES) and an Ion Chromatography (IC) unit in the Department of Chemical Engineering, and an Inductively-Coupled-Plasma Mass Spectrometer (ICP-MS) in the Department of Life Sciences. Other methods such as atomic absorption spectroscopy are not available and are therefore omitted from the following discussion. A more detailed discussion for ICP-AES is given as this is the technique employed for the majority of the analyses in this project (see Section 4.2.3 for the rationale for this decision).

4.2.1. ICP-AES and ICP-MS

Atomic emission spectroscopy (AES) involves excitation of a liquid sample of low acidic concentration (~ 5 %) in a high temperature inductively-coupled plasma (ICP, Figure 4-1); collisional excitation within the plasma imparts additional energy to the atoms promoting them to excited states. Both atomic and ionic excited state species then relax to the ground state via the emission of a photon producing visible light line spectra characteristic of the element present. The total number of photons is directly proportional to the concentration of the related element in the sample and recorded as counts. These counts can be converted to concentration (see section 4.3.3).

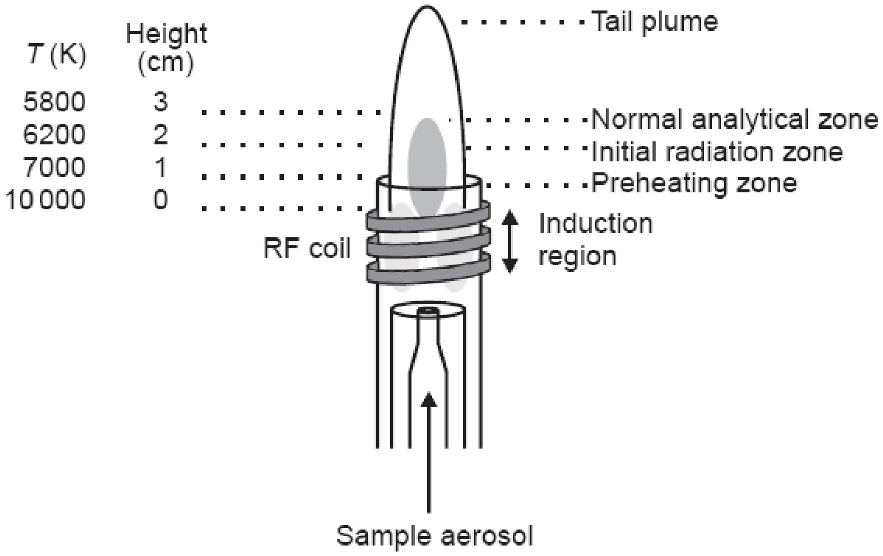

Figure 4-1. Schematic diagram of an ICP assembly showing the three concentric tubes composing the torch, the RF coil, the different plasma regions, and the temperature as a function of height above the load coil.

Concentration of elements present below 100 µg / l can be determined by comparing the intensities of the line spectra obtained against the spectra from calibration solutions of known concentrations. The method allows the determination of 20 to 60 elements either simultaneously or sequentially with detection limits typically down to 0.0001 – 0.1 parts per million (ppm). ICP-AES lacks the sensitivity to accurately determine trace element content in very dilute solutions below these concentrations, for which ICP-MS would be a more suitable choice. A further drawback with this method is the potential for interference between the different light wavelengths used to infer the concentration of a given element (see section 4.3.4 for a detailed discussion). Radial view is the classical operation mode, where the plasma is operated in a vertical orientation with the analytical zone observed from the side of the plasma. This limits the effect of potential spectral and background interferences. In axial view, the plasma is rotated to a horizontal position and the ICP is observed from the end of the plasma. The axial view can provide a 5- to 10- fold improvement in the limits of detection (LOD; see Section 4.2.4 for a definition). The list of elements capable of being observed by ICP-AES is given below (Table 4-1).

Table 4-1. List of elements that can be determined by ICP-AES (Hou 2000).

Alkaline and alkaline earth	Rare Earth	Transition metal	Others
Li, Na, K, Rb, Cs, Be, Mg, Ca, Sr, Ba	Ce, Pr, Nd, Sm, Eu, Gd, Tb, Dy, Ho, Er, Tm, Yb, Lu, Th, U	Sc, V, Ti, Cr, Mn, Fe, Co, Ni, Cu, Zn, Y, Nb, Zr, Mo, Ru, Th, Pd, Ag, Cd, La, Hf, Ta, W, Re, Os, Ir, Pt, Au, Hg	B, C, N, Al, Si, P, S, Cl, Ga, Ge, As, Se, Br, In, Sn, Sb, Te, I, Tl, Pb, Bi

In contrast ICP-MS is extremely sensitive due to the highly sensitive detection of the mass spectrometer resulting in part per trillion (ppt) detection limits (< 1 - 100 ppt), ~ 2 to 3 orders of magnitude lower than ICP-AES. As with ICP-AES, the quantification of trace elements is obtained by external calibration curves using multi-element standard aqueous solutions. As with AES, limitations of ICP-MS include interpretation of the results. The cations produced in the plasma are separated in the mass spectrometer according to their mass-over-charge (m / z) ratio. This classification has a major limitation since it is possible for two or more species to be detected at the same m/z values. For example, interferences occur when residual Cl^- anions are present in solution when HC1 or $HC1O_4$ are used during the sample preparation. In the case of As, polyatomic ion species can be formed between argon and chlorine ions resulting in interfering peak in the mass spectrum at a mass equal to their combined atomic mass, ($40^{Ar}35^{Cl}$); As will have the same m/z ratio of 75. ICP-MS is also relatively intolerant to high levels of total dissolved solids which should generally be no higher than 0.02 % in the final solution. ICP-AES is far less disturbed by the dissolved solid content of the sample. Therefore, the possibility of introducing more highly concentrated solutions in the ICP-AES instrument (generally 50 to 100 times more concentrated) often compensates for its poorer detection limits.

4.2.2. Ion-exchange Chromatography (IC)

The IC operates by the release of anions and cations from a chromatograph column based on their interaction with a resin. Solutions pass through a pressurized chromatographic column where ions are absorbed by the column, made of the resin. As an eluent runs through the column, the absorbed ions begin to separate. The retention time of different species determines their concentration in the solution and as such are characterised by their release over time. Elements that can be observed include Cl, F, K, P and S.

4.2.3. Choice of Analytical Methods

The decision over which method to use was made on the basis of an estimation of the element concentrations expected in the input materials (Table 4-2):

Table 4-2. Estimation of element concentrations in unknown samples (ppm).

	Limestone SRM 1d		Sub-bituminous coal SRM	
Element	Sample Conc.	**Solution Conc.**	Sample Conc.	**Solution Conc.**
Al	2780	**5.56**	32,000	**64**
Ba	29.6	**0.0592**	-	**-**
Cr	8.21	**0.01642**	2.5	**0.005**
Cu	-	**-**	2.6	**0.0052**
Fe	2230	**4.46**	23,900	**47.8**
K	1130	**2.26**	-	**-**
Mg	1820	**3.64**	-	**-**
Mn	209	**0.418**	21.4	**0.0428**
Na	80.9	**0.1618**	24,000	**48**
Ni	-	**-**	1.4	**0.0028**
P	180.2	**0.3604**	-	**-**
Pb	-	**-**	1.9	**0.0038**
S	1030	**2.06**	36,160	**72.32**
Sr	256	**0.512**	-	**-**
Ti	183	**0.366**	2,000	**4**
Zn	17.7	**0.0354**	4.7	**0.0094**

The expected solution concentrations were estimated by dividing the expected sample concentrations in by the dilution factor (DF) (see below, section 4.2.4) which for a 20 mg sample in 10 ml of solution is 500. This indicates that ICP-AES would serve as the most appropriate analytical technique, given the detection limits described above (section 4.2.1) (i.e. parts per million rather than parts per trillion) and the limited number of elements observable by IC. Furthermore, the high financial cost of running all samples through an ICP-MS from a different department would render the project financially unviable (~ £1000 / day as opposed to £50 / day for in-house (Jarvis 2013)). An initial comparison of the two methods actually indicate that ICP-AES actually performed better in an analysis of NIST standard reference material (SRM) 1633b (fly ash) for three elements chosen at random (Figure 4-2) where all values for the ICP-AES were within the range of the experimental limits imposed by the standard.

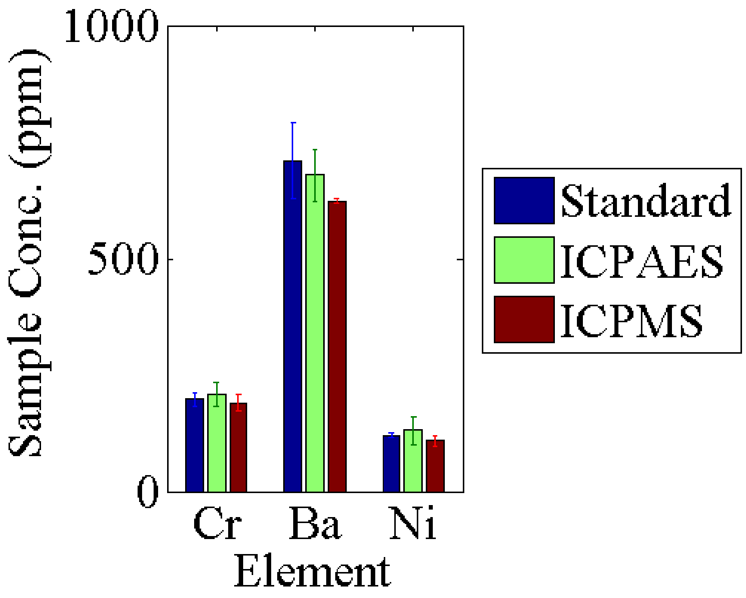

Figure 4-2. Comparison of ICPAES and ICPMS for NIST SRM 1633b (average of three repeat samples, error bars shown as relative standard deviation, RSD).

However, neither of the in-house ICP-AES machines are capable of observing S. This is because the only observable wavelength for this element is at the bottom of the light spectrum at ~ 189 nm below the minimum wavelength detectable by the machine (190 nm). According to the machine operating instructions it was possible to observe the lower range of the light spectrum through attachment of a N_2 purge line. However this was found not to be the case on either machine. Therefore attempts have been made to observe S using ion chromatography (see section 4.3.9).

4.2.4. Important parameters for trace element analysis

The accurate measurement of the trace element content in a solid is dependent on two parameters; the dilution factor (DF) and the limit of detection (LOD), defined here. The DF is the correction factor applied to the concentration in the liquid solution to obtain the concentration in the solid. The dilution factor results from the sample preparation (digestion) procedure and the dilution required prior to analysis such that the total dissolved solid satisfy the ICP requirement. It is calculated as the volume of the solution (Vs) divided by the sample weight (Ms) and can therefore be defined as follows:

$$DF = \frac{V_s}{M_s} \qquad \text{Eq. 4-1}$$

The LOD is the lowest value at which one can confidently say the element exists in the sample (Charpentau 2009). Taking into account both instrumental sensitivity and sample preparation, the LOD is calculated as the concentration equal to three times the standard deviation of the background signal ($3\sigma_{bk}$) (or the 'procedural blank' – see section 4.2.3) multiplied by the known concentration in a calibration solution (γ_{cb}, e.g. 1ppm) divided by the mean of the raw counts of the blank ($\bar{x}_{bk}$) subtracted from the counts of the calibration solution $\bar{x}_{cb}$. These are quoted as concentration in the solid for each preparation procedure. The LOD may therefore be defined by Eq. 4-2

$$LOD = \left(\frac{3 \cdot \sigma_{bk} \cdot \gamma_{cb}}{\bar{x}_{cb} - \bar{x}_{bk}}\right) \qquad \text{Eq. 4-2}$$

The relative standard deviation (RSD) of the results for the unknown samples provides a measure of precision and is the standard deviation (SD) multiplied by 100 and divided by the mean ($\bar{x}$) Eq. 4-3:

$$RSD = \frac{(SD \cdot 100)}{\bar{x}} \qquad \text{Eq. 4-3}$$

4.3. Experimental Section

4.3.1. Preparation of solid samples for ICP-AES by wet acid digestion

The quantification of trace elements by ICP-AES or ICP-MS requires that the sample be dissolved in acidic solution. This was carried out using strong acids which also dissolve the trace elements (discussed below). Upon cycling, CaO sorbent produced from the cycling experiments (Chapter 3) was ground to – 90 µ by hand using a pestle and mortar (to avoid contamination from more convenient grinding methods) before undergoing a homogenisation step. The resulting $CaOH_2$ aliquots are accurately weighed to ~ 20 mg and the exact weights recorded to enable the DF to be calculated. The aliquots are placed into PTFE vessels of volume 7 ml and 1 ml of 69 % HNO_3 added. This was to leach elements from, in the case of limestone or CaO, the resulting calcium nitrate salts according to Eq. 4-4due to the subsequent heat and pressure applied at the microwave stage. The lids are secured and the vessels microwaved according to a heating regime (Table 4-3) to affect the hot acid digestion of the samples.

$$Ca(OH)_2(s) + 2HNO_3 \rightarrow Ca(NO_3)_2(s) + 2H_2O(l) \qquad \text{Eq. 4-4}$$

Table 4-3. Microwave heating regime.

Stage	1	2	3	4	5	6 (cooling)
Power (W)	250	0	250	400	600	0
Time (mins)	1	2	5	5	5	20

After 45 mins cooling at – 7 ºC (to ensure volatile elements are not released upon opening), the inside of the vessels are rinsed into 10 ml volumetric flasks via a small plastic funnel using 5 % HNO_3. The solutions are topped up to 10 ml to enable the DF to be calculated. The solution was then shaken and poured into a 50 ml centrifuge tube and drawn into a 20 ml plastic syringe. This allowed the solution to be filtered via a 0.45 μ Whatman filter into a 10 ml test tube ready for insertion into the ICP-AES.

4.3.2. ICP-AES Operation

The instrument was first warmed up for 75 minutes with argon flowing to the plasma to enable the plasma temperature to equilibrate, as advised the instrument user guide. A test sample was then inserted containing all elements in 1 ppm concentration. The results of this test sample allow the peak of each wavelength included in the analysis to be examined for interferences. This also allows for the correct positioning of peak measurement readings and baseline points i.e. on the baseline rather than on the wavelength peak of interest or another wavelength peak positioned nearby.

Calibration of the instrument at the start of each run was performed by analysing three multi-element solutions at concentrations of 0.125, 0.25 and 0.5 ppm respectively. The counts recorded for the 'standard blank' (i.e. the matrix solution, 5 % HNO_3) provides a baseline value for the calibration line. The x-axis shows the known concentration of the calibration solutions whilst the y-axis shows the counts recorded for each solution (e.g. Figure 4-3).

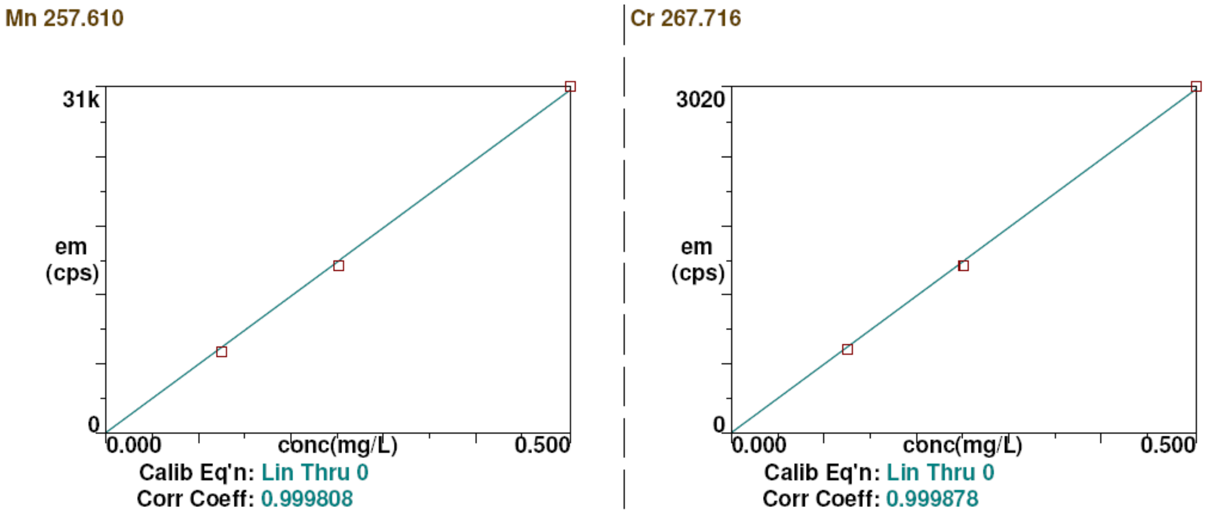

Figure 4-3. Examples of wavelength calibration for Mn (257.610 nm) and Cr (267.716 nm) showing correlation co-efficients for each line.

The unknown samples are then run after calibration. Each sample lasts ~ 6 minutes to allow all elements of interest to be registered including 25 seconds uptake time (for the solution to reach the plasma) and 60 seconds of washing using a 2 % HNO_3 solution to prevent contamination between samples. A 1 ppm 'drift' solution was analysed every 5 samples to correct for instrument sensitivity which varies as a function of time due to changes in ambient temperature and small fluctuations to the temperature of the plasma itself. The extent of the drift for one of the ICP-AES in-house machines used for this project was shown to be + 10 % over the course of an eight hour run (Figure 4-4).

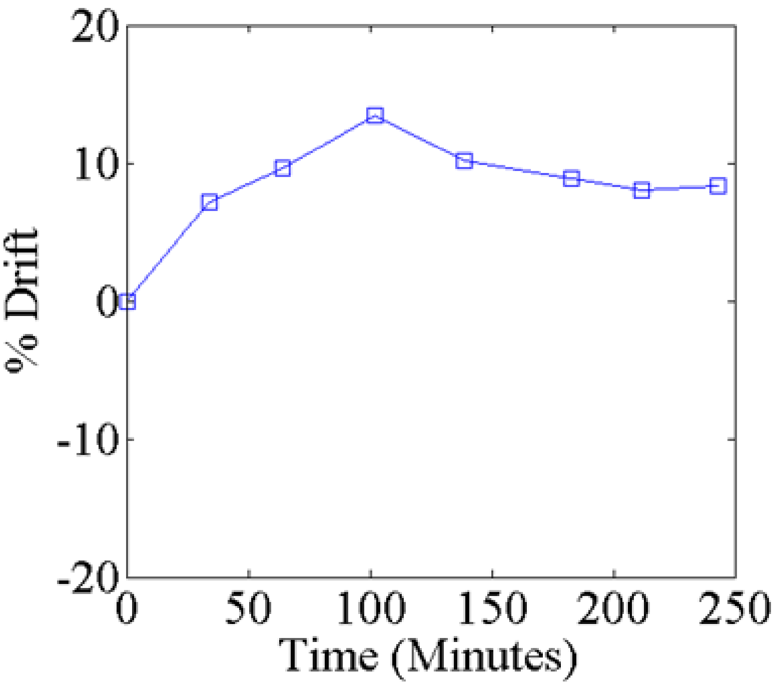

Figure 4-4. Example of ICP-AES drift over the course of a four hour run.

4.3.3. Converting ‘counts’ to sample concentrations

The element counts for each element in the unknown sample ($\bar{x}_{sp}$) first has the counts for the procedural blank ($\bar{x}_{bk}$) subtracted to account for any contamination introduced during the preparation procedure. The procedural blank consists of a solution containing all reagents used in the digestion of samples without containing the material undergoing analysis. This blank undergoes all of the preparation stages of a normal sample. Its purpose is to provide a background for contamination picked up during sample preparation. The blank-corrected counts are then multiplied by the gradient of the calibration line (β, e.g. Figure 4-3) to give the solution concentrations. This multiplied by the DF for each sample gives the concentration of each element in the original solid sample γ_{sp}.

$$\gamma_{sp} = \left(\bar{x}_{sp} - \bar{x}_{bk}\right) \cdot \beta \cdot DF \qquad \text{Eq. 4-5}$$

4.3.4. Determination of Spectral Wavelengths

The light wavelength selection was based upon the following factors (Boss and Fredeen 1997) :

- Purging ability of the instrument
- Analyte concentration vs. Emission line sensitivity (or detection limit, D.L.)
- Interferences from other wavelengths

Initially, wavelengths were run for all elements of interest. However the ICP-AES requires ~ 1 ml per element per sample which places a limitation on the number of wavelengths / elements that can be observed from a 10 ml sample to only ten wavelengths. Therefore it was necessary to determine the most suitable wavelength for each element based on the factors listed above. This section deals with this issue for the list of elements detailed in the background section of this thesis, which are listed again here:

As, B, Ba, Be, Bi, Cd, Cr, Cu, K, La, Li, Mg, Mn, Na, Ni, Sb, Sr, Ti, V, W, Y, V, Zn, Z..

The information used for this section has been taken from the Inorganic Ventures on-line interactive periodic table (Inorganic_Ventures 2013). According to (Gaines 2012), the data on this website is referenced from (Barnes 1981; Thompson and Walsh 1983; Montaser and Golighty 1992).

Aluminium (Al): Al has wavelengths at 167.078, 394.401 and 396.152 nm. The first wavelength is below the limit detectable by the machine whilst the third wavelength has a major interference with Mo. Therefore the 394.401 wavelength was used.

Arsenic (As): As has three spectral lines at, nm. The line with the lowest estimated D.L (189.042 nm) was below that detectable by the machine (i.e. below 190 nm), whilst the 228.812 line is known to have a strong interference with Cd. Therefore the 193.696 nm line was chosen. The solution concentrations of all input materials were below the LOD value for this line, indicating that As was not to be included in any further analysis.

Barium (Ba): Barium has spectral lines at 230.424, 233.527 and 455.403 nm. Although the wavelength with the best detection limit is 455.403, this is known to have an interference with Zr, whilst the 230.424 has an interference with Mo. The only line not to have an interference is 233.527 therefore this line was used.

Beryllium (Be): Beryllium has wavelengths at 234.861, 313.042 and 313.107. The first two both have interferences with elements likely to be present in the unknown samples (Fe and V respectively). The 313.107 nm wavelength has interferences with elements unlikely to be present in the samples (Ce, Th, Tm), and still has a useable estimated detection limit of 0.0007 ppm. However, the solution concentrations of all input materials were below the LOD value for this line, indicating that Be was not to be included in any further analysis.

Boron (B): Boron has spectral lines at 249.773, 249.678 and 208.959 nm. The 208.959 line is reported to have the least number of minor interferences (Mo) and no major interferences, whilst the other two lines have eight and five respectively. Therefore the 208.959 line was chosen.

Bismuth (Bi): Bi has wavelengths at 190.171, 206.170,. The 190.171 line showed poor sensitivity due to it being below 200 nm. Therefore it was necessary to use the 206.170 line. According to the peak produced from the 0.5 ppm solution, no interference was reported. However its close proximity to the 206.200 nm Zn line (Figure 4-5) indicates that care should be taken using this line for Bi if the reported solution concentration is above 0.5 ppm.

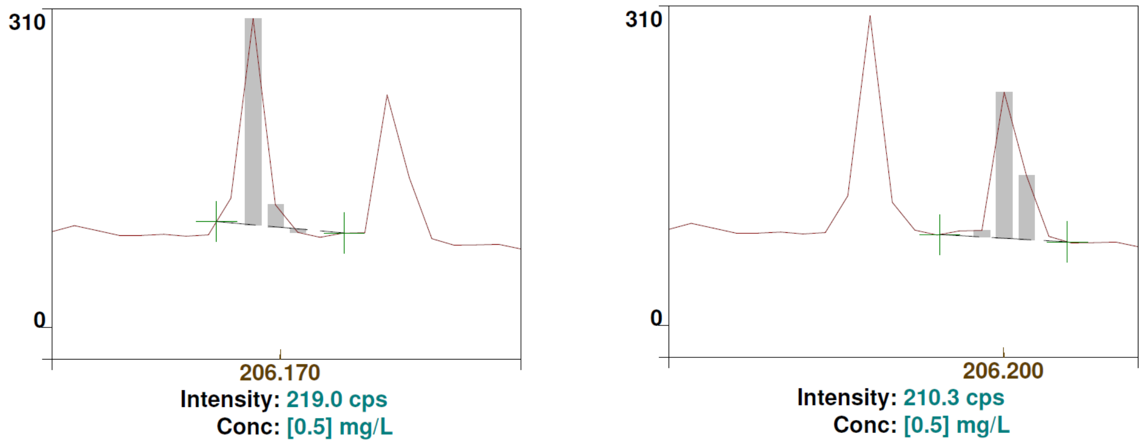

Figure 4-5. Wavelength peaks for a) Bi at 206.170 and 2) Zn at 206.200 nm (0.5 ppm).

However, the solution concentrations of all input materials were below the LOD value for this line, indicating that Bi was not to be included in any further analysis.

Cadmium (Cd): The 228.802 line is known to have a strong interference with As line 228.812, eliminating the use of this line. The other two lines have experimental LOD's of 0.0105360059 and 0.0051136520 respectively. Given the low expected concentration of Cd in all inputs, the line with the lowest LOD value (226.502 nm) should be used. However, the solution concentrations of all input materials were below the LOD value for this line, indicating that Cd was not to be included in any further analysis.

Chromium (Cr): Cr has wavelengths at 205.560, 267.716 nm and 283.563 nm. The solution concentrations reported by the 205.560 nm line were an order of magnitude lower than the LOD values calculated, whilst the R^2 value on the 283.563 nm was very low at 0.2257. Therefore the 267.716 line was used.

Copper (Cu): Cu has wavelengths at 219.958, 224.700 and 324.754 nm. A strong interference is known to exist with the second line. The other two lines have minor interferences with elements unlikely to be present in any of the samples to be analysed in this investigation (Nb, U, Th, Hf, and Ta). The 324.754 nm line has the lowest reported detection limit therefore this line was used.

Lanthanum (La): La was supposedly detected in all three fuels (La Jagua, 708.14; Lea Hall, 702.56; RDF, 680.88 ppm respectively) at the 407.735 nm line. However this is due to its close proximity with the 407.771 nm Sr line causing interference; the similarity between the shapes of the peaks corresponding to these two readings can be observed (Figure 4-6**).** This was confirmed by the 408.672 nm La line which reported solution concentrations of all input materials below the LOD value for this line.. Therefore the 408.672 nm La line would be used, however La was not detected in any of the inputs.

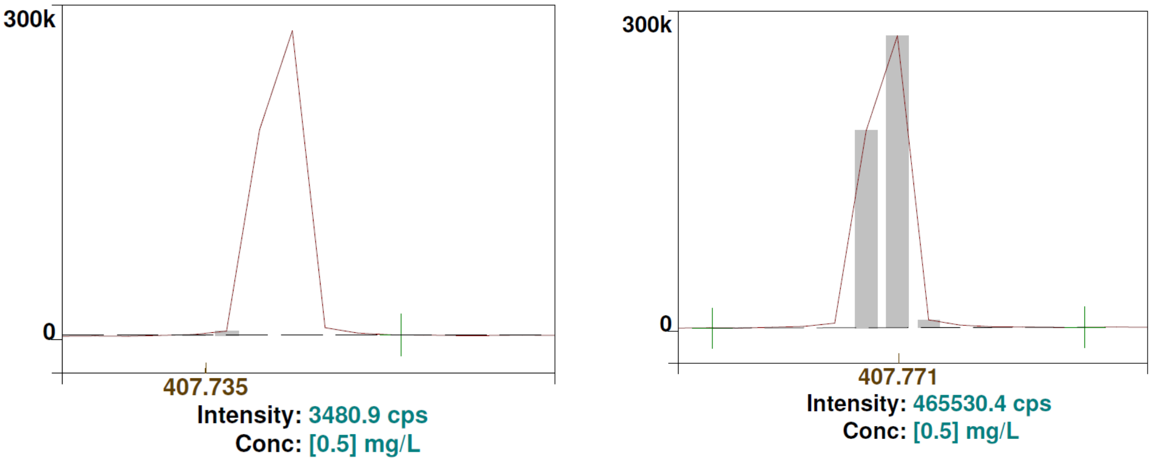

Figure 4-6 Spectral peak at a) 407.735 nm (La) and b) 407.771 nm (Sr) (0.5 ppm).

Lithium (Li): Li has wavelengths at 323.261, 460.286 and 670.784 nm. The first two wavelengths both report interferences with elements which may be present in the samples (Sn and Zr respectively) therefore the highest wavelength of 670.784 nm was used. This was also the wavelength with the lowest detection limit. However, the solution concentrations of all input materials were below the LOD value for this line, indicating that Li was not to be included in any further analysis.

Potassium (K): K has wavelengths at 404.721, 766.490 and 771.531 nm. It was found that no counts registered at either 404.721 or 771.531, potentially due to the high detection limit of these two wavelengths (1.1 and 1.0 ppm respectively). Therefore the 766.490 nm line was used which reported no interferences and a detection limit of 0.4 ppm.

Magnesium (Mg): Mg has wavelengths at 279.553 and 285.213 nm. The 279.553 nm line has the lowest detection limit of 0.0002 ppm whilst the 285.213 line has a small interference with Cr. However according to (Welz and Sperling 1997) the 279.553 nm line becomes non-linear even at very low concentrations. This was confirmed when standard reference material samples were run containing known concentrations of Mg. The results for the 279.553 were consistently lower than the certified value whilst the 285.213 garnered concentrations which matched that of the certified values. This suggested the small Cr interference with the 285.213 line was not significant enough to affect the results and therefore this line was used.

Manganese (Mn): Mn has wavelengths at 257.610, 259.373 and 260.569 nm. The 257.610 line offered the lowest detection limit with no interference from other elements therefore this wavelength was used.

Molybdenum (Mo): Molybdenum has spectral wavelengths at 202.031, 203.844 and 204.598 nm These lines reported experimental LOD's of 0.0360, 0.146 and 0.0630 ppm respectively. The 202.031 line provided a LOD value ~ 10 times that of the solution concentration in the fuel samples (~ 0.2 ppm) indicating that this was the line that should be used. However, the solution concentrations of all input materials were below the LOD value for this line, indicating that Mo was not to be included in any further analysis.

Sodium (Na): Na has wavelengths at 330.237, 588.995 and 589.595 nm. The first wavelength has known significant interferences with Znwhilst the 588.995 line registered no counts. Therefore the 589.595 line was used which also provided the lowest detection limit of 0.07 ppm

Nickel (Ni): Nickel has wavelengths at 221.647, 231.604 and 232.003 nm. The 232.003 line has a strong interference with Cr whilst the other two have small interferences with Si and Sb respectively. However the 231.604 line was used given that Sb is less likely to be present in the samples than Si (Figure 4-7). The 231.604 wavelength also offered the lowest detection limit.

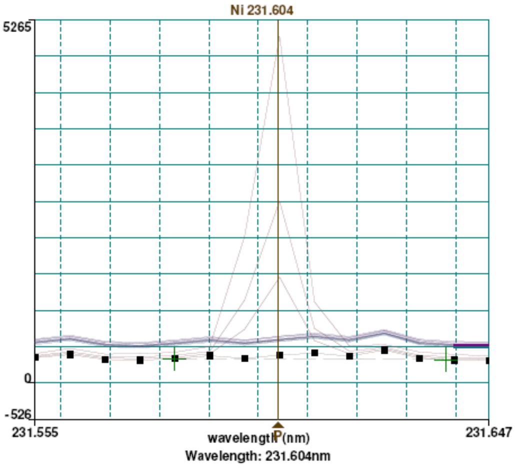

Figure 4-7. Strong Ni peak at 231.604 nm.

Phosphorous (P): P has wavelengths at 177.495, 178.287 and 213.618 nm. The first two wavelengths are below the minimum wavelength detectable by the ICP machine (i.e. below 190 nm). The 213.618 nm line has a strong interference with both Cu and Mo. However, the results of the limestone standard reference material suggested that this interference did not affect the results. As such the 213.618 nm line was used.

Lead (Pb): Pb has wavelengths at 168.215, 217.000 and 220.353 nm. The first wavelength is below 190 nm and therefore could not be used. The 217.000 nm reported interferences with Sb whilst the 220.353 line reported an interference with Sb, both elements potentially present in the samples. However the 220.353 offered the lowest detection limit therefore this wavelength was used.

The solution concentrations of all input materials were below the LOD value for this line, indicating that Pb was not to be included in any further analysis.

Antimony (Sb): Sb has wavelengths at 206.833, 217.581 and 231. 147 nm. All three report minor interferences with elements likely to be present in the samples (Cr, Fe and Ni respectively). However the solution concentrations in all inputs were below the limit of detection for all wavelengths therefore Sb was omitted from any further analyses.

Strontium (Sr): Sr has wavelengths at 407.771, 421.552 and 460.773 nm. No interferences were reported with any of these wavelengths therefore the 407.771 wavelength was used which offered the lowest detection limit of 0.0004 ppm.

Titanium (Ti): Ti has wavelengths at 323.452, 334.941 and 336.121 nm. All three wavelengths reported small interferences with elements which could be present in the samples; Cr, Mo / Co and Ni respectively. However the 323.452 wavelength offered the lowest detection limit of 0.0038 ppm therefore this line was used.

Vanadium (V): V has wavelengths at 290.882, 292.402 and 309.311 nm. The 309.311 line though offering the lowest detection limit of 0.005 ppm reported an interference with Mg. The other two wavelengths reported no relevant interferences therefore the 292.402 line was used which offered the lowest detection limit of 0.006 ppm.

Tungsten (W): W has wavelengths at 207.911, 209.475 and 224.875 nm. The 209.475 line reported an interference with Mo. The 207.911 line reported no interferences and offered the lowest detection limit therefore this line was used. However, the solution concentrations of all input materials were below the LOD value for this line, indicating that W was not to be included in any further analysis.

Yttrium (Y): Y has wavelengths at 360.073, 371.030 and 377.433 nm. None of these wavelengths reported any interference therefore the 360.073 line was used which offered the lowest detection limit of 0.005 ppm. However, the solution concentrations of all input materials were below the LOD value for this line, indicating that Y was not to be included in any further analysis.

Zinc (Zn): Zn has wavelengths at 202.548, 206.200 and 213.856 nm. All three wavelengths reported interferences with elements which may be present in samples, namely; Ni / Cu, Cu and Sb / Bi respectively. The 213.856 line offered the lowest detection limit therefore this line was used.

Zirconium (Zr): Zr has wavelengths at 272.261, 193.198 and 343.823nm. The 272.261 nm line reported a strong interference with Cr. The other two wavelengths reported no relevant interferences therefore the 343.823 line was used which offered the lowest detection limit of 0.007 ppm. However, the solution concentrations of all input materials were below the LOD value for this line, indicating that Zr was not to be included in any further analysis.

The wavelength choice for each element is given in Table 4-4 following the discussion above:

Table 4-4. Spectral wavelengths for elements of interest and prevalence in the inputs. 'X' indicates the presence of an element in an input; '-' indicates the absence. (Elements not highlighted in bold were removed from subsequent analysis).

Element	Wavelength (nm)	Detected in inputs			
		Longcliffe	La Jagua	Lea Hall	RDF
Al		**X**	**X**	**X**	**X**
As	193.696	-	-	-	-
B	**208.959**	**X**	**X**	**X**	**-**
Ba	**233.527**	**X**	**X**	**X**	**X**
Be	313.107	-	-	-	-
Bi	206.170	-	-	-	-
Cd	226.502	-	-	-	-
Cr	**267.716**	**X**	**X**	**X**	**X**
Cu	**324.754**	**X**	**X**	**-**	**X**
La	408.672	-	-	-	-
Li	670.784	-	-	-	-
K	**766.490**	**X**	**X**	**X**	**X**
Mg	**285.213**	**X**	**X**	**X**	**X**
Mn	**257.610**	**X**	**-**	**-**	**-**
Mo	202.031	-	-	-	-
Na	**589.555**	**X**	**X**	**X**	**X**

Ni	**231.604**	**-**	**X**	**X**	**X**
P	**213.618**	**X**	**-**	**-**	**-**
Pb	220.353	-	-	-	-
Sb	-	-	-	-	-
Sr	**407.771**	**X**	**X**	**X**	**X**
Ti	**323.452**	**-**	**X**	**-**	**X**
V	292.402	-	-	-	-
W	207.911	-	-	-	-
Y	360.073	-	-	-	-
Zn	**213.856**	**-**	**X**	**-**	**X**
Zr	343.823	-	-	-	-

4.3.5. Checking Repeatability of Results

Due to the sensitivity of the ICP-AES to external factors such as ambient room temperature, it was necessary to perform a check on machine integrity to enable reliable comparisons to be made between sorbents of different cycle numbers run on different dates (Table 4-5). The same sample was run on three different days over the course of three weeks for a range of elements.

Table 4-5.ICPAES results of same single-cycled ‘no fuel’ CaO sorbent run on 3 different dates over 3 weeks.

	Run 1		Run 2		Run 3	
	MEAN	RSD	**MEAN**	RSD	**MEAN**	RSD
Al	**290.69**	6.47	**299.50**	4.31	**262.62**	6.29
Ba	**47.92**	5.78	**50.03**	7.91	**47.57**	6.40
Cr	**4.04**	13.53	**4.18**	19.13	**4.78**	14.37
Cu	**7.75**	14.93	**7.20**	15.54	**8.43**	26.25
K	**112.83**	10.96	**117.21**	12.97	**90.93**	15.48
P	**20.00**	8.90	**21.19**	7.39	**20.29**	5.14
Mg	**1635.41**	3.89	**1628.23**	4.74	**1619.17**	4.95
Mn	**65.02**	3.65	**65.07**	4.85	**73.52**	3.32
Na	**117.38**	23.83	**65.48**	8.69	**145.20**	13.94
Sr	**67.26**	**9.47**	**72.11**	**16.46**	**66.29**	**17.50**

Comparing these concentrations, the results show that for all elements except Na it was possible to run samples on different dates without affecting the results, even for elements of very low concentration (e.g. Cr and Cu).

4.3.6. Efficacy of the Digestion Method for materials of interest

The deviation of the experimental values from the certified values provides a measure of the accuracy of the results for that digestion method and for the trace element procedure as a whole. A significant error between these two values suggests an issue in the procedure, and likely to be as a result of poor sample digestion. Figure 4-8 compares the experimental values for digesting NIST SRM 1d, (argillaceous limestone) against the certified values, whilst Table 4-6 shows the conversion of the concentration from % oxides given in the certified standard to elemental ppm concentrations as required in the experiments.

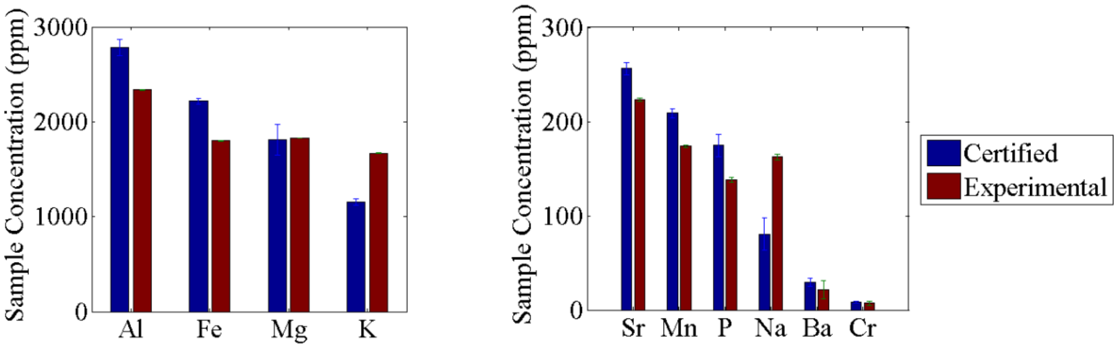

Figure 4-8. Comparison of experimental values against certified values for NIST SRM 1d (argillaceous limestone) for a. sample concentrations > 1000 ppm and b. sample concentrations < 1000 ppm. Average of six results. Error bars shown as RSD.

Table 4-6. Certified Values for SRM 1d Limestone, Argillaceous and conversions from % oxides to element ppm concentrations.

Oxide	Conc. (%, 3 s.f.)	± (%, 2 s.f.)	Element	Conc. (ppm, 3 s.f.)	± (ppm, 2 s.f.)
Na_2O	0.0109	0.0016	**Na**	80.9	0.74
MgO	0.301	0.010	**Mg**	1820	0.60
Al_2O_3	0.526	0.013	**Al**	2780	0.52
P_2O_5	0.0413	0.0025	**P**	180.2	0.43
S	0.1028	0.0062	**S**	1030	
K_2O	0.1358	0.0046	**K**	1130	0.83
Mn	0.00209	0.0005	**Mn**	209	5.0
Fe_2O_3	0.3191	0.0068	**Fe**	2230	0.69
ZnO	0.0022	0.0003	**Zn**	17.7	
SrO	0.0303	0.0010	**Sr**	256	
TiO_2	0.0306	0.0065	**Ti**	183	0.60
Cr_2O_3	0.0012	0.0002	**Cr**	8.21	0.69
BaO	0.0033	0.0011	**Ba**	29.6	

The results for Mg and Cu are excellent with experimental values close to the certified values. For most elements however the experimental values are slightly lower than the certified values. This suggests that not all of the material was being digested and that some of the elements are being lost, possibly during the filtration process. The experimental results for Na and K are both much higher than the certified values. The reason for this is currently unknown (see: Further Work).

4.3.7. Effect of a single calcination on trace elements

NB. This was early work during the PhD process therefore not all elements were analysed.

To ensure that loss of elements was due to repeated cycling and not a single cycle, a comparison was made between the original limestone and the sorbent homogenised after a single cycle (‘0’ cycles). Though these results are less relevant to Ca-Looping (than those for repeated cycling), a Ca-looping calciner will have a larger quantity of fresh limestone entering than a standard cement calciner due to the need to continually replenish and purge bed material. Therefore the release of volatile elements as a result of a single calcination becomes relevant from the point of view of calciner operation (due to potential build-up of problem elements in calciner components, e.g. ring-build-ups / filters etc.)

Due to the different form of the two samples (original limestone as $CaCO_3$ and calcined material as $Ca(OH)_2$ following homogenisation) it was not possible to directly compare concentrations; the concentrations in the calcined material would appear higher due to the fact the sample has a smaller mass following calcination. For a direct comparison, concentrations of each element (ppm) in the samples were converted to theoretical quantities contained in the original 100 g batch (mg) based on the relative atomic masses of $CaCO_3$ and $Ca(OH)_2$ respectively. The "student's t-test" was used to identify whether a change in the theoretical weight has taken place. The results indicate that the concentration of a number of elements changed as a result of a single calcination (Table 4-7).

Table 4-7. Sample concentrations (ppm) and theoretical weights (mg) and the results of the "Students" t-test comparing quantities (mg) of elements in single-cycled sorbent against the original limestone (x=mean, s=variance, DoF=degrees of freedom, Ho=null hypothesis). Results in green indicate rejection of the null hypothesis (Ho) due to a statistically significant increase in concentration following a single calcination; red marks indicate a decrease. Blank = no significant change.

	Longcal (Homog.)		**0 cycle ($CaOH_2$)**		**t-test parameters**		
	x2 ppm (mg)	**s2**	**x1** ppm (mg)	**s1**	**DoF**	**p-value**	**Ho**
Al	124.28 (12.06)	9.25108	299.50 (21.77)	0.88256	13	3.6E-4	🟩
Ba	12.68 (1.49)	0.00824	40.89 (3.64)	0.08280	13	1E-9	🟩
Cr	2.16 (0.21)	0.00006	4.18 (0.30)	0.00338	13	0.001	🟩
Cu	124.28 (0.72)	0.00903	7.20 (0.52)	0.00662	13	0.002	🟥
K	83.99 (8.15)	2.69523	117.21 (8.52)	1.22182	13	0.637	
Mg	1217.54 (118.10)	6.94377	1628.23 (118.37)	31.45362	13	0.902	
Mn	44.74 (4.34)	0.00582	65.07 (4.73)	0.05269	13	7E-4	🟩
Na	49.37 (4.79)	0.07712	65.48 (4.76)	0.17122	13	0.876	
P	16.51 (1.60)	0.00332	21.19 (1.54)	0.01294	13	0.195	
Sr	114.80 (11.14)	0.03985	72.11 (5.24)	0.74468	13	7.3E-9	🟥

The results show that Cu and Sr decreased whilst Al, Ba, Cr and Mn all saw an increase. The loss of elements would suggest devolatilisation during calcination. However , both Sr and Cu have boiling points above the maximum system temperature. An increase would suggest either contamination from the reactor / laboratory procedure, the liberation of elements due to heating and fluidisation or as a result of high variability of element concentrations within the limestone itself. However an alternative explanation may be presented to account for these findings. The differences observed may be attributable to the efficacy of the digestion procedure in digesting different types of sample. This possibility was tested by performing an experiment consisting of a single cycle of calcination followed by a single carbonation allowing the sorbent to be removed as $CaCO_3$. This enabled direct comparison of the cycled material against the original limestone. These results are shown in (Table 4-8).

Table 4-8. Example of “Students” t-test comparing concentration (ppm) of elements in single-cycled sorbent removed as CaCO3 against original limestone (x=mean, s=variance, DoF=degrees of freedom, Ho=null hypothesis). Results in green indicate rejection of the null hypothesis (Ho) due to a statistically significant increase in concentration following a single calcination; red marks indicate a decrease. Blank = no significant change.

	Longcal (Homog.)		**0 cycle ($CaCO_3$)**				
	x2 ppm (mg)	**s2**	**x1 ppm (mg)**	**s1**	**DoF**	**p-value**	**H_o**
Al	174.62 (16.94)	378.59	234.33 (22.73)	558.21	9	7.4E-4	🟩
Ba	23.20 (2.25)	9.22	29.54 (2.87)	22.21	9	0.81	
Cr	4.27 (0.41)	2.19	10.49 (1.02)	3.60	9	2.4E-5	🟩
Cu	9.20 (0.89)	0.40	9.19 (0.89)	0.24	9	0.92	
K	103.78 (10.07)	73.42	71.05 (6.89)	147.30	9	1.8E-7	🟥
Mg	1411.82 (136.95)	3145.19	1461.83 (141.80)	5618.64	9	0.597	
Mn	61.10 (5.93)	7.42	69.74 (6.77)	104.73	9	0.127	
Na	57.39 (5.57)	31.52	61.82 (6.00)	319.27	9	0.159	
P	22.10 (2.14)	1.74	21.37 (2.07)	16.57	9	0.23	
Sr	139.72 (13.55)	36.71	140.56 (13.63)	134.07	9	0.344	

Table 4-8 indicates that the single-cycled $CaCO_3$ contained a higher concentration of Al and Cr than the original limestone and a lower concentration of K. The decrease in K could be attributed to devolatilisation. The fact that the single-cycled $Ca(OH)_2$ samples contained less Sr than the original limestone whilst the single-cycled $CaCO_3$ did not suggests that Sr was easier to extract from $CaCO_3$ than $Ca(OH)_2$. Similarly, the fact that the single-cycled $Ca(OH)_2$ samples contained more Ba and Mn than the original limestone whilst the single-cycled $CaCO_3$ did not suggest that these two elements are easier to extract from $Ca(OH)_2$ than from $CaCO_3$. Al and Cr on the other hand saw an increase in both the $Ca(OH)_2$ and $CaCO_3$ samples. This could be attributed to the liberation of these elements from the limestone due to heating and fluidisation or due to contamination. The high concentration of Cr in the residue removed from one of the bed thermocouples (> 3500 ppm) suggests that Cr contamination from this source is a strong possibility. This contamination would have to take place in the first cycle given that Cr contamination was not detected in the cycling experiments. However the Cr contamination reported is well below a level likely to impact on clinker composition.

4.3.8. Observing S using IC

S is one of the elements of interest that cannot be observed on either of the ICP instruments available (see section 4.2.3) but can be observed using IC. The acidic solutions resulting from digestion of the solid samples are run through the machine similar to that of an ICP. It is found however that the high number of ions in the 5 % acid solutions prepared for ICP leads to a shift in the release of release time of the elements from the chromatograph column rendering the results unusable.This was found when using both NHO_3 and HCl as the digestion medium. The use of KOH crystals as to neutralize the solution before insertion was not found to remedy this issue. As such, S was omitted from analysis in this project despite its relevance to cement manufacture.

4.3.9. Concentration of Elements in the Input Materials

Analysis of the input materials was carried out to determine which elements should be included in the sorbent analysis and to enable mass balances on elements to be performed. Twenty of each sample type was digested and the mean values recorded to enable consistent comparison between the variability in element concentrations between each sample type (Table 4-9):

Elements shown to have high variability tend to be those of low concentrations; this was an expected finding. However some elements of higher concentrations show high variability in more than one instance despite sample concentrations above 100 ppm, e.g. Sr. Lea Hall coal showed the greatest consistency with no RSD values greater than the mean values.

4.3.10. Elements to be included in the analysis of sorbent

The list of elements to be included in the sorbent analysis was based on the lists of elements known to impact on alite production (as detailed in the Background section) and elements present in the inputs (see section 4.9 above). On this basis, the list of elements to be included in the analysis of sorbent cycled in the absence and presence of fuel respectively was given below. Elements shown to remain

Table 4-9. Concentration of trace elements in the inputs (mean of twenty samples, ppm).Cases where the RSD values are greater than or comparable to the mean value markedwith an asterisk (*).

Element	Longcliffe	+/- (RSD)	La Jagua	+/- (RSD)	Lea Hall	+/- (RSD)	RDF	+/- (RSD)
Al	112.65	47.45	979.49	22.07	2854.87	136.62	3826.17	35.63
B	6.22	81.82 *	15.89	26.10 *	69.13	9.01	-	-
Ba	8.42	56.04 *	277.11	146.79	173.87	44.95	135.29	47.66
Cr	2.12	47.81 *	5.70	114.04 *	17.50	123.15	35.55	68.56*
Cu	5.42	94.21 *	21.66	35.48	-	-	50.12	48.89*
K	93.81	47.75	113.40	115.24	46.06	107.12	1919.03	41.60
Mg	1405.17	12.55	1441.55	218.98	1081.55	95.43	1612.56	29.96
Mn	107.14	22.71	-	-	-	-	-	-
Na	102.94	37.82	135.70	18.51	1765.45	79.67	3289.31	38.45
Ni	-	-	9.04	96.21 *	30.57	76.20	19.89	65.75*
P	35.79	12.60	-	-	-	-	-	-
Sr	133.95	17.41	164.50	140.41 *	223.38	119.62	110.14	83.98*
Ti	-	-	411.60	128.10	-	-	54.27	53.21*
Zn	-	-	215.57	144.25 *	-	-	344.69	65.95

4.3.11.

the same upon cycling and not present in the fuel (e.g. Mn) are not included in the analysis of sorbent cycled in the presence of fuel, as follows (NB. Though not a trace element, Al was included in the analysis to determine ash retention in the sorbent):

In the absence of fuel: Al, B, Ba, Cr, Cu, K, Mg, Mn, Na, P, Sr.

In the presence of La Jagua combustion: Al, B, Ba, Cr*, Cu, K, Mg, Na, Ni*, Sr, Ti, Zn.

In the presence of Lea Hall combustion: Al, B, Cr*, Cu, K, Mg, Na, Ni*, Sr.

In the presence of RDF combustion: Al, Ba, Cr*, Cu, K, Mg, Na, Ni*, Sr, Ti, Zn.

* Cr and Ni are omitted from the results for sorbent cycled in the presence of fuel due to low concentrations in the sorbent in relation to the error bars produced.

4.4. Results & Discussion: Element Inventories in Cycled Sorbent

Sorbent cycled without and with fuel are digested and analysed for their trace element inventories. This was to determine whether cycling has an impact on the element inventory.

4.4.1. 'No Fuel' Experiments

In the 'No Fuel' experiments, sorbent was cycled fifteen times; this was the maximum number of 'No Fuel' cycles that can be achieved in a day. The trace element inventories of these sorbents are given in Figure 4-9.

a.

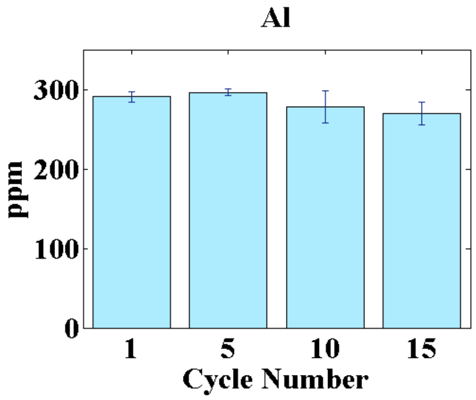

b.

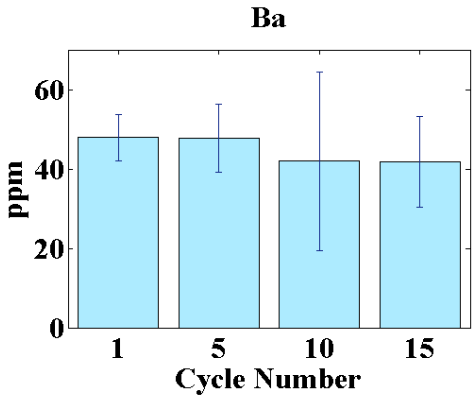

c.

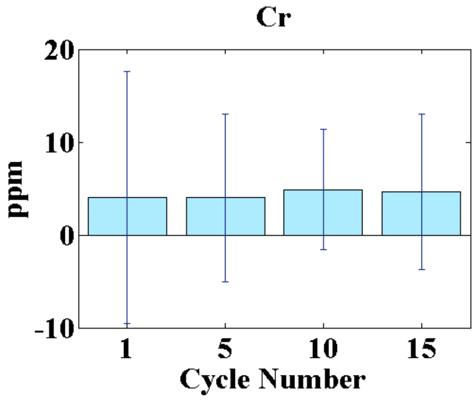

d.

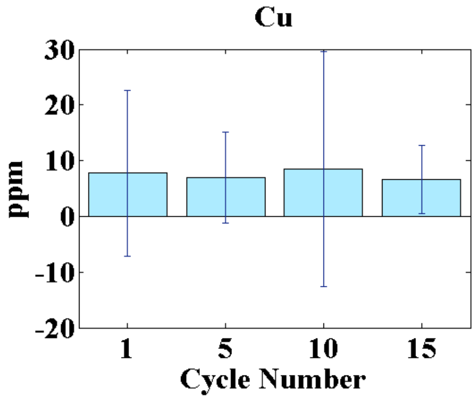

e.

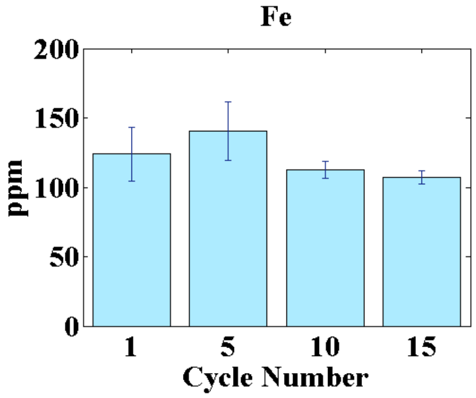
Fe
ppm
200
150
100
50
0
1
5
10
15
Cycle Number

f.

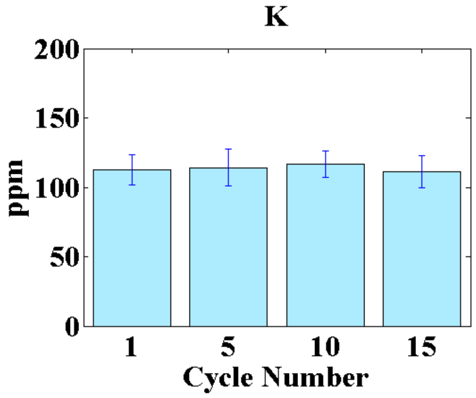
K
ppm
200
150
100
50
0
1
5
10
15
Cycle Number

g.

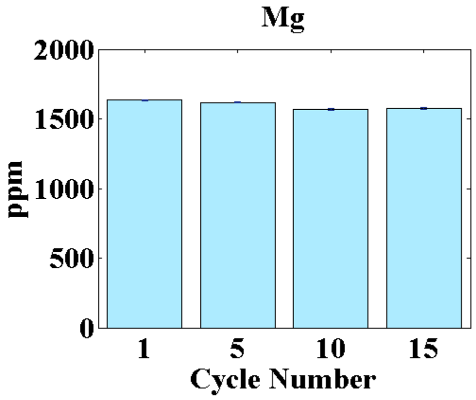
Mg
ppm
2000
1500
1000
500
0
1
5
10
15
Cycle Number

h.

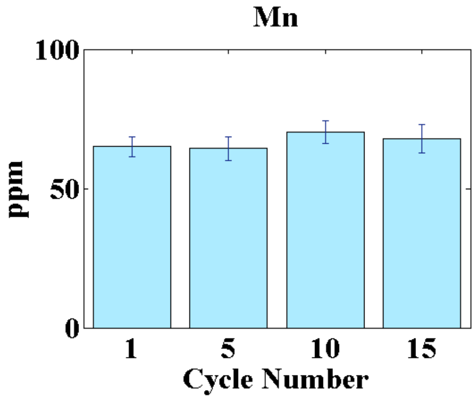
Mn
ppm
100
50
0
1
5
10
15
Cycle Number

i.

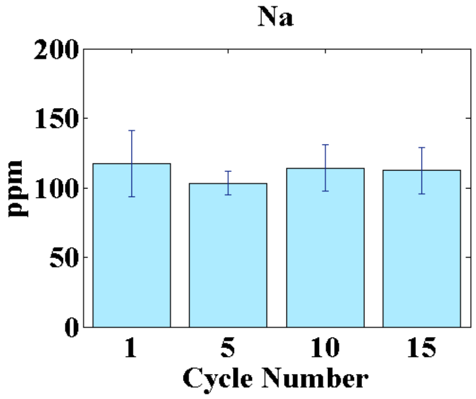
Na
ppm
200
150
100
50
0
1
5
10
15
Cycle Number

j.

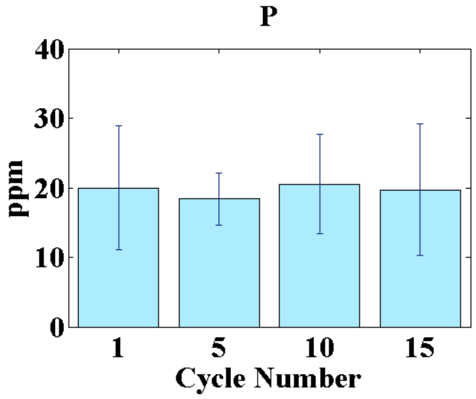
P
ppm
40
30
20
10
0
1
5
10
15
Cycle Number

k.

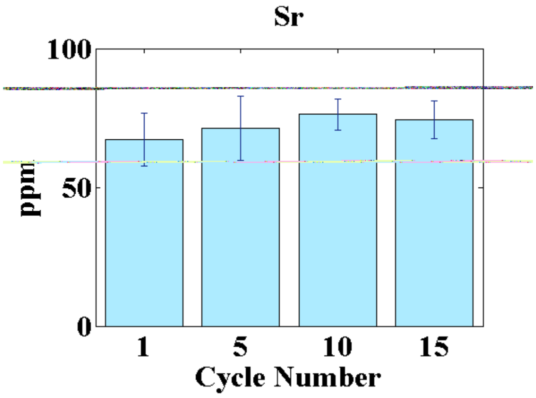

Figure 4-9 (a-k). Trace element inventories of sorbent cycled without fuel. Error bars shown as RSD values.

Given that all results remain the same within the experimental limits (indicated in Figure 4-9 as the RSD); these results indicate that subjecting the sorbent to up to 15 calcination / carbonation cycles in the absence of fuel does not affect its trace element inventory. This was an expected result given that the dissociation temperature for the elements included in the analysis is above that of the maximum system temperature.

4.4.2. Batch-fed Experiments

In the batch experiments coal was fed into the base of the spouted bed in 2 g charges on each cycle. These experiments served as an initial test as to whether inserting coal at these sorts of quantities does impact on the trace element inventory of the cycled sorbent, before proceeding with the continuously-fed fuel experiments (Figure 4-10).

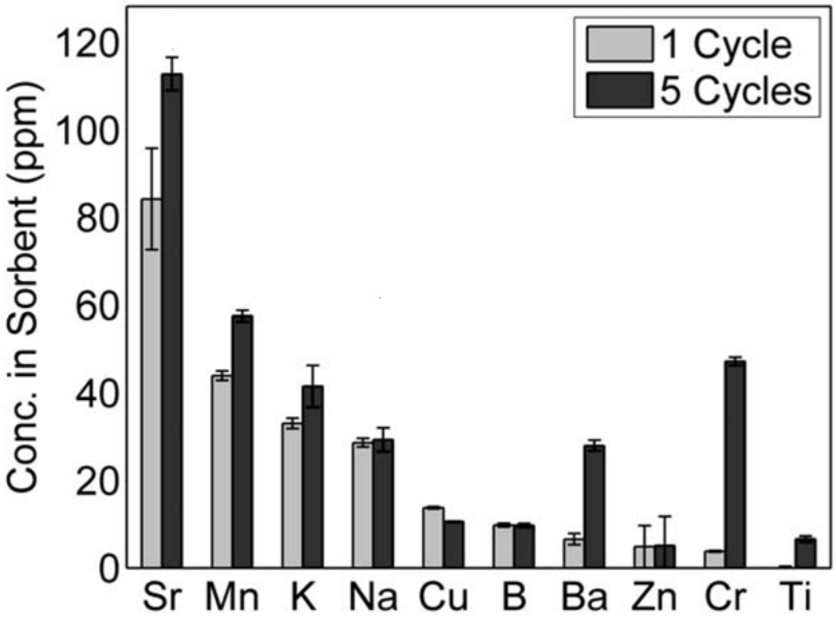

Figure 4-10. Trace element inventories of sorbent upon cycling in the presence of batch fed La Jagua. Error bars shown as RSD values.

The results show that in the initial experiments an increase in the trace element concentration was observed for Ba, Cr, K, Mn, Sr, and Ti. B, Na and K remain the same, whilst Cu sees a small decrease. Cr saw a particularly large increase. This suggests that the batch-fed coal system was effective in introducing powdered coal into the bed of limestone.

4.4.3. Continuously-fed Experiments

In the continuously-fed coal experiments, sorbent was cycled five and eight times for the coals and three and five times for the RDF respectively. The number of cycles for the coal experiments is based on the number of cycles experienced by the sorbent for a Ca-loop integrated with a cement kiln as derived by the stochastic model (see: Flowsheeting Chapter section 2.2.1). The number of cycles for the RDF experiments is limited by the number of pellets that can be produced in a morning before carrying out the experiments in the afternoon (see: Production of Spent Sorbent Chapter section 3.1.5). The trace element inventories of these sorbents are given in (Figure 4-11).

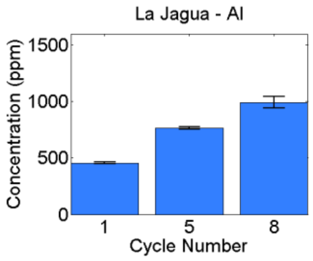

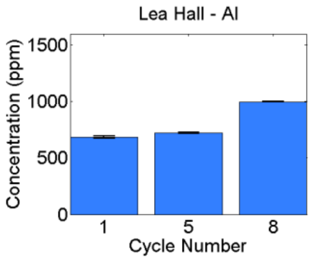

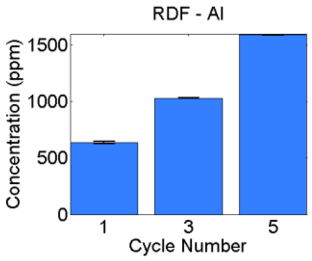

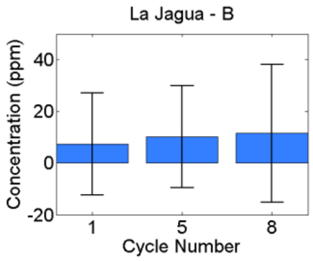

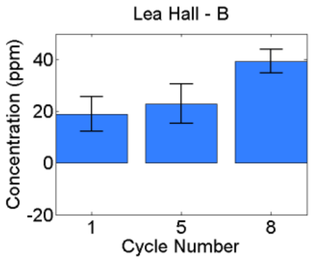

No B analysis undertaken

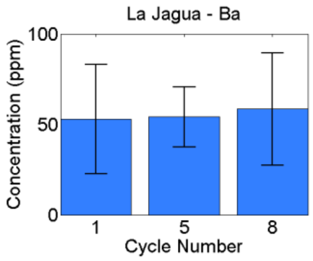

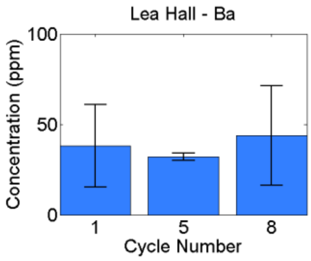

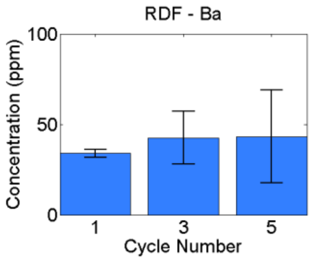

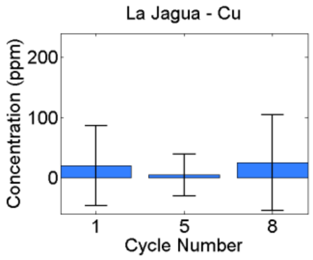

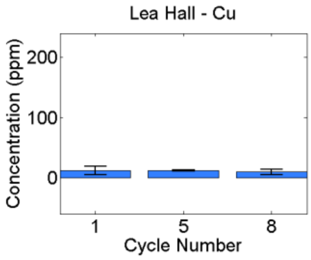

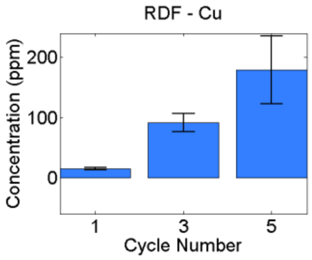

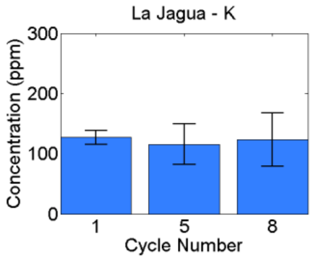

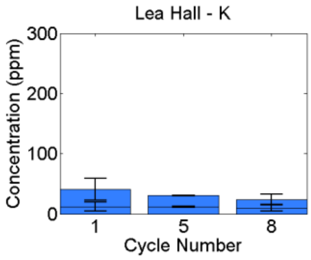

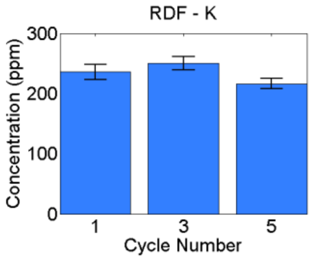

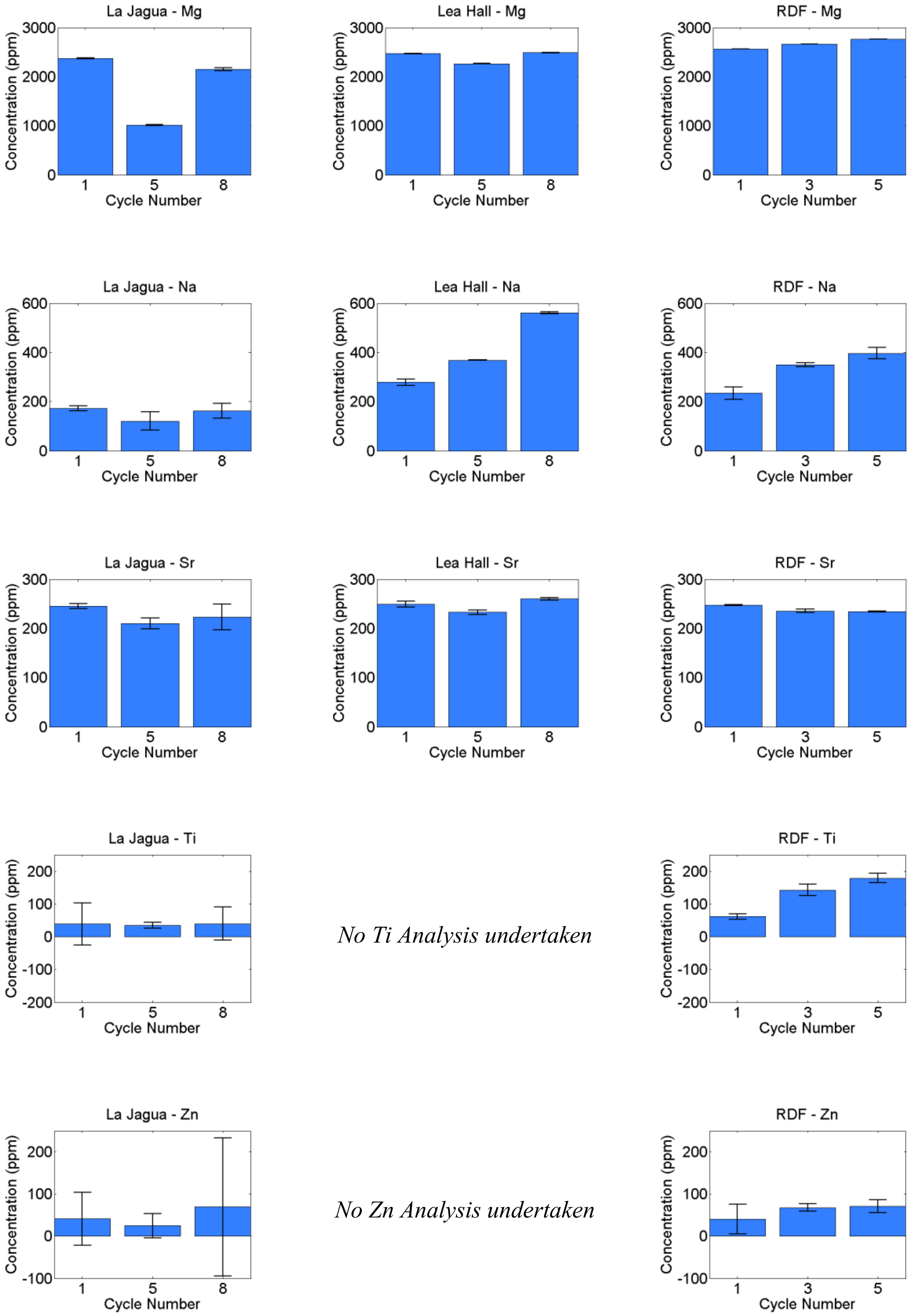

Figure 4-11. Trace element inventories of sorbent upon cycling in the presence of continuously fed fuel (La Jagua, Lea Hall and RDF). Error bars shown as RSD values.

Figure 4-11 indicates that based on the increase in Al content, some ash did mix in with the sorbent for all sorbents produced in the presence of fuel combustion. For the experiments with fuel, the trace concentration of Ba, K, Sr and Zn remained the same where present in the original fuels. For Lea Hall, B sees an increase over eight cycles from ~ 20 to 40 ppm, exceeding the experimental limits (RSD); thought does not for La Jagua. This was also the case for the La Jagua batch experiments where the concentration of B remained the same despite being present in the original fuel. For Cu, the low level concentrations in the sorbent on the first cycle (~ 15 ppm) remains the same over eight cycles for the two coals, though sees an increase over five cycles for the sorbent cycled in the presence of RDF from ~ 20 ppm to ~ 180 ppm. Na remains the same for the sorbent cycled in the presence of La Jagua, though sees an increase in the results for Lea Hall and RDF from ~ 250 to ~ 550 ppm and from ~ 200 to 400 ppm respectively. This was an expected result given that the Na content of the La Jagua coal is an order of magnitude lower than that of the other two fuels. Ti remains the same for La Jagua over eight cycles, though sees an increase in the sorbent cycled in the presence of RDF over five cycles from ~ 50 ppm to ~ 150 ppm.

Some of these results are expected whilst others are not. An expected result would be an increase in the trace element inventory over repeated cycles for every case where non-volatile elements are present in the original fuel. However it was found that this is not always the case.

4.4.4. Mass Balances on Elements

Mass balances have been calculated with upper and lower bounds using the RSD values of the incoming fuel and the results for cycled sorbent for elements shown to have increased upon cycling (Table 4-10 -Table 4-14).

Table 4-10. Results for % retention of Al in cycled sorbent.

Fuel / Cycle No.	Lower	Absolute	Upper
La Lagua			
1	104.40	**133.79**	183.59
5	75.17	**84.97**	97.23
8	65.86	**75.20**	86.24
Lea Hall			
1	97.54	**112.50**	137.43
5	30.47	**32.19**	35.66
8	26.70	**28.82**	32.56
RDF			
1	75.41	**85.09**	98.00
3	33.72	**35.13**	36.95
5	33.09	**34.82**	36.94

Table 4-11. Results for % retention of B in cycled sorbent.

Fuel / Cycle No.	Lower	Absolute	Upper
Lea Hall			
1	-7.47	**34.98**	316.23
5	-4.67	**16.81**	69.84
8	-6.44	**12.77**	55.64

Table 4-12. Results for % retention of Cu in cycled sorbent.

Fuel / Cycle No.	Lower	Absolute	Upper
RDF			
1	4.29	**7.11**	9703.25
5	23.69	**38.66**	12177.72
8	52.09	**69.17**	12716.67

Table 4-13. Results for % retention of Na in cycled sorbent.

Fuel / Cycle No.	Lower	Absolute	Upper
Lea Hall			
1	52.70	**63.81**	81.51
5	24.26	**25.47**	27.96
8	0.00	**25.48**	54.91
RDF			
1	23.97	**24.87**	41.72
3	11.94	**12.39**	14.85
5	8.17	**9.37**	11.67

Table 4-14. Results for % retention of Ti in cycled sorbent.			
Fuel / Cycle No.	**Lower**	**Absolute**	**Upper**
RDF			
1	4.29	**7.11**	9703.25
5	23.69	**38.66**	12177.72
8	52.09	**69.17**	12716.67

The mass balances for Al (Table 4-10) indicate the % retention for this element decreases with cycle number for all elements. This suggests that the amount of ash entering and leaving the system is reaching equilibrium as cycle number increases. Given that the amount of ash leaving will increase over a given period of time, after a certain point the amount of ash entering and leaving will remain constant. The difference in the results for Al for the three fuels is likely to be down to differences in the nature of the fuels. For example, the retention of Al for Lea Hall on the fifth and eighth cycles was much lower than that of La Jagua, suggesting an increased friability of this fuel. The retention of Al for RDF was also lower suggesting that the nature of this fuel, the difference in the feeding system and its combustion characteristics in relation to the coal granules played a role in the results observed.

The same trend was also shown for all results relating to B and Na (Table 4-11, Table 4-13), suggesting that these elements are being retained in the sorbent via the ash and not through dissociation from the solid fuels and reaction with the sorbent. The other elements (Cu and Ti) showed considerable errors in the mass balances; this could be accounted for by the high variability in the concentration of these elements in the original limestone and in the fuel (RDF) (Table 4-9). The presence of Ti in the stainless steel RDF feeder could also account for the mass balances being considerably higher than 100 % for this element.

The increase in B suggests that this element would have implications in terms of the cement chemistry for cement produced from sorbent cycled with Lea Hall coal given the known effect of B on alite production (see: Background) suggesting that this element requires further observation for any future experiments using this coal.

Both the Na retained in the sorbent and that lost from the bed has implications in terms of volatile cycles. Na lost from the bed indicates that volatile cycles could develop in the Ca-looping calciner as Na was introduced in the fuel but not retained in the sorbent. Na retained in the sorbent will be passed to the kiln; the high kiln temperatures will cause this element to dissociate causing volatile cycles to form within the kiln and between the kiln and Ca-looping calciner. This could limit the amount of sorbent that can be passed directly to the cement kiln.

4.5. Conclusions

- The results of the single cycle experiments indicate that Sr is easier to extract from $CaCO_3$ than from $Ca(OH)_2$, whilst Ba and Mn were both easier to extract from $Ca(OH)_2$ than from $CaCO_3$. The results of these experiments also suggest that Cr contamination from the thermocouple is a strong possibility though well below any limit likely to impact on clinker composition.

- Sorbent cycled in the absence of fuel does not undergo a measurable change in its trace element inventory up to fifteen cycles.

- The fuel systems designed and built as part of this project are effective in introducing the fuel into the system and in enabling the ash to mix with the sorbent during combustion as indicated by the concentrations for Al in the sorbent cycled with fuel.

- The decrease in the % retention for Al and other elements with reasonable RSD values suggest that an equilibrium is reached for the amount of ash entering the system after a certain number of cycles

- The results show that B would need further observation given its observed increase over eight cycles and its known role in the formation of alite crystals.

- The results for Na indicate that this element could have implications in terms of volatile cycles developing both in the Ca-looping calciner and the cement kiln. Such features of the system could limit the amount of sorbent that can be passed directly to a cement kiln.

4.6. Further Work

- Further work would include producing and testing sorbent with a wider range of solid fuels to see which other elements may be of interest in terms of their retention in the sorbent and their behaviour under calcination / carbonation conditions.

- Further work would include to ascertain why when digesting NIST SRM 1d (argillaceous limestone) experimental values for Na and K were much higher than the certified values.

Chapter 5. Investigation into the effect of using repeatedly cycled sorbent on phases in cement

5.1. Chapter Summary

The aim of this chapter is to determine the wt % alite in the clinkers produced from cycled sorbent. It was first necessary to develop a method for producing clinker in the laboratory which is described below. Both X-ray Diffraction (XRD) and X-ray Fluorescence (XRF) analytical techniques were then used. It was found that XRD was the more useful of the techniques as it enabled both the identification of alite polymorphs and determination of % wt. in the clinkers through the production of a calibration curve.

5.2. Relevant Analytical Techniques

5.2.1. Fundamentals of X-Ray Diffraction (XRD)

A crystal is any material whose constituent atoms, molecules, or ions are arranged in an ordered pattern extending in all three spatial dimensions. The distance between these atomic planes or layers can be referred to as the lattice parameters or lattice plain spacing (d_{hkl}, Ǻ), i.e. the distances between the layers. The type of crystal can be identified by measuring these distances; X-ray diffraction (XRD) is a well developed method for achieving this.

An X-ray is an electromagnetic wave with wavelengths (λ) between 0.1 and 10 Ǻ. These wavelengths are comparable to the interatomic distances within crystalline materials. When X-rays encounter such material, they are scattered by the electrons. The field of the X-rays causes the electrons within the material to oscillate and these electron oscillations are the starting point of secondary waves of the same frequency and wavelength as the X-ray "primary" waves. These secondary waves are not physical "reflections" of X-rays, though considering them as such is correct in a geometric sense and provides a means of measuring the lattice plane spacing from the X-ray wavelength, the order of reflection (n) and the angle of incidence / reflection (θ) (Figure 5-1). This is known as Bragg's law (Eq. 5-1):

$$n\lambda = 2d_{hkl}sin\theta \tag{Eq. 5-1}$$

Two X-ray beams of the same phase and wavelength approach the crystal and are scattered from two different atoms within it. The lower beam travels an extra length of $2dsin\theta$. These waves superimpose when this length is equal to or an integer multiple of the wavelength of the X-rays and constructive interference occurs. Constructive interference gives rise to the different diffraction phenomena seen in XRD. The smallest repeating structure in the lattice of a crystalline material is referred to as a 'unit cell'. It is these repeating unit cells that give rise to the constructive interference defined by Bragg's law.

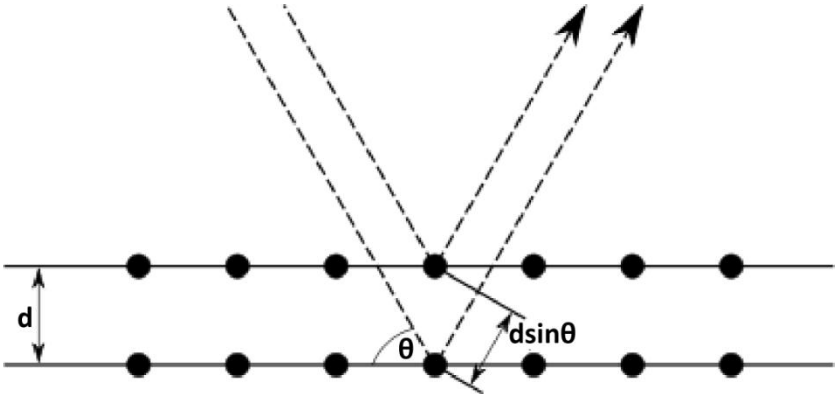

Figure 5-1. Bragg diffraction.

The intensities (I_i) of X-rays diffracted by phase component *'i'* were shown by Klug and Alexander (Klug and Alexander 1954) to be related to weight fraction (x_i), density (ρ_i) and the mass absorption co-efficient (μ_i) by Eq. 5-2 (where K_i is a constant which depends upon the geometry of the diffractometer and the nature of component i):

$$I_i = K_i * \frac{\left(\frac{x_i}{\rho_i}\right)}{\sum \mu_i * x_i}$$ Eq. 5-2

As such peak intensity is roughly proportional to the abundance of that phase. However this relationship is usually not linear due to phase and sample absorption. The mass absorption co-efficient (μ/ρ) is a measure of how strongly a material absorbs or reflects the X-rays. This becomes important when the material under examination contains more than one phase, and for quantitative analysis. A list of mass absorption co-efficients relevant to cement manufacture are given in (Table 5-1).

Table 5-1. Mass absorption co-efficients of compounds commonly found in cement.

Phase	**Composition**	**μ/ρ**	**Phase**	**Composition**	**μ/ρ**
Alite	Ca_3SO_4	92.3	Thenardite	Na_2SO_4	35.0
Belite	Ca_2SiO_4	89.5	Gypsum	$CaSO_4{\bullet}2H_2O$	82.4
Aluminate	$Ca_3Al_2O_6$	85.9	Bassanite	$2CaSO_4{\bullet}H_2O$	70.1
Aluminate	$NaCa_4Al_3O_{10}$	79.0	Soluble Anhydrate	$2CaSO_4{\bullet}2H_2O$	70.1
Ferrite (Low Al)	$Ca_4Fe_4O_{10}$	177.7	Anhydrate	$CaSO_4$	74.1
Ferrite	$Ca_4FeAl_3O_{10}$	107.1	Rutile	TiO_2	129.3
Periclase	MgO	27.8	Corundum	Al_2O_3	31.4
Free Lime	CaO	119.1	Silicon	Si	60.6
Arcanite	K_2SO_4	84.8	Flourite	CaF_2	91.9

5.2.2. Quantitative X-Ray Diffraction (QXRD)

XRD can be used to quantify as well as identify phases in a composite material. Cement clinker is a material of at least four phases, each with a different chemical composition and therefore a different level of X-ray absorption. Klug and Alexander (Klug and Alexander 1974) showed that an absorption correction can be made by the use of an internal standard and calibration curves which effectively "flush out" the differences in mass absorption co-efficients.

5.2.2.1. The Internal Standard Technique

Because of differences in the mass absorption co-efficient (μ / ρ) of each phase present in the material, the integrated intensity of reflection *i* of component *J* is given by Eq. 5-3:

$$I_{ij} = \frac{K_{ij} \cdot x_j}{\rho_j \left[X_j \left(\mu_j - \mu_M \right) + \mu_M \right]} \qquad \text{Eq. 5-3}$$

Where, $x_J$and ρ_J are, respectively, the weight fraction and density of the analyte, μ_J and $\mu_M$are the mass absorption coefficients of component *J* and the matrix, and K_{iJ} is a constant whose value depends on the diffracting power of component *J* and the geometry of the apparatus.

5.2.2.2. The Reference Intensity Ratio Technique

The Reference Intensity Ratio (or 'RIR') is defined as the ratio of the strongest peak of the unknown phase to that of an internal standard in a 1:1 mixture. In the case of clinker, RIR's were determined for the strongest non-overlapping peaks. Calibration using this method requires calculation of the RIR value. The method for this is as follows:

- Collection of diffraction patterns of individual phases for measurement of background-subtracted relative intensities (not required if one peak is used).
- Calculation of peak or pattern intensities and calculation of the RIR constant (Eq. 5-4):

$$\frac{I_{i\alpha}}{I_{js}} \cdot \frac{I_{js}^{rel}}{I_{i\alpha}^{rel}} \cdot \frac{X_s}{X_\alpha} = RIR_{\alpha s} \qquad \text{Eq. 5-4}$$

Where, I^{rel}_{js} is the relative peak intensity of diffraction peak *j* of internal standard *s*, $I^{rel}_{i\alpha}$ is the peak intensity of diffraction peak *i* of phase α, X_α is the mass fraction of phase α and X_s the mass fraction of internal standard *s*.

However, it is possible to generate semi-quantitative results using RIR values published in the ICDD database according to Eq. 5-5, where X'_α is the mass fraction of phase α after correction for the presence of corundum in the sample:

$$X'_\alpha = \frac{X_\alpha}{(1 - X_s)} \qquad \text{Eq. 5-5}$$

Both the use of RIR values from the ICCD database and the generation of experimental RIR values have been tried in the course of this investigation, as described below (section 5.3.3)

5.2.3. Fundamentals of X-Ray Fluorescence (XRF)

X-ray fluorescence (XRF) is the emission of characteristic "secondary" (or fluorescent) X-rays from a material that has been excited by bombarding with X-rays. Ionization of the atoms take place when the material is exposed to short-wavelength X-rays or (‘gamma’ rays), and as such results in the ejection of one or more electrons from the atom. The removal of an electron in this way renders the electronic structure of the atom unstable, causing electrons in the higher orbital to fall into a lower orbital to fill the hole left behind. In falling, energy is released in the form of a photon, the energy of which is equal to the energy difference of the two orbitals involved. Thus, the material emits radiation which has energy characteristic of the atoms, enabling the elements present in the substance to be identified.

5.3. Experimental Section

5.3.1. Developing a method for producing laboratory OPC

The raw materials were acquired or prepared according to the following size fractions to enable the formation of clinker phases; CaO, Al_2O_3 and Fe_2O_3 90% to pass – 90 μ; 100 % SiO_2 to pass a – 45 μ sieve. Al_2O_3 and Fe_2O_3 were supplied in powder form from Fisher Scientific. – 45 μ SiO_2 was acquired from Sibelco Sands (product code HPF5). CaO was produced in the fluidised bed reactor through calcination of Longcal P25 limestone (in the absence of fuel), supplied by Longcliffe quarries, and ground to the required size fraction in a pestle and mortar. The four materials were then proportioned as follows to produce a synthetic raw meal; 68.3 % CaO; 22.7 % SiO_2; 0.05 % Al_2O_3; 0.04 % Fe_2O_3. Enough material was produced to fill a 100 mm alumina boat (short enough to fill but not exceed the 120 mm high temperature region of the horizontal tube furnace, see Figure 5-2) and fired at 1450° C (furnace wall temperature). (NB. It was estimated that at this wall temperature the inside of the furnace was estimated to be ~ 50 ° lower at 1400 °C based on the temperature profile at 1300 ° C, due to the maximum temperature of the thermocouple inside the furnace being 1350 °C). XRD was then used to identify the presence of alite based on peak position (see section 5.3.2)

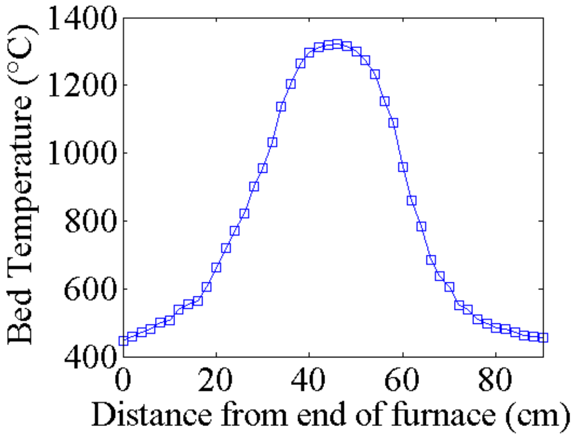

Figure 5-2. Temperature profile of the horizontal tube furnace (Max. temperature of 1297 °C for a wall set-point of 1350 ° C).

The results show that mixing the materials by hand in this fashion results in a high belite clinker (green line on Figure 5-3). Compressing the clinker to 100 bar increases the alite content (red line). Lastly, rapidly cooling the clinker after firing shows a further increase in the size of the alite peak (blue line). (NB. At first an alumina boat was used to hold the clinker brick whilst firing. However on occasions this boat cracked during the rapid cooling stage due to thermal shock. Therefore a platinum boat was used instead).

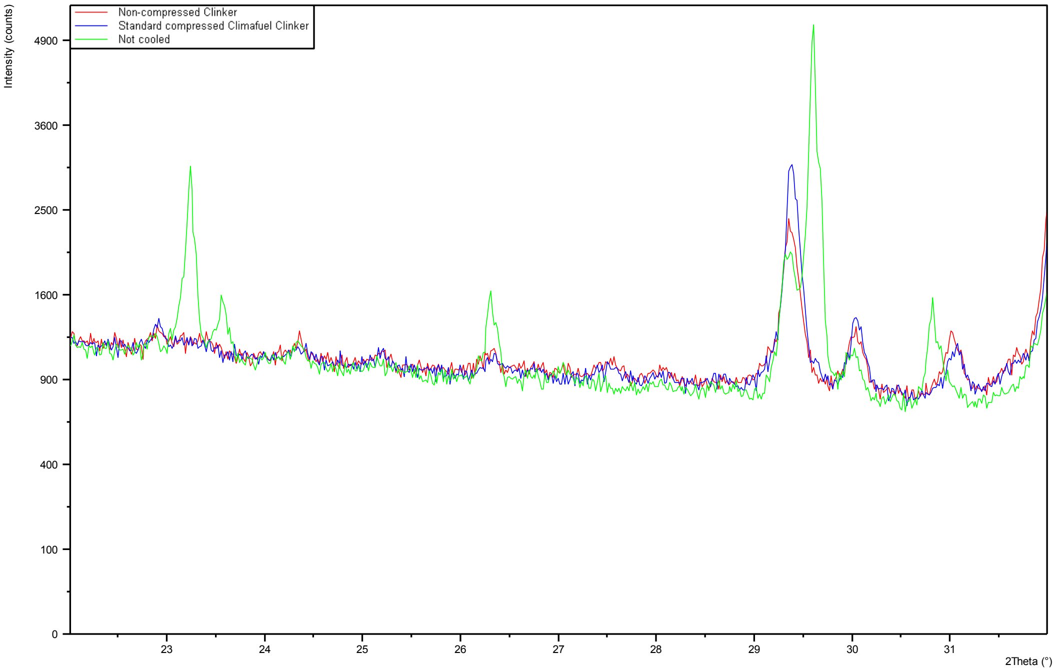

Figure 5-3. Alite and Belite Peaks for compressed but not cooled (green line), cooled but not compressed (red line) and both (blue line). XRD settings: Scan step size: 0.0167, Time per step: 60 seconds).

After pressing the brick, the maximum amount of material that could be fitted into the boat after pressing was 50 g; this is important to mention as it dictated how much sorbent was used from the cycling experiments.

5.3.2. Identifying alite and belite polymorphs using XRD

Guidance for the identification of alite and belite polymorphs has largely been taken from (Stutzman 1996). This section describes the identification of alite and alite polymorphs by peak position and shape for three types of clinker / cement; an industrial cement, a NIST cement standard reference material and the clinker produced in the laboratory.

The main peaks for alite and belite (~ 31.5 – 45 ° 2θ) overlap rendering this range unusable for identification of either phase. Therefore the polymorphs of alite thought to commonly occur in industrial clinkers based on their geometry (M_1, M_3 and T_1) are distinguished by the diffraction lines occurring at 51 – 51.5 ° 2θ. The M_1 polymorph is distinguished by a single peak at 51.7; M_3 by a well-defined doublet at 51.7; and the triclinic T_1 polymorph exhibiting a triplet between 51 and 52 ° 2θ. Figure 5-4 compares this peak for the three types of clinker/cement. For the industrial clinker, a slight doublet is visible indicating that the alite polymorph in this clinker was M_3. The other two clinkers exhibited a slight shoulder, suggesting these were also a doublet. This was confirmed by observing the same peak for the pure alite phase produced for the calibration line (see section 5.3.3) (Figure 5-4). This indicates that the peak is a doublet, and as such both this and therefore the laboratory clinker were of the M_3 polymorph (provided the selective extraction procedure described in section 5.3.3 had not caused a change in polymorph).

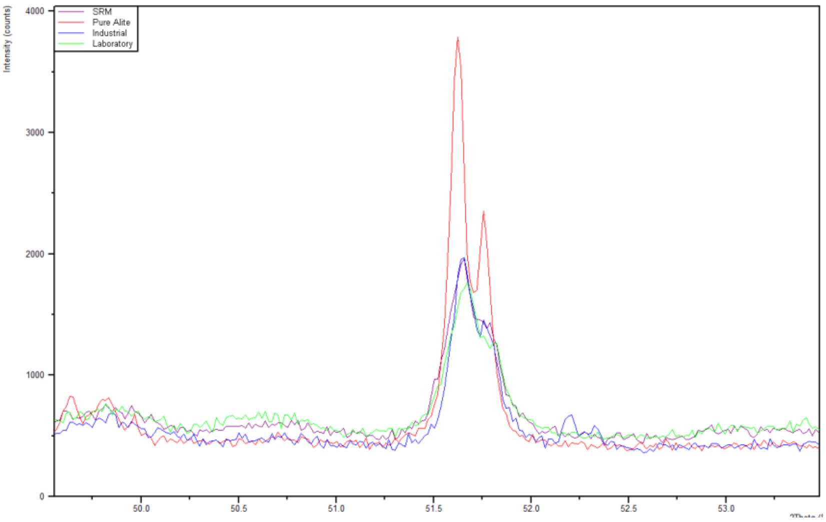

Figure 5-4. XRD scan from 49 – 54° 2θ showing the largest available alite peak at 51.7 2θ.

Quantitative analysis of β-C_2S is possible at the 31° 2θ peak, with a much weaker but still resolvable peak residing at 35.2 °. For identification of the interstitials, the C_3A cubic form exhibits strong singlet peaks at 33.3, 47.7 and 59.4, while the orthorhombic form exhibits splitting of the strong peak at 33.3 into a strong singlet at 33.2 and a weaker close doublet at 32.9 – 33. The XRD scan in Figure 5-5 exhibits a singlet peak at 33.3 suggesting that the C_3A in the laboratory clinkers is cubic; singlet peaks were also detected at 47.7 and 59.4.

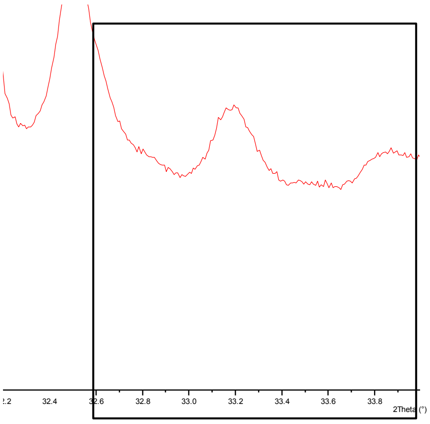

Figure 5-5.XRD scan from 32.6 – 34° 2θ showing a singlet aluminate peak at 33.2 2θ.

5.3.3. Developing a method for measuring % alite in the clinkers

The largest available peak for alite is at 30.4 ° (the larger peak at 51.7 ° cannot be used as the alite polymorph produced in the laboratory has been shown to be a doublet peak). Any changes in the proportion of alite and belite can be determined by calculating the ratio of the two background-subtracted peak area count intensities given that dividing through in this way negates any of the matrix absorption effects (as described in section 5.2.1). However, to determine the proportion of the two phases, single phase corundum (α-Al_2O_3) can be mixed with the clinker samples in a 1:1 ratio. The ratio of the alite and belite peak area intensities to the corundum peak indicate the abundance of that phase using the RIR value taken from the ICCD database However, using the RIR values from the PDF cards can only be deemed semi-quantitative given that the values have been determined on a different machine.

RIR values for alite can be found experimentally by fabricating alite as a single phase and producing a calibration curve for the phase of interest. Single phase alite was produced by a selective extraction procedure (Stutzman 1996). The first stage was to homogenise, press and fire commercial cement with $CaCO_3$ powder to convert all belite in the clinker into alite. The amount of $CaCO_3$ to be added needed to be such that all belite was converted to alite without any $CaCO_3$ remaining. This was difficult given that the proportion of belite in the commercial clinker was unknown. An approximate figure for commercial clinkers of 20 % was used indicating that 4 g of $CaCO_3$ was needed; XRD analysis confirmed that very little $CaCO_3$ was present in the resulting alite sample. The remaining phases (C_3A, C_4AF and $CaSO_4$) were then removed using a potassium hydroxide (KOH) / sugar selective extraction procedure. 30 g KOH pellets and 30 g sucrose were dissolved in 300 ml DI water at a temperature of 95 °C. The solution was filtered using a 0.45 µ Whatman filter and Buchner funnel via a vacuum pump. The remaining residue was washed with 50 ml of DI water, followed by 100 ml methanol (to prevent alite hydration) and dried at 60 °C.

The alite was then combined with a matrix material under different proportions (20, 50 and 70 % respectively) to produce a 1 g sample which was then mixed with 0.13 g of an internal standard (CeO_2) (Table 5-2). A calibration curve was produced by plotting the ratio of the alite peak intensity over the CeO_2 peak intensity plotted against the known phase proportions of alite (Figure 5-6).

Table 5-2. Weights used to produce calibration mixtures (g).

	C_3S	Fe_2O_3	CeO_2
Mix 1	0.2	0.8	0.13
Mix 2	0.5	0.5	0.13
Mix 3	0.7	0.3	0.13

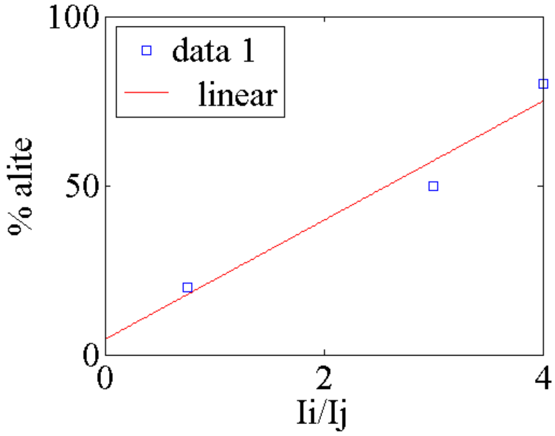

Figure 5-6. Calibration curve, R^2 value = 0.775.

Various matrix materials tested (MgO, $CaCO_3$ and SiO_2) indicated that interference between peaks was an issue in the production of the calibration curve. It was found that Fe_2O_3 was able to be used as a matrix material without the issue of interference with the alite or CeO_2 peak.

5.3.4. Quantification of clinker phases proportions using XRF

An attempt was made to quantify the proportion of phases in the clinker using the Bogue Equation (see: Background) by identifying the proportion of the four major compounds (CaO, SiO_2, Al_2O_3 and Fe_2O_3) via XRF. It was found that the equation outputted the % wt alite at over 100 %, which is clearly not possible. Although the Bogue equation is known to overpredict % wt alite in clinker, discussion with other users of XRF for similar purposes in the department suggested that this is due to the sample being in powder rather than pressed pellet form which is known to introduce error and prevent quantitative analysis. Therefore it was decided that XRD would remain the analytical method of choice for determining the proportion of alite in the clinkers.

5.4. Results and Discussion: % wt. of alite in clinkers produced from cycled sorbent

The production of spent sorbent described in Chapter 3 was then used in the production of clinker to determine whether cycling and the associated changes in trace element inventory of the sorbent impacts on the % alite in the resulting clinkers.

5.4.1. No Fuel or 2 g La Jagua per cycle

Figure 5-7 shows the results for the % alite in clinkers produced from cycled sorbent without fuel and in the presence of 2 g La Jagua being combusted per cycle. These results were generated by mixing the samples with corundum in a 50:50 mixture. For the clinker produced from sorbent cycled without fuel no change was detected outside the experiment limits up to fifteen cycles. However, clinker produced from sorbent cycled in the presence of La Jagua batch fed coal indicated an increase over the course of fifteen cycles from ~ 40 % to 52 %.

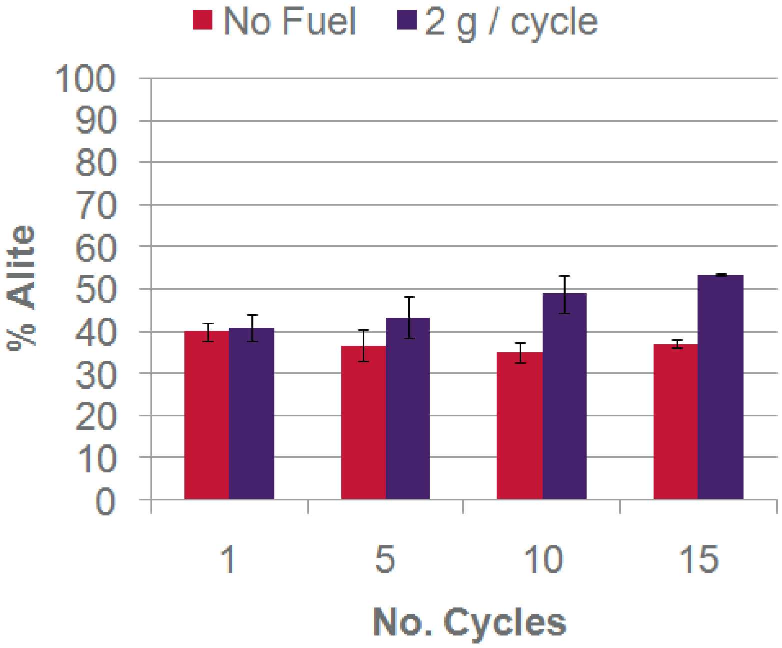

Figure 5-7. % wt. alite in clinkers produced from sorbent cycled without fuel and in the presence of La Jagua coal combustion (2 g / cycle). Error bars shown as RSD.

This suggests that the elements reported to have increased (see: Chapter 4, section 4.4.2) may be impacting on the % alite in the resulting clinkers. However, the high variability in the clinker produced from sorbent cycled without fuel suggests that increase observed in the clinker produced from batch-fed sorbent may be due to experimental error. The variations in the size of the error bars also suggest that this could be the case. This is further discussed below.

5.4.2. Continuously-fed coal and RDF

Figure 5-10 shows the results for the % alite in clinkers produced from cycled sorbent in the presence of continuously fed fuel; La Jagua coal, Lea Hall coal and RDF respectively. These results were generated by mixing the samples with 0.13 g of CeO_2 and using the RIR value calculated from Figure 5-6 to determine the % wt of alite. The results (Figure 5-8) show that no change was detected outside the experiment limits up to eight cycles for the coals and up to five cycles for the RDF respectively.

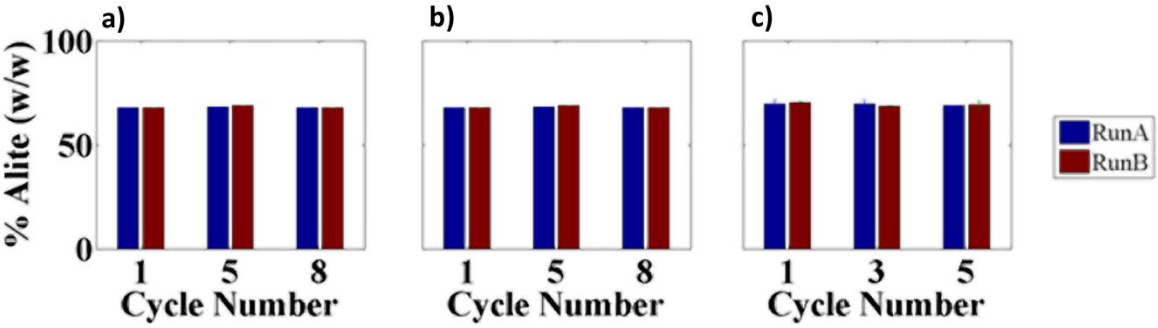

Figure 5-8. % wt. alite in clinkers produced from sorbent cycled in the presence of a) continuously fed La Jagua coal, b) continuously fed Lea Hall coal and c) RDF.

As such, the increase in % alite seen in the batch-coal experiments described in the previous section may be due to experimental error rather than due to the introduction of trace elements. This would be an expected result given that the change in the trace element inventories reported in Chapter 4 (section 4.4.2) are insignificant in comparison to the changes required to affect a change in % alite detailed in the background section of this thesis (see: Chapter 1, section 1.3).

5.5. Conclusions

- Methods have been developed to enable clinker to be produced in the laboratory with a % wt of alite comparable to commercial clinkers

- Methods have been developed to enable the intensity of X-ray diffraction peaks to be converted to wt % alite.

- XRF was not useful in accurately calculating the wt % alite in the clinkers using the Bogue equation; any further analysis using XRF would require pelletisation of the samples.

- Clinkers produced from sorbent repeatedly cycled in the absence of fuel did not lead to a change in the % wt alite, nor did cycling in the presence of continuously fed coal nor semi-continuously fed RDF.

- However, repeated cycling in the presence of 2 g of La Jagua did appear to effect a % wt change in alite over the course of fifteen cycles. This is either due to the incorporation of impurities from the fuel in the sorbent or experimental error

5.6. Further Work

- Larger numbers of clinker samples are required to enable definitive conclusions to be drawn with regards to the change in % wt. alite, in particular for the result with 2 g La Jagua batch-fed per cycle.

Chapter 6. Performance Tests

6.1. Chapter Summary

The aim of this chapter is to determine whether cement produced from cycled sorbent differs in mechanical performance to that of standard OPC. Due to the limited amount of sorbent that can be produced from the cycling experiments (~ 56 grams), the first stage is to miniaturise the tests by reducing the quantity of cement required whilst ensuring the test still complies with parameters set out in the standards. The tests used in this investigation are standard consistency (to determine the water / cement (w / c) ratio, cement setting time and compressive strength. The procedures for these tests are covered in British / European standards BS-EN 197-3 (standard consistency and setting time) (BSI 2008) and BS-EN 197-1 (compressive strength) (BSI 2005) respectively. These tests are also covered in the equivalent American standards ASTM C187 (standard consistency) (ASTM 2006), C191 (setting time) (ASTM 2008) and ASTM C109 (compressive strength) (ASTM) and respectively.

6.2. Theory behind the tests

6.2.1. Cement Consistence

Consistence describes the state of fresh concrete, which is the firmness of form of a substance or the ease with which it will flow (Neville 2010). The consistence or workability of concrete is important as it determines whether proper compaction can be achieved, and also the ease with which concrete can be transported, placed and finished without segregation. These can ultimately affect the strength, stability and durability of the concrete mix. Workability also allows for practicality in planning for construction works where contractors are able to plan and complete work on time before setting occurs.

6.2.2. Cement Setting Time

Setting time refers to the stiffening or change of phase of cement paste from a fluid to rigid state. In determining the setting time of cement, a cement paste of a standard consistence is immersed in water. The change of phase of cement is caused by selective hydration of C_3A and C_3S where the silicates and aluminate in cement form products of hydration or hydrates. These reactions are accompanied by a temperature rise of the cement paste. Setting times are defined by initial and final setting time. The initial setting time corresponds to a rapid rise in temperature whilst final setting time refers to the peak of the temperature rise (Neville 1991). Both tests measure the time it takes for the cement paste to develop some finite value of resistance to penetration.

The initial setting time of the cement paste is determined when the 1 mm diameter Vicat needle (see: section 6.3.4 below) under prescribed weight penetrates the paste and measures 6 mm from the base plate. There is a tolerance of ± 3 mm allowable by the British Standards. The initial setting time is recorded to the nearest 5 minutes from the time of cement first mixing with water. A minimum time of 45 minutes is prescribed by BS EN 197-1 for cement of strength classes 52.N and 62.5 N whilst 60 minutes is prescribed for strength classes of 32.5 N and R and 42.5 N and R (BSI 2005). The final setting time of the cement paste is determined by using a needle with ring attachment of diameter ~ 5 mm. The final setting time is when the needle penetration does not mark the specimen surface with a complete circular impression, i.e. the needle does not penetrate the cement paste for more than 5 mm. ASTM C191 (ASTM) provides a predictive method to calculate the final and initial setting time of the cement paste (Eq. 6-1) where E = time in minutes of last penetration > 25 mm; H = time in minutes of first penetration < 25 mm; C = penetration reading at time E; and D = penetration reading at time H:

$$\left(\left(\frac{H-E}{C-D}\right)\times(C-25)\right)+E \qquad \text{Eq. 6-1}$$

There are several factors that can affect the setting time of cement paste. These include cement composition, cement fineness, aggregate content, coefficient of thermal expansion, surrounding temperature and humidity. In the main these factors influence the adiabatic temperature rise of the cement paste which in turn effects the setting times. For example, low C_3S and C_3A contents are found to reduce excessive heat during hydration giving longer initial and final setting times. Lower fineness cement also produces slow hydration and reduces temperature rise (Moser). The British Standard specifies that the allowable tolerance for temperature is ± 2 °C and ± 1 °C for mixing and storing cement paste respectively with relative humidity in the range of 60 % - 90 %. To comply with the ASTM standard, two tests on similar pastes should not a have Vicat initial time difference of more than 34 minutes and a Vicat final time difference of more than 56 minutes (ASTM).

6.2.3. Compressive Strength of Cement

Strength of concrete is widely considered to be its most valuable property as it usually gives an overall picture of concrete quality because it is directly related to the structure of cement paste (Neville 1991). Compressive strength is defined as the maximum resistance of a concrete sample to an applied pressure and is the most common measure of performance when determining the suitability of concrete in the design of buildings and other structures. It can vary from of lows of 17 MPa and can exceed 70 MPa for certain applications. Results from compressive strength tests are used to determine the concrete mixture as delivered to meet the specified strength as required of any job.

Concrete mixture is designed such that the average strength is sufficiently higher than the specified strength. To comply with the strength requirements of a job specification, the average of 3 consecutive tests must equal or exceed the specified strength, and no single test should fall below the specified strength by more than 3.45 MPa or > 10 % when the specified strength is greater than 35 MPa. The compressive strength of a sample is calculated by dividing the failure load by the cross-sectional area resisting the load. Table 6-1 shows the mean compressive strengths of different cement types as listed according to ASTM C150-04a:

Table 6-1. Compressive strengths of different cement types according to European classification(Neville 1991).

Compressive strength, MPa (psi)	I	IA	II	IIA	III	IIIA	IV	V
1 day	-	-	-	-	12.0(1740)	10.0 (1450)	-	-
3 days	12.0 (1740)	10.0 (1450)	10.0 (1450)	8.0 (1160)	24.0 (3480)	19.0 (2760)	-	8.0 (1160)
7 days	19.0 (2760	16.0 (2320)	17.0 (2470)	14.0 (2030)	-	-	7.0 (1020)	15.0 (2180)
28 days	-	-	-	-	-	-	17.0 (2470)	21.0 (3050)

Strength, as well as durability and volume changes of hardened cement paste, depends not so much on the chemical composition as on the physical structure of the products of hydration of cement and on their relative volumetric proportions. A primary factor is porosity, i.e. the relative volumes of pores or voids in the cement paste, which can be viewed as sources of weakness. There is a direct inverse relationship between porosity and compressive strength (Figure 6-1).

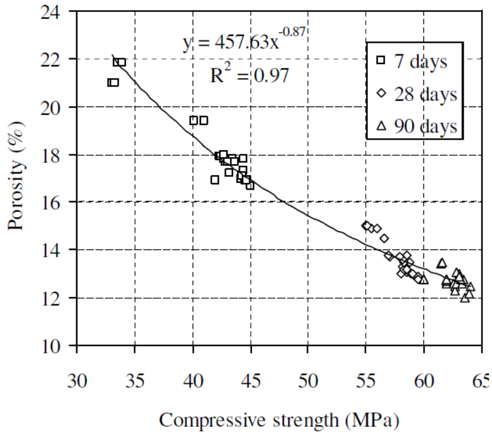

Figure 6-1. Relationship between porosity and compressive strength of Portland cement (Chindaprasirt and Rukzon 2008)

Other sources of weakness arise from the presence of aggregate which itself may contain flaws as well as causing micro-cracking at the interface with the hydrated cement paste. As aggregates represent three quarter of the total volume of concrete mortar, its properties such as size, shape and porosity can seriously influence the overall strength of cement. Aggregate particles contain pores that influence the strength of bonds formed at the interface of the aggregate and hydrated cement paste. It is understood that rougher textures or more angular shaped aggregates can result in a stronger bond leading to less micro-cracking at the interface. Larger aggregate particles are also known to require less water than finer aggregates during wetting when hydration occurs. This demand alters the effective water / cement ratio of the cement paste. A finer mix of aggregate can then decrease this ratio, subsequently decreasing the porosity while enhancing the strength.

6.3. Equipment and Materials

6.3.1. Ordinary Portland Cement (OPC)

The OPC used in tests is Type I and has the strength class 32.5 R.

6.3.2. Aggregate (Sand)

Pre-packed 1.35 kg BS EN 196-1 sand packs manufactured by David Ball Specialist Sands were used in these experiments. Each pack consists of more than 98% rounded silica particles with size ranging from 0.08 to 2 mm in diameter.

6.3.3. Mixer

A Kenwood Chef mixer was used for cement paste mixing. A plastic bowl of width 20 cm and height 18 cm and an approximate capacity of 5 litres are used. The stainless steel blade revolves about its own axis and is driven in a planetary movement around the axis of the bowl at various speeds (Table 6-2).

Table 6-2. Speed of mixer blade.

	Rotation /min	Planetary movement /min
Low speed	140 ± 5	62 ± 5
High speed	285 ± 10	125 ± 10

6.3.4. Vicat Apparatus

There are two apparatus that that can be used to determine the setting times; Vicat and Gilmore apparatus. Although both apparatus comprises of weights and needles, BS EN 196-3 prescribes the use of the Vicat apparatus as the method for determining setting times (BSI 2008). In the American standards, both methods are equally accepted as mentioned in ASTM C 191 (ASTM 2008) and ASTM C266 - 08e1 (ASTM 2009b) for Vicat needle and Gilmore needle respectively. However in these experiments the Vicat needle (Figure 6-2) has been designated as the apparatus of choice.

Figure 6-2. Vicat apparatus(CMT_Equipment 2012).

A schematic of the Vicat apparatus is given in Figure 6-3. It consists of a weight attached to moving parts with interchangeable ends. The total mass of the moving parts is 300 ± 1 g.

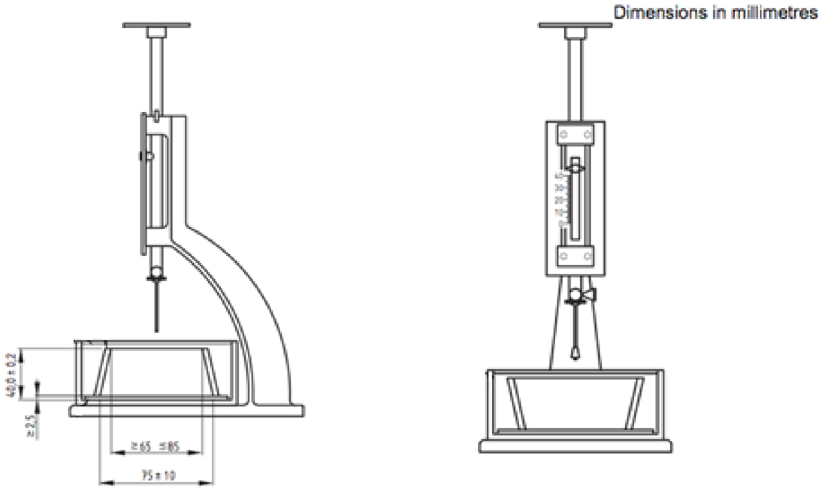

a) Side view with mould in upright position for initial setting time determination

b) Front view with mould inverted for final setting time determination

Figure 6-3. Schematic of the Vicat apparatus.

Schematics of the three interchangeable ends that can be attached to the moving parts are given in Figure 6-4. The plunger is made from steel in form of a right cylinder with 45 mm length and 10 mm diameter. The needle is also made from steel in the form of a right cylinder with 45 mm length and 1.13 mm diameter. The ring attachment has a diameter of approximately 5 mm.

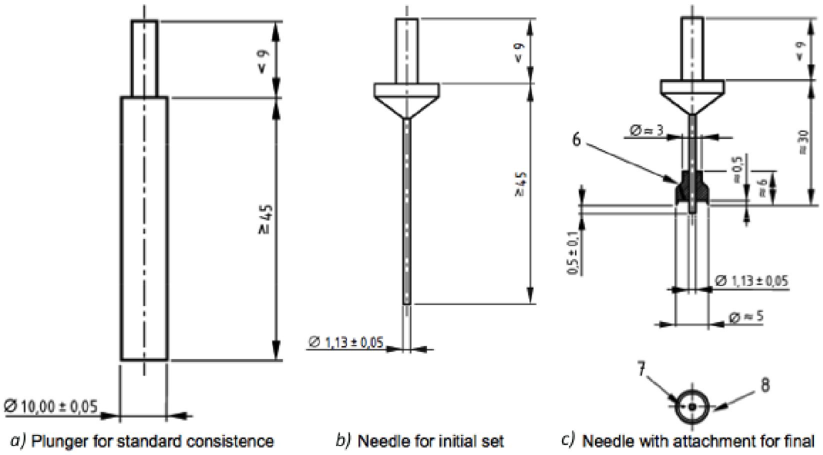

a) Plunger for standard consistence *b)* Needle for initial set *c)* Needle with attachment for final set

Figure 6-4. Needle attachment for Vicat apparatus.

6.3.5. Vicat mould

The Vicat mould is used to contain the cement paste during the standard consistence and setting time tests. It is made from plastic and shaped as a truncated cone with an internal diameter of 75 ± 10 mm and 40.0 ± 0.2 mm deep. The mould is paired with a base-plate, made from metal with a thickness of 2.5 mm.

6.3.6. Jolting Apparatus

The jolting apparatus used has been custom-built to comply with the specifications of BS EN 196-1 (BSI 2005).

6.3.7. Compressive Strength Tests

The EZ-50 Universal Materials Testing Machine from Lloyd Instruments was used to test the compressive strengths of the concrete samples. The EZ-50 machine is capable of testing applications of up to 50 kN and is suitable for non-continuous testing.

Prior to testing, the compressive strength testing gear is put in place. The de-moulded concrete sample is placed onto the machine and hard cardboard or plastic sheets are placed surrounding the test area to avoid release of test samples. As the test is running, data is gathered by the NEXYGENPlus Data Analysis software. Here, further data analysis on the stress, strain and load of the sample can be generated after tests are completed.

Table 6-3. Parameters used in the compressive strength tests.

Load Limit (kN)	40
Load rate (MPa / s)	0.6

6.4. Method development (Miniaturization of tests)

Miniaturization of standard consistency, setting times and compressive strength tests were carried out owing to the limited amount of sorbent produced in the cycling experiments. For descriptions of the operating procedures please refer to Appendix 6-1.

6.4.1. Standard Consistency

The standard consistency test was initially carried out using standard mould sizes according to the standard; the results indicated a required w / c ratio of 2.5. The sizes of moulds were then reduced and the standard consistency test repeated. The test utilized a plunger apparatus of diameter (10 ± 0.05) mm to penetrate the mould sample. Hence, it was decided that the minimum diameter of the miniaturized mould should not be any less than 26 mm to provide a minimum 8 mm of space from the plunger to the walls of the mould. The minimum mould diameter size available above 26 mm was found to be 31 mm. Upon miniaturization of the standard mould to a 31 mm diameter cylinder with a height of 40 mm, the w / c ratio required to pass the standard consistence test was found to have increased from 0.25 to 0.275.

6.4.2. Setting times

Setting times tests were then carried out with OPC using sample sizes set out in BS EN 196-3 (BSI 2008) to test the standard method. Next, moulds of smaller diameters were sourced or produced and each size was tested to see whether the same results could be achieved. The heights of each mould were kept at 40 mm to accommodate the operating specifications of the Vicat apparatus. Steel or plastic pipes were chosen as appropriate moulds given their availability and low cost. However, given that only standardized pipe sizes are manufactured, the range of pipe diameters available for use was limited. At this size, the setting times test using the Vicat apparatus matched the results of the standard tests. The final size of 31 mm still garnered initial and final setting times within the limits of the standard.

In the miniaturization process, mixing by hand was also attempted but the resulting cement paste was found to be greatly inconsistent and difficult to reproduce. Hence, the sizes of moulds were also limited to the minimum amount of cement paste that could be mixed with the standard mixing apparatus. This was found to be ~ 75g.

6.4.3. Compressive strength

OPC concrete prisms were first made according to BS EN 196-1 (BSI 2005) and tested for their compressive strength. However, it was later concluded that the prisms were too long to produce accurate testing results due to the need to miss out a flexural strength test. The flexural strength test was important to reduce the length of prisms to produce a prism with an appropriate length to width ratio suitable for compressive strength testing. The ratio most commonly used is 2:1. However, with a limited supply of spent sorbent available for making concrete, it was decided that a ratio of 1:1

would be more suitable as it required less material. This led to a redesign of the BS EN 196-1 standard mould to produce cubic concrete blocks. This was done in accordance with the guidelines stated in BS EN 12390-1:2000. The miniaturized mould produced cubic blocks measuring 40 x 40 x 40 mm.

The concrete blocks were then tested for their compressive strength and compared to the minimum required strengths as listed in BS EN 197. Further miniaturization of cubic moulds was attempted but due to limitations in design and time constraints, it was concluded that cylindrical moulds would be more suitable for miniaturization and testing. This also allowed a comparison between the compressive strengths of the different shapes of concrete samples to be made

Cylindrical moulds were produced using both steel and plastic drain pipes due to their availability and easy manipulation of length. The dimensions were decided in accordance with BS EN 12390-1:2000 and a length to diameter ratio of 2:1 was used. Cylindrical concrete blocks were made using several moulds of different diameter. The moulds were then attached to the jolting table's base plate with duct tape to keep the samples upright (Figure 6-5). This ensured a more consistent production of samples, particularly in attaining parallel top and bottom faces.

Figure 6-5. Miniaturised cylindrical moulds.

Each concrete sample was tested for its compressive strength. The strength of each block was shown to match or exceed the minimum strength required as listed in ASTM C150-04. Miniaturization of mould sizes was continued until a minimum size was found. The minimum size was determined when further miniaturization of mould size failed to match the required minimum strength. This was found to be 31mm. This miniaturization effectively decreased the amount of cement required for the test by 85 % from 500 to 75 g.

6.5. Results and Discussion

6.5.1. Standard Consistency

OPC cement paste tested for standard consistence, in standard mould sizes as according to BS EN 196-3 was found to utilize a w / c (water / cement) ratio of 0.25. This ratio was obtained by increasing the water content in 0.05 increments from a ratio of 0.2, while performing standard consistence tests on each specimen. As previously stated upon miniaturization of the standard mould to a 31 mm diameter cylinder with a height of 40 mm, the w / c ratio required to pass the standard consistence test was found to have increased from 0.25 to 0.275. Standard consistency testing was not carried out for cement produced with spent sorbent due to the limited amount of sorbent available. Instead, a w / c ratio of 0.275 was assumed for the setting times test.

Table 6-4.w / c ratios used in the fabrication of mortars.

Test type	w / c ratio
Standard test (OPC)	0.25
Miniaturised test (OPC)	0.275
Miniaturised test (cement from cycled sorbent	0.275

6.5.2. Setting times

Utilizing a w / c ratio of 0.275, the average initial setting time for OPC cement over 7 samples was found to be 134 minutes using the miniaturised moulds. The final setting time for the same number of samples was found to be 179 minutes. The initial and final setting times for cement produced with spent sorbent was found to be 75 and 240 minutes respectively. The cement used was made from single-cycle sorbent cycled in the absence of fuel. The setting times results are given in Figure 6-6 below.

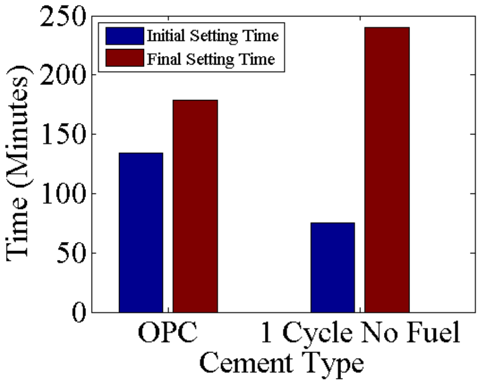

Figure 6-6. Setting times of OPC and cement produced from cycled sorbent (1 cycle, no fuel).

These results fall within the standard range where initial setting time is required to be above 60 minutes and final setting has to occur before 600 minutes as reported in BS EN 197-1.

The standard consistence and setting times of cycled-cement sorbent is found to fall within the required standards. This means that the concrete mix is sufficient in terms of workability and allows for full compaction which is vital in achieving the maximum possible density. As the strength of concrete is highly influenced by the presence of voids / porosity, a high density is preferred to produce cement of high quality and strength as described previously.

6.5.3. Compressive Strength

First the samples produced from OPC were tested for their compressive strength. Three 40 mm cubic samples were produced for both 3-day and 7-day testing along with four 31 mm cylindrical samples. The 3-day samples fractured and ultimately failed during testing. However, all 7-day test samples were able to withstand the maximum load of 40 kN as safely allowable by the compressive strength machine, and hence resisted total failure. As such there are no results to display for the 7-day test.

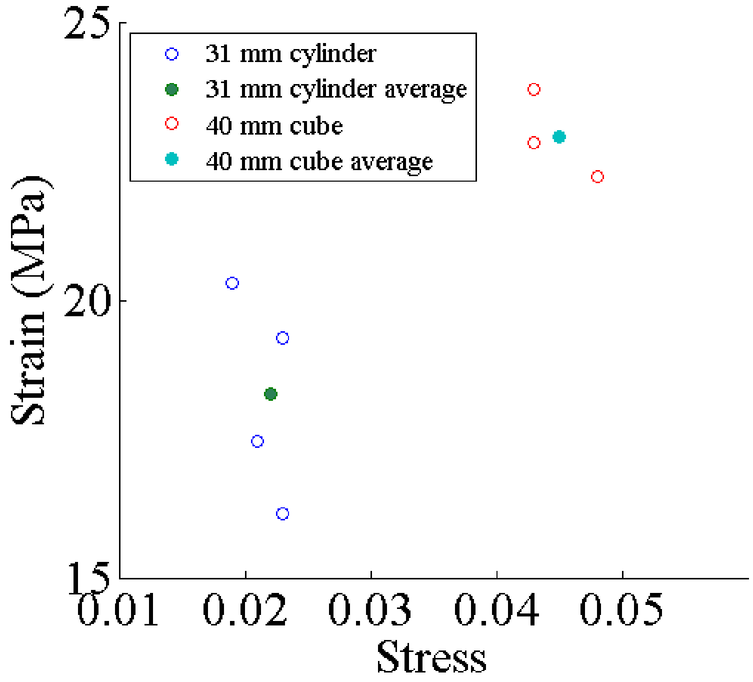

Figure 6-7. Results of the strength test for different shaped-samples (OPC, 3-day test)

The stress-strain behaviour of all samples were very similar (see Figure 6-7 and Figure 6-9, Appendix) and all samples were found to perform above the minimum required strength of 12 MPa as stated in the British Standard. (Figure 6-7). Notably, the cubic samples were found to have compressive strengths ~ 25 % higher than the cylindrical samples. However they also required 30 % more cement. Therefore the cylindrical moulds were chosen for testing of the cements produced from cycled sorbent due to the limited quantity of sorbent available.

For cylindrical samples at a height to diameter ratio of 2, the de-moulded samples were found to have uneven surface areas at the axial planes, with visible marks of uneven hydration, as shown in Figure 6-8. However this does not appear to have impacted on the strength of the cylinders produced, at least not to the extent that the cylinders failed before the minimum 12 MPa.

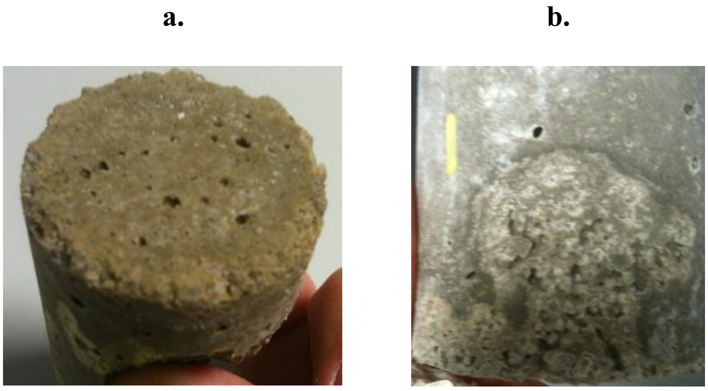

Figure 6-8. Images showing a) uneven finishing of top side of cylindrical samples b) visible marks of uneven hydration.

Next, the cement samples produced from cycled sorbent were tested. Due to the limited quantity of sorbent, compressive strength tests were only conducted on 5-cycled sorbent cement with fuel, whilst it was possible to perform the test on no fuel sorbent-cements up to 15 cycles. Physical inspection showed that the produced cement samples were also found to have uneven surface area due to poor finishing and visible marks of uneven hydration as seen in Figure 6-8.

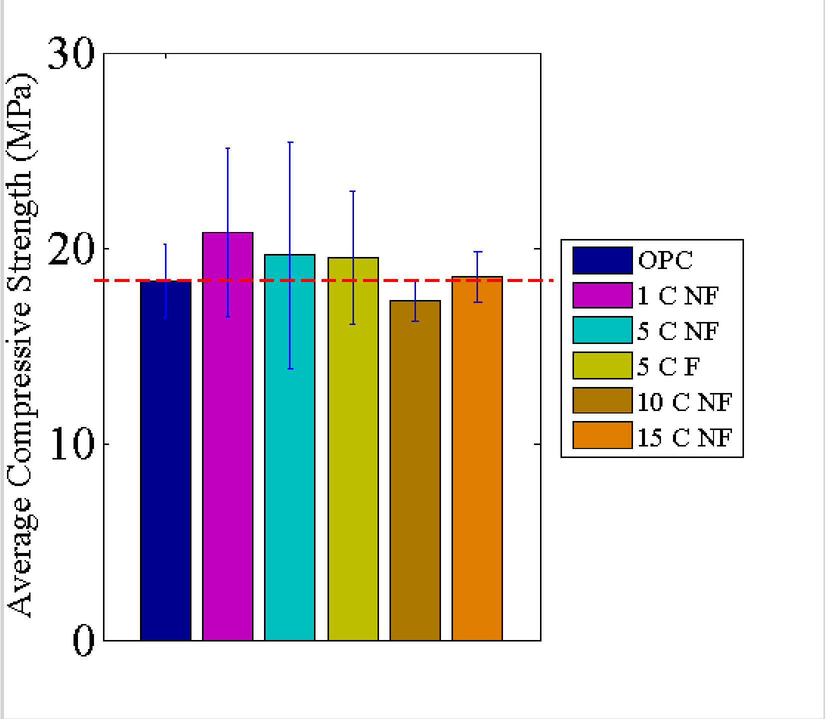

Figure 6-9. Average compressive strengths for different cycled-sorbent cement. OPC=Ordinary Portland Cement; 1C NF= 1 cycle, no fuel; 5C NF=5 cycle, no fuel; 10C NF. Average of 3 samples with error bars shown as the standard deviation. Red dotted line enables comparison with OPC.

Figure 6-9 illustrates the average compressive strengths of each cycled-cement in comparison with the OPC. It shows that all samples tested clearly passed the minimum strength requirement of 12 MPa for the 3-day test as stated in ASTM C150-04a. It can also be observed that all cycled-sorbent cement performed better than OPC with the exception of 10-cycled sorbent. On average, cement from cycled sorbent result in a compressive strength value 4.7 % higher than OPC. The standard deviation for each cement type was calculated, and was found to vary between 1.0 and 5.8.

The cement produced from 5-cycle sorbent with fuel was found to differ from 5-cycle cement produced from sorbent without fuel by only 0.2 MPa. This represents a difference of only 1%. As such it is reasonable to assume that the introduction of additional fuel impurities into the cement did not have an impact on the strength of the cement. However, further testing would be required to draw a firm conclusion given the limited number of samples run so far.

Figure 6-10 and Figure 6-11 (Appendix 6-1) allow comparison of the deformation and strength characteristics of OPC and cement from cycled sorbent to be made. It shows that OPC and cycled-sorbent cement have similar non-linear stress-strain behaviours. All specimen curves start with an upwards slope that is followed by a linear ramp-up which is more steep. A loss of linearity is then observed before the peak or maximum load is reached. This loss of linearity can be understood to be an indication of the initiation of the fracture process within the test sample.

Generally speaking, it can be seen that there exists a downward trend in sample strength as the number of cycles increase. A study by Blamey et al. (Blamey, Anthony et al. 2010) discovered that repeated cycling of sorbent causes higher degrees of CaO particle sintering, or changes in pore shape and shrinkage. This is thought to decrease the rate of hydration of samples as water encounters more resistance while filling up the pores. This is turn would hamper the hydration reactions and build-up of solid hydration products. Subsequently, this could affect the degree of hydration which is a main indicator of porosity and overall strength. As such, this could explain why higher numbers of cycles lead to a decrease in the cement strengths recorded.

6.6. Conclusions

- Successful new methods involving miniaturised test specimens have been developed, allowing comparative studies of setting times and compressive strength tests to be conducted for OPC and sorbent-cycled cements. Only 75 g of cement are now required to produce one sample for setting time and compressive strength tests using a mould size of diameter 31 mm.

- Hand mixing of this small amount of mortar was unsuccessful therefore the procedure still depends on the use of the automated mixer.

- Standard water / cement ratio of the miniaturised OPC sample was found to be 0.275.

- The initial and final setting times of 1-cycled sorbent sample was found to be 75 and 240 minutes respectively which fell within the standard range recorded in BS EN 197-1.

- Cubic samples have been shown to be 25 % stronger than their cylindrical equivalent following miniaturisation.

- Compressive strength conducted on all sample specimens passed the minimum required strength as stated in the ASTM C150-04a. Cements made from cycled sorbent were found on average to be 4.7% higher in compressive strength than OPC.

- Due to the small number of test sample size conducted, these initial results provide indications; future work should include a higher number of test samples.

6.7. Limitations of the experimental method

- Rudimentary Equipment. The miniaturisation tests required certain modifications to the standard methods and procedures to be made. The tests were carried out using rudimentary equipment, as deemed reasonable for a preliminary study. Further work would enable the miniaturisation tests to be carried out using materials of a more suitable nature.

- Moulding / De-moulding of specimens. The moulding of specimens can be said to be one of the factors leading to the inconsistent quality of samples. In the compaction of specimens during moulding, the influence of uneven and non-uniform compaction across the entire sample was apparent once demoulding of the sample was carried out. This irregular compaction could have been caused by a design flaw in which the base plate of the jolting table was not horizontal when rested on the stop during the jolting process. Although this flaw is minimal in practical sense, the quality of compaction that could be provided is clearly affected.

- Miniaturisation leading to wall effects. Another factor that has contributed to the quality of samples is the uneven finishing at the top surface. It was observed that as the size of the moulds decreased, wall effects became more apparent and finishing of samples was less perfect. In certain cases, the top surface was elliptical when demoulded.

- Limited number of specimens. Production of test specimens was severely limited due to the availability of cycled sorbent. In most cases, only 3 samples of each specimen batch were available for testing. This small sample size, although able to provide some initial trends, cannot be used to draw firm conclusions at this stage.

6.8. Further Work

- The number of test samples should be increased to enable results that would be of statistical significance.

- Compressive stress tests should be carried out for 28 days samples to utilize available literature information for comparison.

- Specimens should be capped or grinded to provide greater consistency in the shape of samples.

- Further studies in water / cement ratio, flexural strength and degree of hydration should be performed.

Chapter 7. Conclusions and Further Work

7.1 Conclusions

The Ca-Looping system has been modeled using a stochastic population balance model, a method which is able to garner similar results for the age distribution (r_N), the maximum average reactivity of the sorbent ($\overline{x}_c$) and the CO_2 capture efficiency of the carbonator (E_{CO2}) as those published in literature by INCAR. This method has been furthered to run on a time basis as opposed to per cycle and to incorporate the carbonation rate and extent of carbonation from experimental data rather than a simplified kinetic model. However this part of the model requires further work to bring the results for E_{CO2} closer to those published in literature. A generic dry-process cement plant mass and energy balance has been developed which resulted in a figure of 4.34 MJ for the thermal efficiency of producing 1 kg of clinker. This is within the top 90th percentile of kilns globally; it is thought that this lower thermal efficiency is due to the size the tertiary air stream. Integration of the Ca-looping process with the cement plant indicates that the thermal efficiency of producing 1 kg of clinker can range from 4.49 – 5.83 MJ depending on whether the system supplies itself with electricity through waste heat recovery or whether electricity is supplied from the grid. Up to ~ 36 MW electricity may also be passed back to the grid, however this results in the lowest thermal efficiency of producing 1 kg of clinker of 5.83 MJ. For all configurations 92 % of all CO_2 produced at the kiln is captured which equates to ~ 0.12 kg / kg of clinker or 126 mols^{-1}.

A laboratory-scale system has been designed, built and commissioned capable of producing spent sorbent following a given number of cycles of calcination and carbonation. A range of fuel feeding systems have been tested and included in the commissioning process. The mass balance on the first cycle indicate that the limestone is fully calcined.

The results of the single cycle experiments indicate that Sr is easier to extract from $CaCO_3$ than from $Ca(OH)_2$, whilst Ba and Mn were both easier to extract from $Ca(OH)_2$ than from $CaCO_3$. The results of these experiments also suggest that Cr contamination from the thermocouple is a strong possibility though well below any limit likely to impact on clinker composition. Sorbent cycled in the absence of fuel does not undergo a measurable change in its trace element inventory up to fifteen cycles. The fuel systems designed and built as part of this project are effective in introducing the fuel into the system and in enabling the ash to mix with the sorbent during combustion as indicated by the concentrations for Al in the sorbent cycled with fuel. The decrease in the % retention for Al and other elements with reasonable RSD values suggest that an equilibrium is reached for the amount of ash entering the system after a certain number of cycles. The results show that B would need further observation given its observed increase over eight cycles and its known role in the formation of alite crystals. The results for Na indicate that this element could have implications in terms of volatile cycles developing both in the Ca-looping calciner and the cement kiln. Such features of the system could limit the amount of sorbent that can be passed directly to a cement kiln.

Methods have been developed to enable clinker to be produced in the laboratory with a % wt of alite comparable to commercial clinkers. Methods have been developed to enable the intensity of X-ray diffraction peaks to be converted to wt % alite. Clinkers produced from sorbent repeatedly cycled in the absence of fuel did not lead to a change in the % wt alite, nor did cycling in the presence of continuously fed coal nor semi-continuously fed RDF. However, repeated cycling in the presence of 2 g of La Jagua did appear to effect a % wt change in alite over the course of fiftten cycles. This is potentially due to the incorporation of impurities from the fuel in the sorbent.

Successful new methods involving miniaturised test specimens have been developed, allowing comparative studies of setting times and compressive strength tests to be conducted for OPC and sorbent-cycled cements. Only 75 of cement are now required to produce one sample for setting time and compressive strength tests using a mould size of diameter 31 mm. Hand mixing of this small amount of mortar was unsuccessful therefore the procedure still depends on the use of the automated mixer. Standard water / cement ratio of the miniaturised OPC sample was found to be 0.275. The initial and final setting times of 1-cycled sorbent sample was found to be 75 and 240 minutes respectively which fell within the standard range recorded in BS EN 197-1. Cubic samples have been shown to be 25 % stronger than their cylindrical equivalent following miniaturisation. Compressive strength conducted on all sample specimens passed the minimum required strength as stated in the ASTM C150-04a. Cements made from cycled sorbent were found on average to be 4.7% higher in compressive strength than OPC. Due to the small number of test sample size conducted, these initial results provide indications; future work should include a higher number of test samples.

7.2 Further Work

- The stochastic model requires further work to bring the results for E_{CO2} closer to those published in literature.

- Incorporation of the effects of sulphation and ash need to be included into the stochastic model.

- Further development of the fluidised bed heating system would ensure the entire calcination step takes place at 900 °C.

- Further work would include to ascertain why when digesting NIST SRM 1d (argillaceous limestone) experimental values for Na and K were much higher than the certified values.

- Further work would include producing and testing sorbent with a wider range of solid fuels to see which other elements may be of interest in terms of their retention in the sorbent and their behaviour under calcination / carbonation conditions.

- Larger numbers of clinker samples are required to enable definitive conclusions to be drawn with regards to the change in % wt. alite, in particular for the result with 2 g La Jagua per cycle.

- The number of performance test samples should be increased to enable results that would be of statistical significance.

- Compressive stress tests should be carried out for 28 days samples to utilize available literature information for comparison.

- Performance test specimens should be capped or grinded to provide greater consistency in the shape of samples.

- For the performance tests, further studies in water / cement ratio, flexural strength and degree of hydration should be performed.

Appendix 2-1. Matlab code for the steady-state stochastic model

```
function [CcHrat_x, CcHrat_s, xave, xcarb] = model(F0_mfr)

%% INITIATE RETURN VARIABLES

CcHrat_x        = [];
CcHrat_s        = [];
CcHin_s         = [];
xave            = [];
xcarb           = [];
XCyc            = [];
FRs             = [];

%% MODEL PARAMETERS

no_cyc          = 10000;
Eff             = 0.7;
FCO2            = 1;
CaO_pp          = 1/1000;
no_p_init       = 1/CaO_pp;

% HBr-doped 13 cycles
% Xr=0.1264;
% a=1.6238;

% Grasa
% Xr=0.2182;
% a=0.8574;

% Grasa
Xr=0.075
a= 0.52

% Undoped 50 cycles
% Xr=0.0454;
% a=0.7212;

% HBr-doped 50 cycles
% Xr=0.1264;
% a=0.6956;

%% HEAT VALUES

% enth_Cp = NASA_Glenn;
% enth = enth_Cp(:,:,1) %kJ/mole
% Cp = enth_Cp(:,:,2) %kJ/mole/K
% For_Heat_Reaction
% Rev_Heat_Reaction

% Cp_CaCO3_1223_298 = ((((19.68*(1223-298)) + ((0.01189/2)*(1223^2-298^2))
+ (307600*((1/1223)-1/298))))*(1223-298))*(4.184/1000);
% Cp_CaCO3_1223_923 = ((((19.68*(1223-923)) + ((0.01189/2)*(1223^2-923^2))
+ (307600*((1/1223)-1/923)))*(1223-923))*(4.184/1000));
% Cp_CaO_1223_923 = ((((10*(1223-923)) + ((0.00484/2)*(1223^2-923^2)) +
(108000*((1/1223)-1/923)))*(1223-923))*(4.184/1000));
```

```
% Cp_CaCO3_1223 = (((19.68*1223) + ((0.01189/2)*1223^2) +
(307600*(1/1223)))*1223)*(4.184/1000);
% Cp_CaCO3_923 = (((19.68*923) + ((0.01189/2)*923^2) +
(307600*(1/923)))*923)*(4.184/1000);
% Cp_CaCO3_298 = (((19.68*298) + ((0.01189/2)*298^2) +
(307600*(1/298)))*298)*(4.184/1000);
%
% Cp_CaO_1223 = (((10*1223) + ((0.00484/2)*1223^2) +
(108000*(1/1223)))*1223)*(4.184/1000);
% Cp_CaO_923 = (((10*923) + ((0.00484/2)*923^2) +
(108000*(1/923)))*923)*(4.184/1000);

deltaHf_CaCO3_1223=-1100.89;
deltaHf_CaCO3_923=-1138.92;

deltaHf_CaCO3_298=-1206.61;

deltaHf_CaO_1223=-588.805;
deltaHf_CaO_923=-604.21;

Rev_Hr = 168.5; % kJ/mol
Hcomb = (34*(12/0.83))*1000; % kJ

Hr_Cb = -168.5; % kJ/mol
Hr_Cc = 168.5; % kJ/mol
Hcomb = 34*(12/0.83); %kJ/mol

Hr_Hy = -109; % kJ/mol
Hr_DHy = 109; % kJ/mol
Cp_CaOOH2 = 21.4*4.184/1000;

%% Decay Curves Derived from Experimental Work

% % Decay Curve NF1 - Precipitated CaCO3 (PCC3, tp 3hr, 900C, N2)
% DC_NF1 =
[[[0.381017319000000,0.372740437000000,0.364790974000000,0.356523179000000,
0.347612914000000,0.338938937000000,0.330395474000000,0.322242794000000,0.3
14820686000000,0.307534899000000,0.301018814000000,0.294772591000000,0.2890
20149000000,0.283286135000000,0.278055242000000,0.273063666000000,0.2684416
68000000,0.263977448000000,0.259946674000000,0.255894694000000,0.2522607630
00000,0.248702816000000,0.245341776000000,0.242144320000000,0.2390468320000
00,0.236137414000000,0.233476402000000,0.230660893000000,0.228033456000000,
0.225666288000000]],[linspace(0.225666288000000,0.2,no_cyc-30)]];
%
% % Decay Curve NF2 - Precipitated CaCO3 (PCC16, tp 3hr, 900C, N2)
% DC_NF2 =
[[[0.357403152000000,0.347885982000000,0.337705663000000,0.327433991000000,
0.317446698000000,0.308009653000000,0.298915259000000,0.290418154000000,0.2
82420308000000,0.274655550000000,0.267499614000000,0.260959177000000,0.2547
31953000000,0.248719911000000,0.243655397000000,0.238648852000000,0.2337664
39000000,0.229175386000000,0.224948837000000,0.221476488000000,0.2175922880
00000,0.214090498000000,0.210683705000000,0.207674193000000,0.2046425260000
00,0.202066414000000,0.199497889000000,0.197012826000000,0.194549616000000,
0.192549244000000]],[linspace(0.192549244000000,0.185,no_cyc-30)]];
%
% % Decay Curve NF3 - Precipitated CaCO3 (PCC16 'Average Data', 15% CO2
constant
```

```
% DC_NF3 =
[[[[0.428515625000000,0.363501439000000,0.330254898000000,0.313230989000000
,0.304289844000000,0.298452259000000,0.293200762000000,0.287717424000000,0.
281930435000000,0.275723404000000,0.269637282000000,0.263434758000000,0.257
539380000000,0.251919856000000,0.246416143000000,0.241304319000000,0.236380
211000000,0.231539449000000,0.227094017000000,0.222995748000000,0.218904741
000000,0.215104537000000,0.211526487000000,0.208085461000000,0.204758872000
000,0.201642910000000,0.198480362000000,0.195349262000000,0.192430211000000
,0.189567573000000]]],[linspace(0.189567573000000,0.15,no_cyc-30)]];
%
% % Decay Curve NF4 - Precipitated CaCO3 (PCC16 'Average Data', 50% CO2
constant)
% DC_NF4 =
[[0.410432210000000,0.397836621000000,0.382362341000000,0.367062136000000,0
.353302005000000,0.340903570000000,0.329768645000000,0.319751711000000,0.31
0593807000000,0.302342266000000,0.294884819000000,0.287793125000000,0.28133
1231000000,0.275150986000000,0.269473015000000,0.264138108000000,0.25909893
4000000,0.254341408000000,0.249762652000000,0.245503098000000,0.24148803100
0000,0.237674422000000,0.234025499000000,0.230559649000000,0.22721115200000
0,0.224139610000000,0.221185814000000,0.218551220000000,0.215808660000000,0
.213155289000000],[linspace(0.213155289000000,0.2,no_cyc-30)]];
%
% % Decay Curve NF5 - Precipitated CaCO3 (PCC16 'Average Data', 50% CO2
constant)
% DC_NF5 =
[[[0.472195292000000,0.446153579000000,0.429463322000000,0.416460146000000,
0.405331780000000,0.395367066000000,0.386290971000000,0.377784588000000,0.3
69710727000000,0.362190862000000,0.354918854000000,0.348016503000000,0.3413
88859000000,0.334989753000000,0.328786773000000,0.322780572000000,0.3169943
98000000,0.311385031000000,0.305858174000000,0.300555600000000,0.2953312790
00000,0.290295880000000,0.285433686000000,0.280661533000000,0.2760979470000
00,0.271734742000000,0.267591564000000,0.263208714000000,0.259195194000000,
0.255256653000000]],[linspace(0.255256653000000,0.22,no_cyc-30)]];
%
% % Decay Curve NF6 - Precipitated CaCO3 (PCC16 'Average Data', 15% CO2
carb, 100% N2 calc)
DC_NF6 =
[[0.482700781000000,0.470601391000000,0.453828698000000,0.438135703000000,0
.424121977000000,0.412051138000000,0.401179913000000,0.391262287000000,0.38
2218794000000,0.374055620000000,0.366040435000000,0.358356916000000,0.35151
2792000000,0.344657725000000,0.338059139000000,0.331552393000000,0.32530831
4000000,0.319401136000000,0.313620057000000,0.307844213000000,0.30242858600
0000,0.296921596000000,0.291774347000000,0.286701331000000,0.28192571900000
0,0.277218154000000,0.272773733000000,0.268517747000000,0.264467329000000,0
.260582505000000],linspace(0.260582505000000,0.23,no_cyc-30)];
%
% % Decay Curve NF7 - Precipitated CaCO3 (PCC16 'Average Data', 50% CO2
carb, 100% N2 calc)
% DC_NF7 =
[[0.472195292000000,0.446153579000000,0.429463322000000,0.416460146000000,0
.405331780000000,0.395367066000000,0.386290971000000,0.377784588000000,0.36
9710727000000,0.362190862000000,0.354918854000000,0.348016503000000,0.34138
8859000000,0.334989753000000,0.328786773000000,0.322780572000000,0.31699439
8000000,0.311385031000000,0.305858174000000,0.300555600000000,0.29533127900
0000,0.290295880000000,0.285433686000000,0.280661533000000,0.27609794700000
0,0.271734742000000,0.267591564000000,0.263208714000000,0.259195194000000,0
.255256653000000],linspace(0.255256653000000,0.23,no_cyc-30)];

% % Decay Curve VM1 - Pre-sintered Sorbent @ 900C - Manovic & Anthony 2008
- Figure 3
```

```
% DC_VM1 = [[0.65 0.71 0.738 0.754 0.762 0.762 0.75 0.741 0.7238 0.7512 0.7
0.6848 0.6349 0.6463 0.6377 0.6197 0.605 0.5186 0.5673 0.553 0.5337 0.5194
0.509 0.49 0.481 0.475 0.463 0.452 0.444
0.4358],linspace(0.4358,0.35,no_cyc-30)];
%
% % Decay Curve VM2 - Pre-sintered Sorbent @ 900C - Manovic & Anthony 2008
- Figure 3
% DC_VM2 = [[0.65 0.71 0.738 0.754 0.762 0.762 0.75 0.741 0.7238 0.7512 0.7
0.6848 0.6349 0.6463 0.6377 0.6197 0.605 0.5186 0.5673 0.553 0.5337 0.5194
0.509 0.49 0.481 0.475 0.463 0.452 0.444
0.4358],linspace(0.4358,0.35,no_cyc-30)];


%% LOOP THROUGH INPUTS

for F0set=1:length(F0_mfr)
for p=1:length(F0_mfr{F0set}(1,1:end))
                F0 = F0_mfr{F0set}(p);
                age = ones(1,no_p_init);
                [CcHrat_s, xave, XCyc, age, FRs]=stoch(F0, CcHrat_s, xave,
XCyc, age, FRs);
if F0set==1
                [CcHrat_x, xcarb]=Heat_Req_xcarb(CcHrat_x, F0, xcarb);
end
end
end

%% FUNCTIONS

function [CcHrat_s, xave, XCyc, age, FRs] = stoch(F0, CcHrat_s, xave, XCyc,
age, FRs)

for c=1:no_cyc
            clear p_react

%                 p_react                 = ((1*(((1/(1-
Xr))+(a*(age))))).^-1)+Xr;
            p_react                 = DC_NF6(age);

            XCyc{F0set}(c,p)        = mean(p_react);
            FRCyc{F0set}(c,p)       = Eff/XCyc{F0set}(c,p);
            no_p_sys                = FRCyc{F0set}(c,p)/CaO_pp;

            age(1,:)                = age(1,:)+1;

            [chosen]                = purge_func(age,F0,c,FRCyc);
            age                     =
[[age],[ones(1,round(((F0/CaO_pp)+(no_p_sys-length(age)))))]];
            age                     = age(setdiff(1:length(age),chosen));

end

xave{F0set}(p)           = mean(XCyc{F0set}(no_cyc-100:no_cyc,p));
FRs{F0set}(p)            = Eff/xave{F0set}(p);
CcHin_s{F0set}(p)        =
(Rev_Hr*((FRs{F0set}(p)*xave{F0set}(p))+F0))+(((FRs{F0set}(p)*(1-
xave{F0set}(p))*(deltaHf_CaO_1223-
```

```
deltaHf_CaO_923))+(FRs{F0set}(p)*(xave{F0set}(p))*(deltaHf_CaCO3_1223-
deltaHf_CaCO3_923))))+(F0*(deltaHf_CaCO3_1223-deltaHf_CaCO3_298));
CcHrat_s{F0set}(p)        =
(CcHin_s{F0set}(p)/(CcHin_s{F0set}(p)+Hcomb))*100;
end

kk=CcHrat_s(ECRA);
find(kk==min(kk));

save 20130418_results_grasa

function [chosen] = purge_func(age,F0,c,FRCyc)

    purgesize    = floor(F0/CaO_pp);                      % No. of particles
to purge
    chosen=[];
    counter=0;
if purgesize>0
while length(chosen) ~= purgesize
    chosen=unique([chosen;ceil(rand(counter,1)*(length(age)+purgesize))]);
    counter=purgesize-length(chosen);
end
end
end

function [CcHrat_x, xcarb]=Heat_Req_xcarb(CcHrat_x, F0, xcarb)

    xcarb(p,:)                           = linspace(1E-
10,xave{F0set}(p),50);
for x=1:length(xcarb)
    x_carb                               = xcarb(p,x);
    FRx                                  = (FCO2*Eff)/x_carb;
    CcHin_x(p,x)                         =
(Rev_Hr*((FRx*x_carb)+F0))+(((FRx*(1-x_carb)*(deltaHf_CaO_1223-
deltaHf_CaO_923))+(FRx*(x_carb)*(deltaHf_CaCO3_1223-
deltaHf_CaCO3_923))))+(F0*(deltaHf_CaCO3_1223-deltaHf_CaCO3_298));
    CcHrat_x(p,x)                        =
(CcHin_x(p,x)/(CcHin_x(p,x)+Hcomb))*100;
end
end

end
```

Appendix 2-2. Matlab code for the time-dependent stochastic model

```
function [Ecarb] = model_V_FBData_10s

close all
clear all

MCaCO3 = 100.04;

%% Loading FB Data

% FB DATA
% convdatFB = load('LC_30cycles_nosteam_r_per_second.mat');
% [dconv1 dconv2] = size(convdatFB.convdatFBpersecond)
% convdatFBextent = load('LC_30cycles_nosteam.mat');
% convdatFB = load('LC_30cycles_nosteam.mat','conversion');
% convdatFB.conversion(400:501,23)=convdatFB.conversion(399,23)
% convdatFB.conversion(399:501,24)=convdatFB.conversion(398,24)
% convdatFB.conversion(500:535,:)=[];
tb=1;

% TGA DATA
ext_conv = xlsread('G:\backup 20120910\Work\4 Lab Work\2 Cycling
Experiments\Others\NF\TGA_NF_CONVDATA_HAVELOCK','Sheet1');
ext_conv(701:730,:)=[];
% ext_conv = convdatFBextent;
% conv_per_s = convdatFB.conversion;

% t_star=[20];
% k=0.52;
% Xr=0.075;
%
% for N=1:100
%     conversion_grasa(N)=(1/((1/(1-Xr))+(k*N)))+Xr;
%     ext_convrev(N,:)=linspace(conversion_grasa(N),0,t_star)
% end
%
% ext_conv=fliplr(ext_convrev)
%
% for N=1:100
% for t=t_star:(730-t_star)
%     ext_conv(N,t)=conversion_grasa(N);
% end
% end
% ext_conv=transpose(ext_conv);
%
%
[dconv1 dconv2] = size(ext_conv);
pos=floor(linspace(1,dconv1,(dconv1/tb)));
for l=1:dconv2
    ext_conv_10s(:,l) = ext_conv(pos,l);
end
[dconv3 dconv4] = size(ext_conv_10s);
for i=2:dconv3
        conv_per_s(i,:) = ext_conv_10s(i,:)-ext_conv_10s((i-1),:);
end
conv_per_s(1,:) = ext_conv_10s(1,:);
```

```
for k=1:dconv4
for j=1:dconv3
if conv_per_s(j,k)<0
    conv_per_s(j,k)=0;
end
end
end

% plot(

%% Particles
dp = 500/1e6;   % Particle Diameter in Metres
ro = 2500;       % Particle Density (kg/m3)

%% MODEL PARAMETERS

deltaHf_CaCO3_1223=-1100.89;
deltaHf_CaCO3_923=-1138.92;

deltaHf_CaCO3_298=-1206.61;

deltaHf_CaO_1223=-588.805;
deltaHf_CaO_923=-604.21;

% Fuel Properties - La Jagua
FuelA(1)=0.02; % Ash
FuelA(2)=0.83; % Carbon
FuelA(3)=0.01; % Sulphur
FuelA_LHV=32; % MJ/kg

% Power Plant Operation
MW               = 1000;
eff              = 0.44;
Ffuel1           = (MW/FuelA_LHV)*(1/eff);
FCO2             = (Ffuel1*FuelA(2))/12; % CO2 to carbonator (kmols-1) % for
the cement plant use: 0.14;
Hcomb = FuelA_LHV*(12/FuelA(2))*FCO2; % Total Energy Input to Power Plant
(MW)
FCO2=FCO2*tb;
FCO2run(1:144000,1)=FCO2;
% FCO2run(30000:36000,1)=FCO2*1.25;
% FCO2run(36000:42000,1)=FCO2;

% Ca Loop Calciner Operation with Climafuel
FuelB(1)        =0.01; % Ash
FuelB(2)        =0.8; % Carbon
FuelB(3)        =0.01; % Sulphur
FuelB_LHV       = 18; % MJ/kg
Ffuel2          = (Ffuel1*0.5*(FuelA_LHV/FuelB_LHV))*tb; % kgs-1
Fash            = Ffuel2*FuelB(1); % kgs-1
FS              = (Ffuel2*FuelB(3))/32; % kmols-1

% Cement Plant
CaORequiredpersecond = 4000*1000*0.65/24/60/60/56;

% Model Parameters
no_seconds      = 36000;                             % simulation length
(e.g. run for one hour)
```

```
FR                = FCO2*[1];                          % Ca entering leaving
Cb (kmols-1)
F0                = FCO2*[0.01];                       % Ca entering Cc fresh
(kmols-1) % for the cement plant use: 0.55;
CaO_pp            = 0.1;                              % CaO per packet(kmol)
WCaO              = (50*MW);                          % Solids inventory (each
unit), CaO (kg)
pkts_pu           = ((WCaO/56)/CaO_pp);                % Packets per unit
(moles)
ash_perpkt        = Fash/pkts_pu;
S_perpkt          = FS/pkts_pu;

% Heat Values: Perry's - kJ
Cp_CaCO3_1223_298 = (((((19.68*(1223-298)) + ((0.01189/2)*(1223^2-298^2)) +
(307600*((1/1223)-1/298))) *4.184/1000)/(1223-298)));
Cp_CaCO3_1223_923 = (((((19.68*(1223-923)) + ((0.01189/2)*(1223^2-923^2)) +
(307600*((1/1223)-1/923))) *4.184/1000)/(1223-923)));
Cp_CaO_1223_923 = (((((10*(1223-923)) + ((0.00484/2)*(1223^2-923^2)) +
(108000*((1/1223)-1/923))) *4.184/1000)/(1223-923)));
Cp_CaO_1223_573 = (((((10*(1223-573)) + ((0.00484/2)*(1223^2-573^2)) +
(108000*((1/1223)-1/573))) *4.184/1000)/(1223-573)));
% CpCaSO4=
Hr_Cb = -168.5; % MJ/kmol
Hr_Cc = 168.5; % MJ/kmol
CalcT = 950;
CarbT = 650;

% packet data matrix
% 1 Residence Time
% 2 Age
% 3 CO2 Uptake per Second (s-1)
% 4 Total Conversion
% 5 Ash
% 6 Sulphur
count = 0;
%% RUN SIMULATION

for r=1:length(FR)
    clear pdatCbpdatCc
    FR_=FR(r);
    packetsFR       = round((FR_)/CaO_pp); % No. of particles to pass to
calciner
for p=1:length(F0)
    clear pdatCbpdatCc
    pdatCb          = zeros(6,pkts_pu);
    pdatCc          = zeros(6,pkts_pu);
    pdatCb(1,:)     = 1;
    pdatCc(1,:)     = 1;
    pdatCb(2,:)     = 1;
    pdatCc(2,:)     = 1;

    F0_=F0(p);
    packetsF0       = ceil((F0_)/CaO_pp); % No. of particles to purge from
calciner
    freshstream     = zeros(6,packetsF0);
    freshstream(1,:)= ones;
    freshstream(2,:)= ones;

for s=1:no_seconds
```

```
    count=count+1
    pdatCb(3,:)=0;
% Length of time in current unit (s)
    pdatCb(1,:) = pdatCb(1,:)+1;
    pdatCc(1,:) = pdatCc(1,:)+1;

% CO2 uptake capacity per packet per second
% & Total conversion per packet
for iv=1:length(pdatCb)
if pdatCb(1,iv)<dconv3 && pdatCb(2,iv)<dconv4;
            pdatCb(3,iv) = (conv_per_s(pdatCb(1,iv),pdatCb(2,iv)))*CaO_pp;
            pdatCb(4,iv) =
(ext_conv_10s(pdatCb(1,iv),pdatCb(2,iv)))*CaO_pp;
elseif pdatCb(1,iv)>=dconv3 && pdatCb(2,iv)<dconv4;
            pdatCb(3,iv) = (conv_per_s(dconv3,pdatCb(2,iv)))*CaO_pp;
            pdatCb(4,iv) = (ext_conv_10s(dconv3,pdatCb(2,iv)))*CaO_pp;
elseif pdatCb(1,iv)<dconv3 && pdatCb(2,iv)>=dconv4;
            pdatCb(3,iv) = (conv_per_s(pdatCb(1,iv),dconv4))*CaO_pp;
            pdatCb(4,iv) = (ext_conv_10s(pdatCb(1,iv),dconv4))*CaO_pp;
end
end

% Ecb
   CO2reacting(s)=sum(pdatCb(3,:));
   Ecarb(s,r,p) = CO2reacting(s)/FCO2run(s);
if Ecarb(s,r,p) > 0.92
       Ecarb(s,r,p) = 0.92;
end

% Ash and Sulphur
        pdatCc(5,:)             = pdatCc(5,:)+ash_perpkt;
        pdatCc(6,:)             = pdatCc(6,:)+S_perpkt;

% Moving Packets around system

        [chosen1]               = stoch_func1(pkts_pu,packetsFR);       %
function: pass packets from Cb to Cc
        pdatCb(1,chosen1)       = 0;                                    %
reset residence time to zero
        pdatCc                  =[[pdatCc],[pdatCb(:,chosen1)]];        %
append Cb matrix with Cc packets
        FRdata                 =[pdatCb(:,chosen1)];
        pdatCb(:,chosen1)       =[];                                    %
delete packets from Cb matrix

        [chosen2]               = stoch_func2(pkts_pu,packetsFR);       %
function: add packets from Cc to Cb
        pdatCc(1,chosen2)       = 0;                                    %
reset residence time to zero
        pdatCc(2,chosen2)       = pdatCc(2,chosen2)+1;                   %
increase age of calcined particles by one
        pdatCb                  = [[pdatCb],[pdatCc(:,chosen2)]];        %
append Cc matrix with Cb packets
        pdatCc(:,chosen2)       = [];                                    %
delete packets from Cc matrix

        pdatCc                  = [[pdatCc],[freshstream]];              %
append Cc matrix with fresh packets
```

```
        [chosen3]                = stoch_func3(pkts_pu,packetsF0);       %
function: purge old packets from Cc

        kg_ash_N_ratio(s,:)      = pdatCc(5,chosen3)./pdatCc(2,chosen3);
        avekg_ash_N_ratio(s)     = mean(kg_ash_N_ratio(s,:));

        pdatCc(:,chosen3)        = [];                                    %
Remove purge packets from Cc matrix

CaCO3inrecycle(s)=sum(FRdata(4,:))*CaO_pp;
CaOinrecycle(s)=(CaO_pp*length(FRdata))-CaCO3inrecycle(s);

CcHin1(s)       = (Hr_Cc*(CaCO3inrecycle(s)+F0_)); % energy required to
calcine
CcHin2(s)       =
(300*((CaCO3inrecycle(s)*Cp_CaCO3_1223_923)+(CaOinrecycle(s)*Cp_CaO_1223_92
3)));
CcHin3(s)       = (F0_*Cp_CaCO3_1223_298*950); % energy required to raise
temp of fresh
CcHintot(s)     = CcHin1(s)+CcHin2(s)+CcHin3(s);

% CcHrat(r,p)      = (CcHin(r,p)/(CcHin(r,p)+Hcomb))*100;

end
Ecarbss(r,p)=mean(Ecarb((no_seconds-100):no_seconds,r,p));
end
end

%% Calculate Fuel For Experiments

LongcliffeBatch=100; % g
molesCaO=LongcliffeBatch/MCaCO3;



%% PLOTS

F0_FCO2= F0./FCO2;


% figure(1)
% Ecarbss=transpose(Ecarbss)
% plot(F0_FCO2,Ecarbss)
% legend('FR=1','FR=2','FR=3','FR=4','FR=5')
% xlabel('F0/FCO2')
% ylabel('Steady State Carbonator Efficiency (Ecarb)')
% axis([0 0.5 0 1])
%
% figure(2)
% CcHrat=transpose(CcHrat)
% plot(F0_FCO2,CcHrat)
% legend('FR=1','FR=2','FR=3','FR=4','FR=5')
% xlabel('F0/FCO2')
% ylabel('% Hin/Hin+Hcomb')
% axis([0 0.5 0 100])

save 20130502_results_50_1_001_SM_exp
```

```
% figure(3)
% bar(gramsfuelpercycle_experiments)

%% Stochastic Functions

function [chosen1] = stoch_func1(pkts_pu,packetsFR) % Pass packets Cb->Cc

    chosen1=[];
    counter=0;
if packetsFR>0
while length(chosen1) ~= packetsFR
    chosen1=unique([chosen1;ceil(rand(counter,1)*((pkts_pu-1)))]);
    counter=packetsFR-length(chosen1);
end
end
end

function [chosen2] = stoch_func2(pkts_pu,packetsFR) % Pass packets Cc->Cb

    chosen2=[];
    counter=0;
if packetsFR>0
while length(chosen2) ~= packetsFR
    chosen2=unique([chosen2;ceil(rand(counter,1)*((pkts_pu-1)))]);
    counter=packetsFR-length(chosen2);
end
end
end

function [chosen3] = stoch_func3(pkts_pu,packetsF0) % Purge packets from Cc

    chosen3=[];
    counter=0;
if packetsF0>0
while length(chosen3) ~= packetsF0
    chosen3=unique([chosen3;ceil(rand(counter,1)*((pkts_pu-1)))]);
    counter=packetsF0-length(chosen3);
end
end
end

end
```

Appendix 3-1. Matlab code for fitting absorbance to concentration

```
clear all;clc;
filename = input('Filename? ', 's');
data = importdata(filename, ',');
abs = data.data(:,1);
conc = data.data(:,3);
clear data
a0=[2 2 0.1];
options=optimset('lsqnonlin');
a=lsqnonlin(@calibration,a0,[],[],options,abs,conc);
x=0:0.05:25;
y=a(1).*(exp(-x)-1)+a(2).*x+a(3).*x.^2;
% y=y*100;
plot(x,y);
hold on
plot(abs,conc,'x')
axis tight
xlabel('absorbance')
ylabel('calculated concentration(%)')
% axis([0 5 0 100]);
format long
sprintf('The calibration curve equation is y=%d*(exp(-x)-1)+%d*x+%d*x^2',a)
```

Appendix 6-1. Experimental Procedures

General Requirements

1. Laboratory temperature maintained at 20 ± 2 ^{o}C.
2. Relative humidity of not less than 50 %.
3. Water temperature maintained at 20 ± 1 ^{o}C.
4. Moist air room or large cabinet for storage maintained at 20 ± 1 ^{o}C with relative humidity of not less than 90 %.
5. Storage container shall be made of material that does not react with cement and maintained at 20 ± 1 ^{o}C.

Standard Consistence

➢ Mixing Cement Paste

1. Lightly oil the cylindrical or truncated form mould and the base-plate by using mineral oil.
2. By using the plunger attachment for the Vicat apparatus, lower the plunger to rest on the base-plate. Manually adjust the pointer or scale to read zero.
3. Raise the plunger to the stand-by position.
4. Weigh (500 ±1) g of cement with a mass balance.
5. Measure out a quantity of water (starting with 125 ml) by means of graduated cylinder or burette.
6. Place the water and cement into the mixing bowl taking care to avoid loss of water.
7. Within 10 seconds of cement in contact with water, mix the mixture at low speed.
8. Record the time to the nearest minute as ‘zero time’.
9. After 90 seconds of mixing, stop the mixer for 30 seconds, place the paste adhering to the wall and bottom part of the bowl to the middle of the bowl by using a plastic scrapper or a spoon.
10. Restart the mixer at low speed for a further 90 seconds.
11. Vary the amount of water in step 2 until standard consistence cement has been achieved.

➢ Testing Standard Consistence

1. Transfer the paste immediately into the mould placed on the base-plate.
2. Fill the mould to excess without unnecessary compaction or vibration. Gently tap the mould against the hand to remove any voids.
3. Remove the excess with a straight-edged implement, e.g. a ruler, to leave a smooth upper surface.
4. Position the centre of the mould and base under the plunger of the Vicat apparatus.
5. Lower the plunger until it is in contact with the paste. Pause in that position in order to avoid initial velocity or forced acceleration of the moving parts.
6. Release the moving parts quickly and allow the plunger to penetrate vertically into the centre of the paste. The release of the plunger shall occur 4 minutes ± 10 seconds after zero time.
7. Record the scale reading, the distance between the bottom face of the plunger and the base-plate, 30 seconds after the release of the plunger.
8. Check whether the scale reading is (6 ± 2) mm.
9. Clean the plunger immediately after each penetration.
10. Repeat the test with pastes containing different water contents until one is found to produce a distance between plunger and base-plate of (6 ± 2) mm.
11. Record the water content as a percentage by mass of the cement to the nearest 0.5% as the water for standard consistence.

Setting Times

➢ Initial Setting Time

1. Remove the plunger from the Vicat apparatus and replace it with the needle in Figure 7.
2. Lightly oil the base of the container and Vicat mould with mineral-based oil and place the Vicat mould into the container.
3. The needle should be calibrated by lowering it to rest on the base of the container. Manually adjust the scale or pointer to read zero.
4. Raised the needle to the stand-by position.
5. Mix the cement paste with water and cement ratio in accordance to standard consistence as mentioned above.
6. Fill the mould similarly as according to standard consistence test procedures.
7. Add distilled or drinking water to the container so that the surface of the paste is submerged to a depth of at least 5 mm.
8. After 1 hour from zero time, position the centre of the mould and container under the needle of the Vicat apparatus.
9. Lower the needle until it is in contact with the paste. Pause in that position in order to avoid initial velocity or forced acceleration of the moving parts.
10. Release the moving parts quickly and allow the needle to penetrate vertically into the paste.
11. Record the scale reading, the distance between the end of the needle and the base of the container, 30 seconds after the release of the needle.
12. Clean the Vicat needle and repeat the penetration for every 10 minutes with at least 10 mm separations from the last penetrating position.
13. Report the time to the nearest 5 minutes at which the distance between the needle and the base of the container is (6 ± 3) mm as the initial setting time of the cement.

➢ Final Setting Time

1. Fit the needle with the ring attachment as shown in Figure 7.
2. Invert the filled mould from the initial setting time test and place it on the base of the container.
3. Immerse the paste into the water again.
4. Raise the needle with attachment to the stand-by position.
5. After 30 minutes of initial setting time, place the mould and container under the needle of the Vicat apparatus.
6. Lower the needle until it is in contact with the paste. Pause in that position in order to avoid initial velocity or forced acceleration of the moving parts.
7. Release the moving parts quickly and allow the needle to penetrate vertically into the paste.
8. Record the time, from zero time, at which the needle first penetrates only 0.5 mm of the paste i.e. the time at which the ring attachment first fails to leave a circular mark on the specimen. This would be the final setting time.
9. Repeat the penetration at two other positions to confirm.

Compressive Strength

➢ Mixing Cement Mortar Paste

1. Weigh (450 ± 2) g of cement and (1350 ± 5) g of sand with a mass balance.
2. Measure out (225 ± 1) ml of water by means of a graduated cylinder or burette.
3. Place the water and cement into the mixing bowl taking care to avoid loss of water.
4. Within 10 seconds of cement contact with water, start mixing at low speed.
5. Record the time to the nearest minute as ‘zero time’.

6. After 30 seconds of mixing, add the sand steadily over the next 30 seconds.
7. Switch the mixer to high speed and continue mixing for an additional 30 seconds.
8. Stop the mixer for 90 seconds. During the first 30 seconds, remove by means of a plastic scrapper or spoon the paste adhering to the wall and bottom part of the bowl and place in the middle of the bowl.
9. Continue the mixing at high speed for 60 seconds.

Moulding Test Specimens

1. Mould the specimen immediately after the preparation of the mortar using a suitable scoop.
2. Introduce in one or more increments, the first of two layers of mortar into each of the mould compartments, directly from the mixing bowl.
3. Spread the layer uniformly and then compact using 60 jolts of the jolting apparatus.
4. Introduce the second layer of mortar, and compact the layer with a further 60 jolts.
5. Strike off the excess mortar with a metal straightedge, drawn forwards and backwards along each mould compartment.
6. Place a steel plate or plastic sheet on the mould and place the covered mould in a horizontal position in a moist chamber.

Demoulding and Curing Test Specimens

1. Demould specimens, for 24 hour tests, not more than 20 mins before the specimens are tested. For tests at ages greater than 24 hours, carry out demoulding between 20 and 24 hours after moulding.
2. Suitably mark specimens selected for curing in water.
3. Place specimens in water at (20 ± 1) ^{o}C in curing container.
4. Ensure that specimens are kept apart and that water has free access to all six faces of the specimens.
5. Ensure that at no time during storage the depth of water above the upper faces of the specimens be less than 5mm.

Testing Compressive Strength

1. Carry out strength tests at the different ages ie. 3 and 7 days.
2. Remove specimens required for testing from the water not more than 15 minutes before the test is carried out.
3. Remove any deposit on the test faces and cover specimens with a damp cloth until tested.
4. Centre the specimen laterally to the platens of the machine.
5. Increase the stress smoothly at the rate of 0.6 MPa/s until fracture occurs.

Appendix 6-2. Stress-strain curves for OPC cement and cement from cycled sorbent

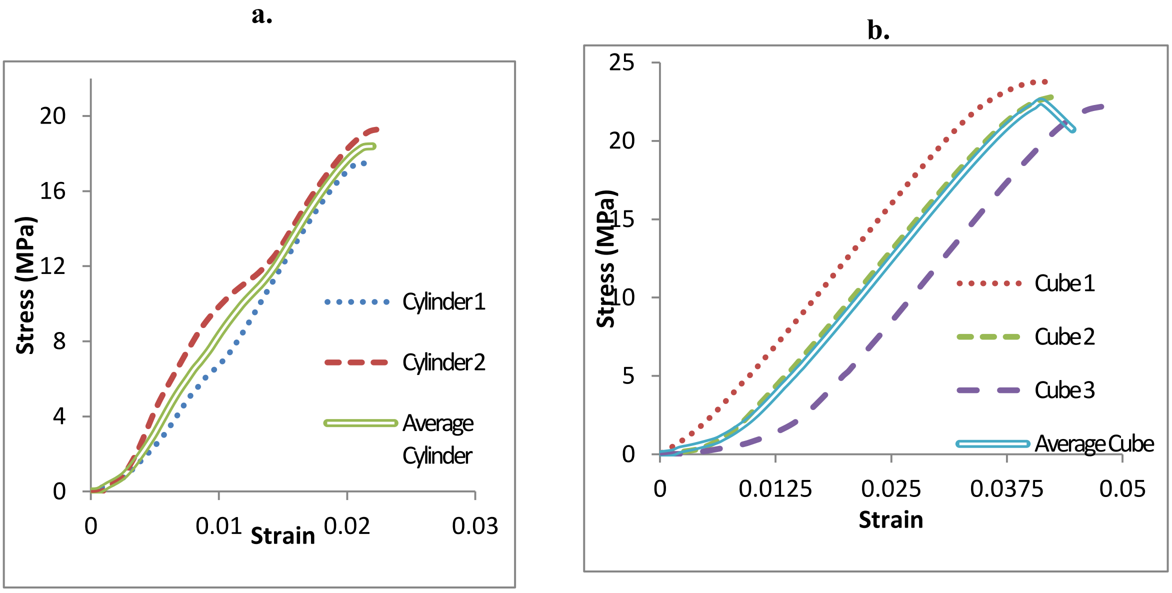

Figure 6-10. Stress-strain behaviour for OPC 3-day a) cylinders; and b) cubes.

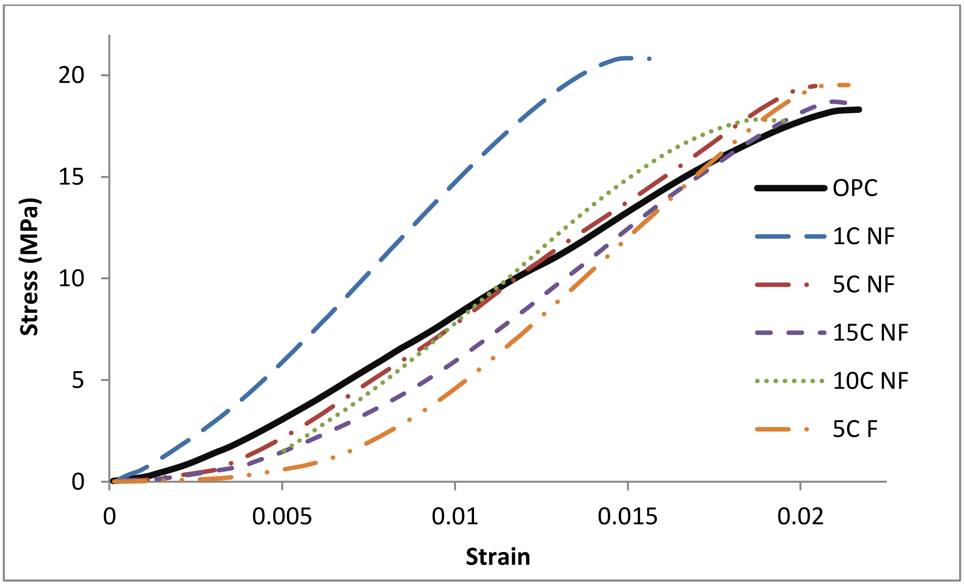

Figure 6-11. Stress-strain behaviour for test specimens.

References

Abanades, J. C. (2002). "The maximum capture efficiency of CO_2 using a carbonation/calcination cycle of CaO/CaCO3." Chemical Engineering Journal**90**(3): 303-306.

Abanades, J. C. and D. Alvarez (2003). "Conversion limits in the reaction of CO_2 with lime." Energy & Fuels**17**(2): 308-315.

Abanades, J. C., G. Grasa, et al. (2007). Cost Structure of a Postcombustion CO_2 Capture System Using CaO. **41:** 5523-5527.

Agnihotri, R., S. K. Mahuli, et al. (1999). "Influence of Surface Modifiers on the Structure of Precipitated Calcium Carbonate." Industrial & Engineering Chemistry Research**38**(6): 2283-2291.

Ahn, H., D. C. Ozcan, et al. (2011). Process Integration of Ca-Looping Process with Cement Manufacturing Plant. 3rd IEAGHG HTSLC. Vienna, Austria.

Aihara, M., T. Nagai, et al. (2001). "Development of porous solid reactant for thermal-energy storage and temperature upgrade using carbonation/decarbonation reaction." Applied Energy**69**(3): 225-238.

Al-jeboori, M. J., M. Nguyen et al. (2013). " Improvement of Limestone-Based CO_2 Sorbents for Ca Looping by HBr and Other Mineral Acids" Ind. Eng. Chem. Res. 52(4) 1426-1433.

Alonso, M. (2013). B. Gonzalez. (Private Communication)

Alonso, M., N. Rodríguez, et al. (2010). "Carbon dioxide capture from combustion flue gases with a calcium oxide chemical loop. Experimental results and process development." International Journal of Greenhouse Gas Control**4**(2): 167-173.

Alonso, M., N. Rodriguez, et al. (2009). "Modelling of a fluidized bed carbonator reactor to capture CO2 from a combustion flue gas." Chemical Engineering Science**64**(5): 883-891.

Alsop, P. A., C. Hung, et al. (2007). Cement plant operations handbook Dorking, Surrey, UK., Tradeship Publications, ©2007.

Alvarez, D. and J. C. Abanades (2005). "Determination of the critical product layer thickness in the reaction of CaO with CO_2." Industrial & Engineering Chemistry Research**44**(15): 5608-5615.

Alvarez, D., M. Peña, et al. (2007). "Behavior of Different Calcium-Based Sorbents in a Calcination/Carbonation Cycle for CO_2 Capture." Energy & Fuels**21**(3): 1534-1542.

Anthony, E. J. (2008). "Solid Looping Cycles: A New Technology for Coal Conversion." Industrial & Engineering Chemistry Research**47**(6): 1747-1754.

Anthony, E. J. and D. L. Granatstein (2001). "Sulfation phenomena in fluidized bed combustion systems." Progress in Energy and Combustion Science**27**(2): 215-236.

ASTM (2006). ASTM C187 11e1: Standard Test Method for Amount of Water Required for Normal Consistency of Hydraulic Cement Paste. West Conshohocken, PA., American Society for the Testing of Materials.

ASTM (2008). C191-08: Standard Test Methods for Time of Setting of Hydraulic Cement by Vicat Needle. West Conshohocken, PA., American Society for the Testing of Materials.

ASTM (2009). ASTM C150 / C150M - 12 Standard Specification for Portland Cement.

ASTM (2009). ASTM Standard C109/C109M - 11b: Standard Test Methods for Time of Setting of Hydraulic Cement by Vicat Needle. West Conshohocken, PA., American Society for the Testing of Materials.

ASTM (2009b). ASTM 266-08e1: Standard Test Method for Time of Setting of Hydraulic-Cement Paste by Gillmore Needles. West Conshohocken, PA.

Babcock and Wilcox (1978). Steam: Its generation and use. New York, Babcock and Wilcox.

Barker, D. J., S. A. Turner, et al. (2009). "CO_2 capture in the cement industry. ." GHTGT-9. Energy Procedia 1: 87 - 94.

Barker, R. (1973). "Reversibility of Reaction $CaCO_3 = CaO + CO_2$." Journal of Applied Chemistry and Biotechnology**23**(10): 733-742.

Barnes, R. M. (1981). Developments in Atomic Plasma Spectrochemical Analysis. London, U.K., Heyden.

Bhatia, S. K. and D. D. Perlmutter (1983). "Effect of the Product Layer on the Kinetics of the CO_2-Lime Reaction." Aiche Journal**29**(1): 79-86.

Bhatty, J. I. (1995). Role of Minor Elements in Cement Manufacture and Use. Skokie, Illinois, U.S.A, Portland Cement Association.

Bhatty, J. I. (2003). "Effect of Minor Elements on Clinker and Cement Manufacture: A Laboratory Analysis." Portland Cement Association Internal Report, Illinois, USA**Serial no. 2147**.

Blamey, J., E. J. Anthony, et al. (2010). "The calcium looping cycle for large-scale CO_2 capture." Progress in Energy and Combustion Science**36**(2): 260-279.

Borgwardt, R. H. (1989a). "Sintering of Nascent Calcium-Oxide." Chemical Engineering Science**44**(1): 53-60.

Borgwardt, R. H. (1989b). "Calcium oxide sintering in atmospheres containing water and carbon dioxide." Industrial & Engineering Chemistry Research**28**(4): 493-500.

Boss, C. B. and K. J. Fredeen (1997). Concepts, Instrumentation and Techniques in Inductively Coupled Plasma Optical Emission Spectrometry, Perkin Elmer.

BSI (2005). BS-EN 196-1: Methods of testing cement - Part 1: Determination of Strength. 1. London, British Standards Institute.

BSI (2008). BS-EN 196-3:2005+A1:2008: Methods of testing cement - Part 3: Determination of setting time and soundness. London, British Standards Institute.

BSI (2011). Cement. Composition, specifications and conformity criteria for common cements.

Bye, G. C. (1983). Portland cement Composition, production and preparation. Oxford, Pergamon Press Ltd:.

CEMBUREAU (1997). Alternative fuels in cement manufacture. . Brussels, The European Cement Association.

CEMBUREAU (1999). "CEMBUREAU Best Available Techniques for the Cement Industry.".

Charpentau, C. (2009). Trace Element Control in Gasification: Adsorption and Thermodynamic Equilibrium Studies. Department of Chemical Engineering and Chemical Technology. London, Imperial College London. **PhD**.

Chen, Z., J. R. Grace, et al. (2008). "Limestone particle attrition and size distribution in a small circulating fluidized bed." Fuel **87**(7): 1360-1371.

Chen, Z., H. S. Song, et al. (2009). "Long-Term Calcination/Carbonation Cycling and Thermal Pretreatment for CO_2 Capture by Limestone and Dolomite." Energy & Fuels **23**(3): 1437-1444.

Chindaprasirt, P. and S. Rukzon (2008). ""Strength, porosity and corrosion resistance of ternary blend Portland cement, rice husk ash and fly ash mortar."." Construction and Building Materials **22**(8): 1601-1606.

Choi, G. S. and F. P. Glasser (1988). " The sulphur cycle in cement kilns: vapor pressures and solid-phase stability of the sulfate phases. ." Cem. Concr. Res.**18(**367).

CMT_Equipment. (2012). "Vicat Apparatus." Retrieved 16/12, 2012, from http://www.cmtequipment.com.au/assets/images/CE100.jpg.

Corella, J., J. M. Toledo, et al. (2006). "Steam gasification of coal at low-medium (600–800 degrees C) temperature with simultaneous CO2 capture in fluidized bed at atmospheric pressure: the effect of inorganic species. 1. Literature review and comments." Industrial & Engineering Chemistry Research**45**(18): 6137 - 6146.

Cuenca M.A. and A. E.J. (1995). Pressurized fluidized beds. , Blackie Academic & Professional.

Curran, G. P. G. (1967). "Carbon dioxide-acceptor [coal] gasification process. Studies of acceptor properties." Advances in chemistry series**69**: 141.

David, J. and H. Herzog (2000). The cost of carbon capture. MIT Carbon Sequestration Forum, Cambridge, MA.

Dean, C., Hills, T., Florin, N. and Fennell, P. (2012) "Integrating Calcium Looping CO_2 Capture with the Manufacture of Cement." GHGT-11. 18th - 22nd November 2012, Kyoto, Japan.

Dean, C. C., J. Blamey, et al. (2011). "The calcium looping cycle for CO_2 capture from power generation, cement manufacture and hydrogen production." Chemical Engineering Research and DesignIn Press, Corrected Proof.

Dean, C. C, Dugwell, D. and Fennell, P. (2011). "Investigation into potential synergy between power generation, cement manufacture and CO_2 abatement using the calcium looping cycle." Energy and Environmental Science 4(6): 2050-2053

Deutsch, Y. and L. Heller-Kallai (1991). "Decarbonation and recarbonation of calcites heated in CO_2 : Part 1. Effect of the thermal regime." Thermochimica Acta**182**(1): 77-89.

Dobner, S., L. Sterns, et al. (1977). "Cyclic Calcination and Recarbonation of Calcined Dolomite." Industrial & Engineering Chemistry Process Design and Development **16**(4): 479-486.

Drax (2008). Environmental Performance Review., Drax Power Ltd.

Dunstetter, F., M. N. de Noirfontaine, et al. (2006). "Polymorphism of tricalcium silicate, the major compound of Portland cement clinker. 1. Structural data: review and unified analysis." Cem. Concr. Res.**36**: 39.

ECRA (2007). Carbon capture technology—options and potentials for the cement industry.

European_Commission. Reference document on best available techniques in cement, lime and magnesium oxide manufacturing industriesftp://ftp.jrc.es/pub/eippcb/doc/clm_bref_0510.pdf (accessed August 20, 2010)

EU (2001). Integrated Pollution Prevention and Control: Reference Document on Best Available Techniques in the Cement and Lime Manufacturing Industries., Commission of the European Union.

Ewing, J. A. Y., D. Beruto, et al. (1979). "The Nature of CaO Produced by Calcite Powder Decomposition in Vacuum and in CO_2." Journal of the American Ceramic Society **62**(11-12): 580-584.

Fennell, P. S., J. F. Davidson, et al. (2005). "A study of the mixing of solids in gas-fluidized beds, using ultra-fast MRI." Chemical Engineering Science **60**(7): 2085-2088.

Fennell, P. S., J. F. Davidson, et al. (2007b). "Regeneration of sintered limestone sorbents for the sequestration of CO_2 from combustion and other systems." Journal of the Energy Institute **80**(2): 116-119.

Fennell, P. S., R. Pacciani, et al. (2007a). The Effects of Repeated Cycles of Calcination and Carbonation on a Variety of Different Limestones, as Measured in a Hot Fluidized Bed of Sand. Energy and Fuels. **21:** 2072-2081.

Florin, N. H. and A. T. Harris (2008a). "Enhanced hydrogen production from biomass with in situ carbon dioxide capture using calcium oxide sorbents." Chemical Engineering Science **63**(2): 287-316.

Florin, N. H. and A. T. Harris (2008b). "Screening CaO-Based Sorbents for CO_2 Capture in Biomass Gasifiers." Energy & Fuels**22**(4): 2734-2742.

Florin, N. H. and A. T. Harris (2008c). "Preparation and characterization of a tailored carbon dioxide sorbent for enhanced hydrogen synthesis in biomass gasifiers." Industrial & Engineering Chemistry Research**47**(7): 2191-2202.

FLSmidth. (2011). "Preheater Calciner Systems." Retrieved 04 / 11, 2013, from http://www.flsmidth.com/~/media/Brochures/Brochures%20for%20kilns%20and%20firing/preheater_lores.ashx.

Foster_Wheeler. (2012). "Circulating-Fluidized Bed (CFB) Steam Generators." Retrieved 09 / 05, 2013, from http://www.fwc.com/GlobalPowerGroup/SteamGenerators/CirculatingFluidizedBed.cfm

Gaines, P. R. (2012). Message Via Website. C. Dean. London.

Glasser, F. P., J. I. Bhatty, et al. (2004). Advances in cement clinkering. In: Portland Cement Association. Innovations in Portland cement manufacture. . Skokie/Illinois.

Gonzalez, B., G. S. Grasa, et al. (2008). Modeling of the Deactivation of CaO in a Carbonate Loop at High Temperatures of Calcination. **47:** 9256-9262.

Grace J.R., Avidan A., et al. (1997). Circulating fluidized beds., Blackie Academic & Professional.

Grasa, G., J. C. Abanades, et al. (2009). "Effect of Partial Carbonation on the Cyclic CaO Carbonation Reaction." Industrial & Engineering Chemistry Research**48**(20): 9090-9096.

Grasa, G. S. and J. C. Abanades (2006). CO_2 Capture Capacity of CaO in Long Series of Carbonation/Calcination Cycles. **45:** 8846-8851.

Greco, R. and G. Enfil (2006). "Combustion of unusual fuels." World Cement**37**: 33.

Gupta, H., M. V. Iyer, et al. (2004). "Reactive separation of CO<SUB align=right><SMALL>2</small></sub> using pressure pelletised limestone." International Journal of Environmental Technology and Management **4**(1): 3-20.

Harrison, D. P. (2008). "Sorption-Enhanced Hydrogen Production: A Review." Industrial & Engineering Chemistry Research **47**(17): 6486-6501.

Hayhurst, A. N. and R. F. Tucker (1991). "The reductive regeneration of sulphated limestone for flue-gas desulphurization—thermodynamic considerations of converting calcium-sulphate to calcium-oxide." Journal of the Institute of Energy **64**(461): 212-229.

Herzog, H. (1998). The economics of CO_2 capture. the 4th International Conference on Greenhouse Gas Control Technologies, Interlaken, Switzerland.

Hou, X. (2000). "Inductively Coupled Plasma/Optical Emission Spectrometry."

Hughes, R. W., D. Lu, et al. (2004). Improved Long-Term Conversion of Limestone-Derived Sorbents for In Situ Capture of CO_2 in a Fluidized Bed Combustor. **43:** 5529-5539.

Hughes, R. W., A. Macchi, et al. (2009). "Changes in Limestone Sorbent Morphology during CaO-$CaCO_3$ Looping at Pilot Scale." Chemical Engineering & Technology**32**(3): 425-434.

IEA (2006). Energy Technology Perspectives 2006: Scenarios & Strategies to 2050. Paris, IEA (International Energy Agency).

IEA. (2010). "IEA High Temperature Looping Cycles Website." from http://www.co2captureandstorage.info/networks/looping.htm.

Imlach, J. A. (1976). "Non-isothermal investigations of the kinetics of reaction occurring during clinker formation." Cem. Concr. Res.**6**: 747.

Inorganic_Ventures. (2013). "Inorganic Ventures Interactive Periodic Table." from http://inorganicventures.com/tech/periodic-table/.

Ives, M., R. C. Mundy, et al. (2008). "Comparison of Different Natural Sorbents for Removing CO2 from Combustion Gases, as Studied in a Bench-Scale Fluidized Bed." Energy & Fuels**22**(6): 3852-3857.

Jackson, J. P. (2007). Portland Cement: Classification and Manufacture. Hewlett, PC. Lea's chemistry of cement and concrete. Oxford, Burlington, Butterworth-Heinemann**:** 25.

Jarvis, K. (2013). C. Dean.

Johansen, V. and T. V. Kouznetsova (1992). Clinker formation and new processes. 9th International Congress on the Chemistry of Cement.

Joutsenoja, T., P. Heino, et al. (1999). "Pyrometric temperature and size measurements of burning coal particles in a fluidized bed combustion reactor." Combustion and Flame**118**(4): 707-717.

Kääntee, U., R. Yevenhoven, et al. (2004). "Cement manufactoring using alternative fuels and the advantages of process modeling." Fuel. Process Technol.**85**: 293.

Kiln_Performance_Tests_Task_Force (1992). Execution and Evaluation of Kiln Performance Tests. Dusseldorf, Germany, German Association of Cement Works (VDZ).

Klauss, J. (2000). "Burning cement clinker under reducing conditions in a rotary kiln – one way of lowering the NOx emission?" ZKG-international.**53**: 132.

Klug, H. P. and L. E. Alexander (1954). X-Ray Diffraction Procedures For Polycrystalline and Amorphous Materials, Wiley.

Klug, H. P. and L. E. Alexander (1974). "X-ray Diffraction." Addision-Wilson Publishing Company Inc, USA: 132.

Kuramoto, K., S. Shibano, et al. (2003). "Deactivation of Ca-Based Sorbents by Coal-Derived Minerals during Multicycle CO_2 Sorption under Elevated Pressure and Temperature." Industrial & Engineering Chemistry Research**42**(15): 3566-3570.

Lanauze, R. D. (1985). Fundamentals of Coal Combustion: In Fluidization (Davidson, J. F.).

Laursen, K., W. Duo, et al. (2000). "Sulfation and reactivation characteristics of nine limestones." Fuel**79**(2): 153-163.

Li, F. and L.-S. Fan (2008). "Clean coal conversion processes - progress and challenges." Energy & Environmental Science **1**(2): 248-267.

Li, Y. J., C. S. Zhao, et al. (2009). "CO_2 Capture Behavior of Shell during Calcination/Carbonation Cycles." Chemical Engineering & Technology **32**(8): 1176-1182.

Li, Z.-s., N.-s. Cai, et al. (2005). "Synthesis, Experimental Studies, and Analysis of a New Calcium-Based Carbon Dioxide Absorbent." Energy & Fuels **19**(4): 1447-1452.

Lisbona, P., A. Martinez, et al. (2010). "Integration of Carbonate CO(2) Capture Cycle and Coal-Fired Power Plants. A Comparative Study for Different Sorbents." Energy & Fuels **24**: 728-736.

Liu, W., B. Feng, et al. (2010). "Synthesis of Sintering-Resistant Sorbents for CO_2 Capture." Environmental Science & Technology **44**(8): 3093-3097.

Liu, W., N. W. L. Low, et al. (2009). "Calcium Precursors for the Production of CaO Sorbents for Multicycle CO_2 Capture." Environmental Science & Technology **44**(2): 841-847.

Lu, D., R. Hughes, et al. (2009). "Sintering and Reactivity of -Based Sorbents for In Situ Capture in Fluidized Beds under Realistic Calcination Conditions." Journal of Environmental Engineering**135**(6): 404-410.

Lu, D. Y., R. W. Hughes, et al. (2008). "Ca-based sorbent looping combustion for CO_2 capture in pilot-scale dual fluidized beds." Fuel Processing Technology**89**(12): 1386-1395.

Lu, H., A. Khan, et al. (2008). "Relationship between Structural Properties and CO_2 Capture Performance of CaO−Based Sorbents Obtained from Different Organometallic Precursors." Industrial & Engineering Chemistry Research**47**(16): 6216-6220.

Lu, H., E. P. Reddy, et al. (2006). "Calcium Oxide Based Sorbents for Capture of Carbon Dioxide at High Temperatures." Industrial & Engineering Chemistry Research**45**(11): 3944-3949.

Lyngfelt, A. and B. Leckner (1989). "Sulphur capture in fluidized bed boilers: The effect of reductive decomposition of CaSO4." The Chemical Engineering Journal**40**(2): 59-69.

Lysikov, A. I., A. N. Salanov, et al. (2007). "Change of CO_2 carrying capacity of CaO in isothermal recarbonation-decomposition cycles." Industrial & Engineering Chemistry Research**46**(13): 4633-4638.

MacKenzie, A., D. L. Granatstein, et al. (2007). "Economics of CO_2 capture using the calcium cycle with a pressurized fluidized bed combustor." Energy & Fuels **21**(2): 920-926.

Mackes, K. H. and C. R. Lightburn (2003). "Evaluating the use of green wood chips processed from small-diameter trees as an alternative fuel for making cement." Forest Product Journal **53**: 42.

Macphee, D. E. and E. E. Lachowski (2007). Cement components and their phase relations. Hewlett PC. Lea’s chemistry of cement and concrete. Oxford, Burlington, Butterworth-Heinemann**:** 95.

Maki, I. and K. Goto (1982). "Factors influencing the phase constitution of alite in Portland cement clinker." Cem. Concr. Res.**12**: 301.

Manovic, V. and E. J. Anthony (2007). "Steam reactivation of spent CaO-based sorbent for multiple CO_2 capture cycles." Environmental Science & Technology **41**(4): 1420-1425.

Manovic, V. and E. J. Anthony (2008a). "Thermal activation of CaO-based sorbent and self-reactivation during CO_2 capture looping cycles." Environmental Science & Technology **42**(11): 4170-4174.

Manovic, V. and E. J. Anthony (2008c). Parametric Study on the CO_2 Capture Capacity of CaO-Based Sorbents in Looping Cycles. **22:** 1851-1857.

Manovic, V. and E. J. Anthony (2009a). "Long-Term Behavior of CaO-Based Pellets Supported by Calcium Aluminate Cements in a Long Series of CO_2 Capture Cycles." Industrial & Engineering Chemistry Research **48**(19): 8906-8912. 2

Manovic, V. and E. J. Anthony (2009b). "Screening of Binders for Pelletization of CaO-Based Sorbents for CO_2 Capture." Energy & Fuels **23**(10): 4797-4804.

Manovic, V., E. J. Anthony, et al. (2008b). "CO_2 looping cycle performance of a high-purity limestone after thermal activation/doping." Energy & Fuels **22**(5): 3258-3264.

Manovic, V., D. Lu, et al. (2008). "Steam hydration of sorbents from a dual fluidized bed CO2 looping cycle reactor." Fuel **87**(15-16): 3344-3352.

Mcbride, B. J., M. J. Zehe, et al. (2002). NASA Glenn Coefficients for Calculating Thermodynamic Properties of Individual Species. N. A. a. S. Administration. Cleveland, OH, USA.

Mess, D., A. F. Sarofim, et al. (1999). "Product layer diffusion during the reaction of calcium oxide with carbon dioxide." Energy & Fuels **13**(5): 999-1005.

Metz, B., O. Davidson, et al. (2007). Mitigation, in Intergovernmental Panel on Climate Change, Fourth Assessment Report, Climate Change 2007.

Metz, B., O. Davidson, et al. (2005). Special Report on Carbon Dioxide Capture and Storage, Intergovernmental Panel on Climate Change. Cambridge, UK, Cambridge University Press.

Mindat.org. (2013). "Brownmillerite." Retrieved 04/04, 2013, from http://www.mindat.org/min-790.html.

Mineral_News. "General Brownmillerite Information " Retrieved 04/04, 2013, from http://webmineral.com/data/Brownmillerite.shtml.

Mohan, K. and F. P. Glasser (1977). "The thermal decomposition of $C3SiO_5$ at temperatures below 1250 °C." Cem. Conr. Res.**Part 1-3.** : 1.

Mokrzycki, E. and A. Uliasz-Bochenczyk (2003). "Alternative fuels for the cement industry." Appl. Energy **74**: 95.

Montaser, A. and D. W. Golighty (1992). Inductively Coupled Plasmas in Analytical Atomic Spectrometry. New York, VCH Publishers.

Moser, R. Mass Concrete. Materials Science of Concrete, Georgia Institute of Technology.

Neville, A. M. (1991). Concrete Technology. Essex, England, Longman Scientific and Technical**:** p.95.

Neville, A. M. (1991). Concrete Technology. U.S., Longman Scientific and Technical.

Neville, A. M. (2010). Concrete Technology. U.S., Longman Scientific and Technical.

NIST. (2011). "Webbook." from http://webbook.nist.gov/cgi/cbook.cgi?ID=C124389&Units=SI&Type=IR-SPEC&Index=1#IR-SPEC.

Oreskes, N. (2004). "Beyond the ivory tower - The scientific consensus on climate change." Science**306**(5702): 1686-1686.

Pacciani, R., C. R. Müller, et al. (2008a). "Synthetic Ca-based solid sorbents suitable for capturing CO_2 in a fluidized bed." The Canadian Journal of Chemical Engineering **86**(3): 356-366.

Pacciani, R., C. R. Müller, et al. (2008b). "How does the concentration of CO_2 affect its uptake by a synthetic Ca-based solid sorbent?" Aiche Journal **54**(12): 3308-3311.

Perry, R. H. (1997). Perry's Chemical Engineer Handbook, Mcgraw-Hill.

Pipilikaki, P., M. Katsioti, et al. (2005). "Use of tire derived fuel in clinker burning. ." Cem. Concr. Res.**27**: 843.

Pizant, J. and J. C. Gauthier (1997). "Burning alternative fuels in rotary kiln." World Cement **September**: 64.

Proscoandro, M., G. Mazziotti, et al. (2003). "Effect of burning supplementary waste fuels on the pollutant emission by cement plants: a statistical analysis of process data." Resour. Conserv. Recycl.**39**: 161.

Rodriguez, N. (2008). "Heat requirements in a calciner of $CaCO_3$ integrated in a CO_2 capture system using CaO." Chemical Engineering Journal **138**(1-3): 148-154.

Rodríguez, N., M. Alonso, et al. (2010). "Average activity of CaO particles in a calcium looping system." Chemical Engineering Journal **156**(2): 388-394.

Rodríguez, N., M. Alonso, et al. (2011). "Comparison of experimental results from three dual fluidized bed test facilities capturing CO_2 with CaO." Energy Procedia**4**(0): 393-401.

Rodriguez, N., M. Alonso, et al. (2008). "Process for capturing CO_2 arising from the calcination of the $CaCO_3$ used in cement manufacture." Environmental Science & Technology**42**(18): 6980-6984.

Romeo, L. M., J. C. Ballesteros, et al. (2008). "Oxyfuel carbonation/calcination cycle for low cost CO_2 capture in existing power plants."

Romeo, L. M., Y. Lara, et al. (2009b). "Optimizing make-up flow in a CO_2 capture system using CaO." Chemical Engineering Journal **147**(2-3): 252-258.

Romeo, L. M., Y. Lara, et al. (2009a). "Economical assessment of competitive enhanced limestones for CO2 capture cycles in power plants." Fuel Processing Technology **90**(6): 803-811.

Ryu, H.-J., J. R. Grace, et al. (2006). "Simultaneous CO_2/SO_2 Capture Characteristics of Three Limestones in a Fluidized-Bed Reactor." Energy & Fuels **20**(4): 1621-1628.

Saastamoinen, J., T. Pikkarainen, et al. (2008). "Model of fragmentation of limestone particles during thermal shock and calcination in fluidised beds." Powder Technology **187**(3): 244-251.

Sakadjian, B. B., M. V. Iyer, et al. (2006). "Kinetics and Structural Characterization of Calcium-Based Sorbents Calcined under Subatmospheric Conditions for the High-Temperature CO_2 Capture Process." Industrial & Engineering Chemistry Research **46**(1): 35-42.

Salvador, C., D. Lu, et al. (2003). "Enhancement of CaO for CO_2 capture in an FBC environment." Chemical Engineering Journal **96**(1-3): 187-195.

Scala, F., R. Chirone, et al. (2003). "The influence of fine char particles burnout on bed agglomeration during the fluidized bed combustion of a biomass fuel." Fuel Processing Technology **84**(1–3): 229-241.

Scala, F., F. Montagnaro, et al. (2008). "Sulphation of limestones in a fluidized bed combustor: The relationship between particle attrition and microstructure." The Canadian Journal of Chemical Engineering **86**(3): 347-355.

Schueppel, B. (2009). Attrition test for calcium-based sorbent materials. 1st IEA GHG Solid Looping Cycles Network Meeting, INCAR-CSIC, Oviedo, Spain.

Shimizu, T., T. Hirama, et al. (1999). "A Twin Fluid-Bed Reactor for Removal of CO_2 from Combustion Processes." Chemical Engineering Research and Design **77**(1): 62-68.

Silaban, A. and D. P. Harrison (1995). "High temperature capture of carbon dioxide: Characteristics of the reversible reaction between CaO(s) and CO_2(g)." Chemical Engineering Communications **137**: 177-190.

Silaban, A., M. Narcida, et al. (1996). Characteristics of the reversible reaction between CO_2(g) and calcined dolomite. Elmont, NY, ETATS-UNIS, Taylor & Francis.

Smith, I. M. (2007). Properties and Behaviour of SO_2 Adsorbents for CFBC, IEA Clean Coal Centre, London.

Stanmore, B. R. and P. Gilot (2005). "Review—calcination and carbonation of limestone during thermal cycling for CO_2 sequestration." Fuel Processing Technology **86**(16): 1707-1743.

Stöppel, R. (2004). " Burning rubber." World Cement **August**: 61.

Stutzman, P. E. (1996). Guide for X-Ray Powder Diffraction Analysis of Portland Cement and Clinker, National Institute of Standards and Technology.

Sun, P., J. R. Grace, et al. (2006). "Removal of CO_2 by Calcium-Based Sorbents in the Presence of SO_2." Energy & Fuels**21**(1): 163-170.

Sun, P., J. R. Grace, et al. (2008). "Investigation of attempts to improve cyclic CO_2 capture by sorbent hydration and modification." Industrial & Engineering Chemistry Research **47**(6): 2024-2032.

Taylor, H. F. W. (1997). Cement Chemistry. London, Academic Press Thomas Telford.

Thompson, M. and J. N. A. Walsh (1983). Handbook of Inductively Coupled Plasma Spectrometry. London, Blackie.

Trezza, M. A. and A. N. Scian (2000). "Burning waste as an industrial resource. Their effect on Portland cement clinker." Cem. Concr. Res. **30**: 137.

Trezza, M. A. and A. N. Scian (2005). "Waste fuels: their effect on Portland cement clinker." Cem. Concr. Res. **35**: 438.

Wang, J. and E. J. Anthony (2005). On the Decay Behavior of the CO_2 Absorption Capacity of CaO-Based Sorbents. **44:** 627-629.

Wang, J., S. Lin, et al. (2009). "Limestone calcination with CO_2 capture (III): characteristics of coal combustion during limestone decomposition." Energy & Fuels**23**: 2804-2809.

Wang, W., S. Ramkumar, et al. (2010). "Subpilot Demonstration of the Carbonation−Calcination Reaction (CCR) Process: High-Temperature CO_2 and Sulfur Capture from Coal-Fired Power Plants." Industrial & Engineering Chemistry Research**49**(11): 5094-5101.

Wang, Y., S. Lin, et al. (2008). "Limestone calcination with CO_2 capture (II): decomposition in CO_2/steam and CO_2/N2 atmospheres." Energy & Fuels**22**(4): 2326-2331.

WBCSD (2006). "Getting the Numbers Right."

Welz, B. and H. Sperling (1997). Atomic Absorption Spectrometry. Weinheim, Wiley.

Wen, C. Y. and Y. H. Yu (1966). A generalized method for predicting the minimum fluidization velocity. **12:** 610-612.

World_Cement_News. (2011). "Cemex UK’s increased alternative fuels results in substantial CO_2 saving."   Retrieved 07/04, 2012, from http://www.worldcement.com/sectors/environmental/articles/Cemex_UK’s_increased_alternative_fuels_results_in_substantial_CO2_saving.aspx.

Zabaniotou, A. and C. Theofilou (2008). "Green energy at cement kiln in Cyprus-Use of sewage sluge as a conventional fuel substitute." Renewable Sustainable Energy Rev.**12**: 531.

Zeman, F. (2008). "Effect of steam hydration on performance of lime sorbent for CO_2 capture." International Journal of Greenhouse Gas Control **2**(2): 203-209.

Zuberbuehler, U. (2009). Need for standardisation of test methods for sorbent/material characterisation. 1st IEA GHG Solid Looping Cycles Network Meeting, INCAR-CSIC, Oviedo, Spain.